SAPIENZA
UNIVERSITÀ DI ROMA

Extracellular volume quantification in Cardiac CT: a new marker of cardiovascular risk in HIV positive individuals?

Scuola di dottorato in Sanità pubblica e Malattie Infettive

Dottorato di Ricerca in Medicina e Chirurgia – XXXIII Ciclo

Candidate

Cristian Borrazzo
ID number 1630667

Thesis Advisors

Prof. Iacopo Carbone
Prof. Claudio Maria Mastroianni

Co-Advisors

Prof.ssa Gabriella D'Ettorre

February 2021

Thesis defended on February 2021
in front of a Board of Examiners composed by:

Prof. Stefano D'Amelio (chairman)

Prof. Pietrantonio Ricci
Prof. Giovanni Capelli
Prof. Marco Iannetta

Extracellular volume quantification in Cardiac CT: a new marker of cardiovascular risk in HIV positive individuals?
Ph.D. thesis. Sapienza – University of Rome

This thesis has been typeset by LaTeX and the Sapthesis class.

Version: February 14, 2021

Author's email: cristian.borrazzo@uniroma1.it

Enjoy the little things

Abstract

Inflammation in response to infection and injury is a critical survival mechanism used by all higher vertebrates. Chronic inflammatory conditions are associated with the prolonged release of inflammatory mediators and the activation of harmful signal transduction pathways, all of which contribute disease development and phenotypes. Extracellular Volume Fraction (ECV) may be able to detect subtle abnormalities such as diffuse inflammation acute or chronic due to infection and/or fibrosis. The validity of this technique was preliminarily evaluated in a study with 20 patients suspected to have diffuse inflammation in the myocardial tissue. Using HU (Hounsfield Unit) values before and after administration of an Extracellular Contrast Agent (ECA) allows the additional calculation of the ECV, well established in CT. In fact, the ratio of the change in blood and tissue attenuation (ΔHU) represents the contrast agent partition coefficient. People living with HIV (PLWH) have an increase vulnerability to sub-clinical and clinical cardiovascular (CV) diseases.
Purpose: PLWH are prone to develop sub-clinical Cardiovascular (sCV) disease, despite the effectiveness of combined AntiRetroviral Therapy (cART). Algorithms developed to predict CV risk in the general population could be inaccurate when applied to PLWH. Myocardial Extra-Cellular Matrix (ECM) expansion, measured by computed tomography, has been associated with an increased CV vulnerability in HIV-negative population. Measurement of Myocardial ECV by computed tomography or magnetic resonance, is considered a useful surrogate for clinical evaluation of ECM expansion. In the present study, we aimed to determine the extent of cardiovascular involvement in asymptomatic HIV-infected patients with the use of a comprehensive cardiac computed tomography (CCT) approach.
In this study, ECV in low atherosclerotic CV risk PLWH was compared with ECV of age and gender matched HIV- individuals. 53 asymptomatic HIV+ individuals (45 males, median age 48 (IQR:42.5-48) years) on effective cART (CD4+ cell count: 450 cells/μL (IQR: 328-750); plasma HIV RNA: <37 copies/ml in all subjects) and 18 age and gender matched controls (14 males, median age 55 (IQR:44.5-56) years) were retrospectively enrolled. All participants underwent CCT protocol to obtain native and postcontrast Hounsfield unit values of blood and myocardium, ECM was calculated accordingly.
The ECV was significantly higher in HIV+ patients than in the control group (ECV: 31% (IQR: 28%-31%) vs 27.4% (IQR: 25%-28%), p<0.001). The duration of cART (standardized β =0.56 (0.33-0.95), p=0.014) and the years of exposure to HIV infection [standardized β =0.53 (0.4-0.92), p<0.001], were positively and strongly associated with ECV values. Differences in ECV (p<0.001) were also observed regarding the duration of exposure to cART (<5 years, 5-10 years and >10 years). Moreover, ECV was independently associated with age of participants [standardized β = 0.42 (0.33-0.89), p=0.084].
We hypothesized that quantitative assessment of tissue ECV would be clinically useful for detecting both focal and diffuse tissue abnormalities in a variety of acute and chronic infectious conditions. ECV imaging can quantitatively characterize tissue inflammation, atypical diffuse fibrosis, and subtle tissue abnormalities not clinically apparent on different method images. Therefore, ECV not only can detect tissue inflammation and/or fibrosis but also might quantify response to treatment during follow-up. HIV infection and exposure to antiretrovirals play a detrimental role on ECV expansion. An increase in ECV indicates ECM expansion, which has been associated to a higher CV risk in the general population. The non-invasive evaluation of ECM trough ECV could represent an important tool to further understand the relationship between HIV infection, cardiac pathophysiology and the increased CV risk observed in PLWH.

Preface

This PhD thesis represents original work by the author and has not been submitted in any form to another institution. When work of others has been used, it has been duly acknowledged in the declaration at the beginning of each chapter. The work described was performed at the Department of Public Health and Infectious Disease, University of Rome - Sapienza. Experiments and imaging studies was conducted at Azienda ospedaliera Policlinico Umberto I (Rome).

The epidemiology of HIV has changed significantly over the past 2 decades. Antiretroviral therapy, by controlling viral burden and restoring immune function, has transformed HIV infection into a chronic disease, improving patients' survival. According to a recently published meta-analysis, patients living with HIV may have a relative risk of 2 for cardiovascular conditions when compared to other high cardiovascular risk groups such as diabetes mellitus (Shah et al., 2018), due to traditional cardiovascular risk factors, but also to disease-specific factors such as inflammation, immune activation and effects of HIV medications. Traditional charts may be insufficient in quantifying risk in this setting (Triant et al., 2018). Although combined AntiRetroviral Therapy (cART) has improved the length and quality of life of People Living With HIV (PLWH), cardiovascular diseases are still a leading cause of death among non-AIDS comorbidities in this population and represent a challenge for clinicians. Several studies have shown an increased frequency of coronary atherosclerotic disease, myocardial infarction, arrhythmias and sudden death in PLWH. Interestingly, recent studies have shown that Severe Cardiovascular (CV) diseases are more frequent than expected in low Atherosclerotic Cardiovascular Disease (ASCVD) risk PLWH as a result of a premature aging due to a possible dangerous combination of inflammation, immune-activation, cART side effects and direct viral effect. For these reasons, algorithms developed to predict CV risk in the general population could be inaccurate when applied to PLWH.
Recently, equilibrium contrast imaging has been developed to non-invasively quantify diffuse interstitial expansion in a range of organs. In this scenario, the non-invasive evaluation of cardiac Extracellular Matrix (ECM) could provide new data in evaluation of CV diseases and risk among PLWH. ECM is a complex biological network consisting of a variety of proteins (principally glycoproteins, proteoglycans, and glycosaminoglycans) in which cardiac myocytes, fibroblasts, vascular cells, and leukocytes dwell. Its structural and non structural proteins contribute to the strength and plasticity of myocardium and play a fundamental role in cardiac development, homeostasis, and remodelling. ECM alterations may indicate a loss of cardiac morphological homeostasis and may ultimately represent an indicator of CV diseases. In particular, myocardial ECM expansion has been linked with cardiac electrical,

mechanical and vasomotor dysfunctions, cardiac fibrosis and, ultimately, with increase of mortality. Contrast enhanced cardiac Computed Tomography (CT) and Cardiovascular Magnetic Resonance (CMR) both use extracellular, Extravascular Contrast Agents (ECA), permitting to measure and quantify non-invasively the myocardial Extracellular Volume fraction (ECV). Quantifying the ECV can be relevant in different fields such as oncology, nuclear medicine, cardiology, or infectious diseases. The aims of our work were i) to investigate on the accuracy of ECV measurements obtainable by CT and/or by Magnetic Resonance Imaging (MRI), ii) to investigate on possible uses in clinics and iii) to evaluation on cardiac ECV to provide new data in evaluation of CV diseases and ASCVD risk among PLWH.
The manuscript comprises 9 chapters, with experimental chapters summarized below. Unless otherwise stated, all work is that of the author. Peer-reviewed publications related to each chapter are summarized below.
A general overview of the current understanding of the epidemiology of HIV infection is treated in the **Part I**, **chapter 1**, where the status-of-the-art of HIV infection epidemiology available is described. Particular emphasis is given to the cardiovascular disease risk prediction for PLWH. **Chapter 2** is devoted to imaging Cardiac CT principles. A concise overview on basic principles is outlined, together with the development of models set up that are used to better characterizes the physical system that is object of this thesis. **Chapter 3** describes the translation of the equilibrium imaging technique from MRI to CT imaging platform, with development of an iodinated contrast equilibrium protocol for ECV. **Part II**, **chapter 4** is devoted to the preliminary analysis of the proposed ECV. **Chapter 5** concerns the creation of test objects. These test objects were vials (falcon, or blood test vial) in which solid structures were inserted, creating a physical compartmentalization of the water content. The test objects were examined with CT and MRI conventional imaging protocols used for clinical examinations, to quantify ECV accuracy.
Chapter 6 focuses on ECV quantification in some clinical applications. In the first application, a group of patients, undergone MR examination for known or suspected heart disorder was examined, assessing the ECV performance as predictive value for cardiologic diseases. In the second application, CEMRI (contrast-enhanced MRI) data of patients with newly diagnosed brain tumors were retrospectively reviewed, calculating the ECV values. Finally, the third application examined the possibility to perform a patient-specific estimation of the Red Marrow (RM) ECV, which is needed to calculate the absorbed dose to RM for evaluating tolerability of radioimmunotherapy treatments, or other treatments with radiopharmaceutical having large carrier molecules, in a nonmyeloablative setting. Lastly, cardiac ECV in low ASCVD risk PLWH was evaluated and compared to that of healthy HIV negative individuals. **Part III** is devoted to the discussion and conclusion of the proposed new method for quantifying ECV in HIV patients. **Chapter 7**, **8** and **9** present the future perspectives and the summarized conclusions of this thesis. **Appendix A** reports some additional informations regarding physics principles, and **Appendix B** contains the accepted observing proposal that I have submitted as corresponding author to study radiology applications.

The work described in this thesis was undertaken between October 2017 and October 2020 while I was a PhD student under the supervision of Prof. Claudio

Maria Mastroianni, Prof. Gabriella d'Ettore and Prof. Iacopo Carbone in the Department of Public Health and Infectious Disease, University of Rome, Sapienza. Portions of this thesis have appeared in the following papers.

Publications presented with this Thesis

- Chapter 4: Altabella Luisa, Borrazzo Cristian et al. "A feasible and automatic free tool for T1 and ECV mapping". Physica Medica (2017).
- Chapter 4: Borrazzo Cristian, et al. "Myocardial blood flow estimates from dynamic contrast-enhanced magnetic resonance imaging: three quantitative methods". Physics in Medicine and Biology (2018).
- Chapter 5: Borrazzo Cristian et al. "T1 and extracellular volume fraction mapping in cardiac magnetic resonance: estimation of accuracy and precision of a novel algorithm". Physics in Medicine and Biology (2019).
- Chapter 6: Borrazzo Cristian et al. "Unexpected increase of myocardial extracellular volume fraction in low cardiovascular risk HIV patients". Journal of transactional medicine communications (2020).

Publications associated with this Thesis

- Silvestri Valeria, Borrazzo Cristian et al. "Carotid Artery Aneurysm in HIV: A Review of Case Reports in Literature." Annals of vascular surgery (2020).
- Santinelli, Letizia, ..., Borrazzo Cristian et al. "Real word outcomes associated with use of raltegravir in older people living with HIV: results from the 60 months follow-up of the RAL-age cohort." Expert Review of Anti-infective Therapy (2020).
- Ceccarelli Giancarlo, ..., Borrazzo Cristian et al. "Physical Activity and HIV: Effects on Fitness Status, Metabolism, Inflammation and Immune-Activation." AIDS and Behavior (2020).
- Innocenti Giuseppe, ..., Borrazzo Cristian et al. "Modulation of Phenylalanine and Tyrosine Metabolism in HIV-1 Infected Patients with Neurocognitive Impairment: Results from a Clinical Trial." Metabolites (2020).
- Ceccarelli Giancarlo, Borrazzo Cristian et al. "Diagnostic issues of asymptomatic neurosyphilis in HIV-positive patients: a retrospective study." Brain Sciences (2019).
- d'Ettorre, Gabriella, Borrazzo Cristian et al. "Increased IL-17 and/or IFN-γ producing T-cell subsets in gut mucosa of long-term-treated HIV-1-infected women." Aids (2019).
- Silvestri, Valeria,..., Borrazzo Cristian et al. "Many Different Patterns under a Common Flag: Aortic Pathology in HIV—A Review of Case Reports in Literature." Annals of vascular surgery (2019).

Proceedings and Abstracts

- C. Borrazzo et al. "Accuracy and precision of a novel algorithm for T1 and extracellular volume fraction mapping in cardiac magnetic resonance imaging". European journal of medical physics (2018).
- Marchitelli Livia, Borrazzo Cristian et al. (2020, January). Myocardial extracellular volume fraction (ECV) quantification with CT: a new marker of cardiovascular risk in HIV positive subjects?. European Congress of Radiology 2020.

Conferences and meeting related to this thesis

- Eugenio Nelson Cavallari, ..., Cristian Borrazzo et al. "Cardiovascular risk and coronary stenosis are easily underestimated in HIV infected Subjects". Science for Democracy, Democracy for Science, Istituto superiore di sanità (2019).
- Marchitelli Livia, Borrazzo Cristian et al. "Myocardial extracellular volume fraction (ECV) quantification with CT: a new marker of cardiovascular risk in HIV positive subjects?". European Congress of Radiology (2020).
- Borrazzo Cristian et al. "Extracellular Volume Fraction by quantitative dynamic equilibrium CT provides insights into acute, chronic and sub-clinical phatology inflammation". Science for Democracy, Democracy for Science, Istituto superiore di sanità (2019).
- G. De Girolamo, L. Santinelli, C. Borrazzo, et al. "Between Association between subclinical atherosclerosis and IFN-I response in HIV-1 infected patients". XXII° ICAR (2020).

Contents

Part I

Background

Chapter 1

Epidemiology of HIV infection

Human Immunodeficiency Virus (HIV) infection is a global pandemic, with cases reported from virtually every country. At the end of 2019, an estimated 38 (31.6-44.5) million individuals were living with HIV infection, according to the Joint United Nations Programme on HIV/AIDS (UNAIDS) 2019. An estimated 95% of people living with HIV/AIDS reside in low- and middle-income countries (especially Sub Saharan Africa); 50% are female, and 1.8 million are children (0-14) years. The estimated number of people living with HIV—i.e., the global prevalence—has increased more than fourfold since 1990, reflecting the combined effects of continued high rates of new HIV infections and the life-prolonging impact of antiretroviral therapy. In 2019, the global prevalence rate among persons age 15–49 years was 0.8%, with rates varying widely by country and regions. Between 2001 and 2019, the estimated number of new HIV infections globally fell by 40%. Recent reductions in global HIV incidence likely reflect progress with HIV prevention efforts and the increased provision to HIV-infected people of antiretroviral therapy, which makes them much less likely to transmit the virus to sexual partners. In 2019, global AIDS deaths totaled 1.5 million (including 190.000 children <15 years old), a 35% decrease since 2005 that coincides with a rapid expansion of access to antiretroviral therapy. However, progress on the prevention of HIV transmission remains far too slow, with the estimated total number of new infections in 2019 more than three times higher than UNAIDS's 2020 target.

1.1 Definition

The current United States Centers for Disease Control and Prevention (CDC) classification system for HIV infection and AIDS categorizes people on the basis of clinical conditions associated with HIV infection and *CD4 T-lymphocyte* measurement. A confirmed HIV case can be classified in one of five HIV infection stages (0 to 3, or unknown). If there was a negative HIV test within 6 months of the first HIV infection diagnosis, the stage is 0, and remains 0 until 6 months after diagnosis. Advanced HIV disease is classified as stage 3 if one or more specific opportunistic illness has been diagnosed. Otherwise, the stage is determined by CD4 test results and immunologic criteria (table 1.1). If none of these criteria apply (e.g., because of missing information on CD4 test results), the stage is U (unknown) (Selik et al.,

Table 1.1. CDC HIV infection stages 1-3 based on age-specific CD4 T lymphocyte count or *CD4 T-lymphocyte* percentage of total lymphocytes (Selik et al., 2014).

Stage	**< 1 years cells/μL (%)**	**1-5 years cells/μL (%)**	**6 years cells/μL (%)**
1	$\geq 1,500$ (34)	$\geq 1,000$ (30)	≥ 500 (26)
2	750-1,499 (26-33)	$500 - 999$ (22-29)	$200 - 499$ (14-25)
3	<750 (26)	< 200 (22)	< 500 (14)

2014).

1.2 Etymology agent

HIV is the etiologic agent of AIDS; it belongs to the family of Human Retroviruses (Retroviridae) and the subfamily of Lentiviruses. The four Retroviruses known to cause human disease belong to two distinct groups: the human T-lymphotropic viruses (HTLV)-1 and HTLV-2, which are transforming retroviruses; and the human immunodeficiency viruses, HIV-1 and HIV-2, which cause cytopathic effects either directly or indirectly. The most common cause of HIV disease throughout the world, and certainly in the United States, is HIV-1, which comprises several subtypes with different geographic distributions. HIV-1 viruses likely came from chimpanzees and/or gorillas, and HIV-2 from sooty mangabeys. The AIDS pandemic is primarily caused by the HIV-1 M group viruses. Although HIV-1 group O and HIV-2 viruses have been found in numerous countries, including those in the developed world, they have caused much more localized epidemics.

1.3 Infection transmission

HIV is transmitted primarily by sexual contact (both heterosexual and male to male); by blood and blood products; and by infected mothers to infants intrapartum, perinatally, or via breast milk (Patel et al., 2014).

- **Sexual transmission:** it's predominantly a Sexually Transmitted Infection (STI) worldwide. By far the most common mode of infection, particularly in developing countries, is heterosexual transmission, although in many western countries a resurgence of male-to-male sexual transmission has occurred. Although a wide variety of factors including viral load and the presence of ulcerative genital diseases influence the efficiency of heterosexual transmission of HIV, such transmission is generally inefficient. A recent systemic review found a low per-act risk of heterosexual transmission in the absence of Antiretrovirals: 0.04% for female-to-male transmission and 0.08% for male-to-female transmission during vaginal intercourse in the absence of antiretroviral therapy or condom use. The virus appears to concentrate in the seminal fluid, particularly in situations where there are increased numbers of lymphocytes and monocytes in the fluid, as in genital inflammatory states such as urethritis

and epididymitis, conditions closely associated with other STIs. The virus has also been demonstrated in cervical smears and vaginal fluid. There is an elevated risk of HIV transmission associated with Unprotected Receptive Anal Intercourse (URAI) among both men and women compared to the risk associated with receptive vaginal intercourse.

- **Transmission through injection drug use**: HIV can be transmitted to Injection Drug Users (IDUs) who are exposed to HIV while sharing injection paraphernalia such as needles, syringes, the water in which drugs are mixed, or the cotton through which drugs are filtered. The per-act risk of transmission from injection drug use with a contaminated needle has been estimated to be approximately 0.6%.

- **Transmission by transfused blood and blood products:** HIV can be transmitted to individuals who receive HIV-tainted blood transfusions, blood products, or transplanted tissue. It is estimated that >90% of individuals exposed to HIV-contaminated blood products become infected .

- Occupational transmission of HIV: health care workers and laboratory workers have a risk to be contaminated with blood from a person with documented HIV infection of 0.3%, if the injured and/or exposed person is not treated within 24 h with antiretroviral drugs.

- **Mother to child transmission of HIV:** HIV infection can be transmitted from an infected mother to her fetus during pregnancy, during delivery, or by breast-feeding. In the absence of prophylactic antiretroviral therapy to the mother during pregnancy, labor, and delivery, and to the fetus following birth, the probability of transmission of HIV from mother to infant/ fetus ranges from 15% to 25% in industrialized countries and from 25% to 35% in developing countries (Fauci and Lane, 2001).

Pathogenesis

The primary targets of the HIV are probably the dendritic cells in the mucosa of the genital tract. The virus uses a specific receptor called DC-SIGN to attach to those cells. The dendritic cells then transport HIV into lymph nodes, where the virus infects lymphocytes. The receptors for HIV are mainly the CD4 molecules on the surface of a sub-population of T lymphocytes. A co-receptor is also necessary for infection. Viruses that preferentially interact with the co-receptor CCR5 are called "R5 viruses" (or "monocytotropic," or "nonsyncytium–inducing"), and they predominate in early infection. Later on, HIV often acquires the capacity to interact with the CXCR4 receptor; such viruses are called "X4" ("syncytium-inducing," or “lymphocytotropic”). The CD4 lymphocytes whose T-cell receptor is specific for HIV proteins proliferate and are preferentially infected. This preferential infection (followed by destruction) may explain the specific deficiency of immunity.More than 98% of lymphocytes are localized in the lymph nodes and spleen. Nonetheless, the viruses produced by the newly HIV infected lymphocytes flood the blood and are transported into all tissues within a matter of days. Viremia reaches high levels—up

Table 1.2. Estimated per-act probability of acquiring HIV from an infected source, by exposure act Sources: CDC, www.cdc.gov/hiv/policies/law/risk.html;(Patel et al., 2014)). $^{(a)}$Other factors, $^{(b)}$including semen and saliva.

Type of exposure	**Risk per 1,000 Exposures**
Parenteral	
Blood transfusion	9250
Needle-sharing during injection drug use	63
Percutaneus	23
Sexual	
Receptive anal intercourse	138
Insertive anal intercourse	11
Receptive penile-vaginal intercourse	8
Insertive penile-vaginal intercourse	4
Receptive oral intercourse	Low
Insertive oral intercourse	Low
Other$^{(a)}$	
Biting	Negligible
Spitting	Negligible
Sharing sex toys	Negligible
Throwing body fluids$^{(b)}$	Negligible

to millions of HIV genomes per cubic millimeter. During this time, many patients become symptomatic with fever, skin lesions, pharyngitis, and swollen lymph nodes. This self limiting disease, lasting usually a few days to a few weeks, is called “primary HIV infection,” “acute retroviral syndrome,” or “seroconversion syndrome.”

Then, the immune response kicks in; antibodies directed against HIV appear in the blood, and cytotoxic T cells specific for HIV-infected cells proliferate. This HIV immune response rapidly achieves partial control of the HIV infection. Viremia levels decrease by several orders of magnitude, stabilizing at a lower level, called “plateau level.” This level can vary from fewer than 50 to several hundred thousand copies of HIV RNA per cubic millimeter, and it correlates closely with further evolution toward immune deficiency: the higher the level, the faster the development of AIDS. A progressive reduction in the level of CD4+ T cells is the hallmark of HIV-induced immune deficiency. A fall from the normal level of approximately 1000 CD4+ cells per cubic millimeter occurs during acute HIV infection. After seroconversion, the level of CD4+ lymphocytes again rises, but rarely returns to normal.

Later, during the chronic phase of HIV infection, a progressive annual loss of about 70 cells per cubic millimeter occurs. However, the speed at which immune deficienty progresses is extremely variable. An incubation period of 10 years is more typical, but occasionally other patients, called "long-term nonprogressors" or "elite controllers," show no evidence of damage to the immune system at all. These "nonprogressors" survive many years with low viremia and a normal number of CD4 cells. When the number of CD4 cells declines below a critical level of about $200/um^3$, the “AIDS defining diseases” start to appear. The list of opportunistic diseases (table 1.3) is relatively short: Pneumocystis Jiroveci Pneumonia (PCP) rather than Aspergillosis, Kaposi’s sarcoma and Lymphoma rather than tumors of other types.

Table 1.3. Indicator Conditions in the Case Definition of AIDS in Adults (The listed numbers and percentages indicate the frequencies of occurrence in the database of the Swiss HIV cohort study, an ongoing registry of more than 11,000 patients).

Condition	*n* (%)
Candidiasis of esophagus, trachea, bronchi, or lungs	3846 (16)
Cervical cancer, invasive	144 (0.6)
Coccidioidomycosis, extrapulmonary	74 (0.3)
Cryptococcosis, extrapulmonary	1168 (5)
Cryptosporidiosis with diarrhea for more than 1 month	314 (1.3)
Cytomegalovirus of any organ other than liver, spleen, or lymph nodes; or of eye	1638 (7)
Herpes simplex with mucocutaneous ulcer for more than 1 month, or bronchitis, pneumonitis, or esophagitis	1250 (5)
Histoplasmosis, extrapulmonary	208 (0.9)
HIV-associated dementia (disabling cognitive or other dysfunction interfering with occupation or activities of daily living)	1196 (5)
HIV-associated wasting [involuntary loss of more than 10% of baseline weight, plus chronic diarrhea (2 or more loose stools daily for 30 days or more), or chronic weakness and documented enigmatic fever for 30 days or more]	4212 (18)
Isospora belli infection with diarrhea for more than 1 month	22 (0.1)
Kaposi's sarcoma	1500 (7)
Lymphoma:	
Burkitt's	162 (0.7)
Immunoblastic	518 (2.3)
Primary central nervous system	170 (0.7)
Mycobacterium avium, disseminated	1124 (5)
Mycobacterium tuberculosis	
Pulmonary	1621 (7)
Extrapulmonary	491 (2)
Nocardiosis	– (<1)
Pneumocystis jiroveci pneumonia	9145 (38)
Pneumonia, recurrent bacterial (2 or more episodes in 12 months)	1347 (5)
Progressive multifocal leukoencephalopathy	213 (1)
Salmonella septicemia (non-typhoid), recurrent	68 (0.3)
Strongyloidiasis, extraintestinal	None
Toxoplasmosis of internal organ	1073 (4)
Wasting syndrome because of HIV	1980 (18)

Most of the opportunistic diseases are caused by reactivation of latent herpes viruses (for example, cerebral lymphoma resulting from Epstein–Barr virus, or retinitis from Cytomegalovirus (CMV)), by fungi (PCP), or by bacteria (Tuberculosis). Other infections—such as Salmonellosis or Cryptococcosis—may be newly acquired.

Clinical manifestations

The incubation period for symptomatic infection is 2 to 4 weeks, but can be as prolonged as 10 weeks. Onset of fever can be abrupt and is associated with diffuse lymphadenopathy and pharyngitis. The throat is usually erythematous, without exudates or enlarged tonsils. Painful ulcers can develop in the oral and genital mucosa. Gastrointestinal complaints are common, with many patients experiencing nausea, anorexia, and diarrhea. A skin rash often begins 2 to 3 days after the onset

of fever and usually involves the face, neck, and upper torso. The lesions are small pink-to-red macules or maculopapules. Headache is another prominent symptom, and aseptic meningitis is noted in about one quarter of patients. Headache is often retro-orbital and worsened by eye movement.

Findings in the CerebroSpinal Fluid (CSF) are consistent with viral meningitis: lymphocytes, normal glucose, and mildly elevated protein. Guillain–Barré syndrome and palsy of the VII th cranial nerve have been reported. Peripheral leukocyte count may be normal or slightly below normal, with a decrease in CD4 lymphocytes and an increase in CD8 lymphocytes (the CD4/CD8 ratio is commonly below 1). Liver transaminase values may be moderately elevated. The illness is self-limiting, with severe symptoms usually resolving over 2 weeks. Lethargy and fatigue may persist for several months (Southwick, 2007).

1.4 Cardiovascular complications

AntiRetroviral Therapy (ART) has led to a dramatic reduction in Acquired Immunodeficiency Syndrome (AIDS)-related morbidity and mortality and HIV infection has become a chronic condition. With the introduction of more potent drugs, co-formulations and once daily to take drug regimens, patients with excellent adherence and immunological response may expect a life expectancy similar to non-HIV-infected individuals. In parallel, a concomitant increase in morbidity and death not directly related to HIV was noted. Among the many comorbidity conditions, Cardiovascular Diseases (CVDs) have become of particular concern due to antiviral-drug-induced metabolic changes, the high prevalence of cardiovascular risk factors in HIV-infected individuals, and growing evidence on HIV-accelerated inflammatory processes that are known to promote atherosclerosis (see figure 1.1). Substantial differences in cardiovascular risk profiles in HIV-infected compared with uninfected individuals were noted in a routinely collected data analysis from two large US hospitals between 1996 and 2004: among HIV-infected patients, a higher prevalence was found for smoking (38 vs 18%), hypertension (21 vs 16%), diabetes (12 vs 7%), and dyslipidaemia (23 vs 18%).

The D:A:D study (Data Collection of Adverse events of Anti-HIV Drugs) is one of the largest databases on cardiovascular risk factors with 33 308 HIV-infected patients. During the 10-year observation period (1999 to 2008), 289 of 2482 deaths in D:A:D were related to CVD [rate 1.60 deaths/1000 Person-Years (PY)]. In D:A:D, a substantial discrepancy between ART-treated and treatment-naıve patients with regard to raised triglyceride and total cholesterol levels was found. Although more HIV-infected patients are treated with lipid and blood pressure-lowering drugs, data from a large cohort study indicates that only modest decreases in lipid and blood pressure values were noted over time.

1.4.1 Dyslipidaemia

Following HIV infection, a decrease in total cholesterol, HDL cholesterol, and LDL-cholesterol but increase in triglycerides has been observed in untreated individuals. After initiation of ART, marked increases in total cholesterol, LDL-cholesterol, and triglycerides are seen with HDL-cholesterol remaining low. The extent of lipid changes

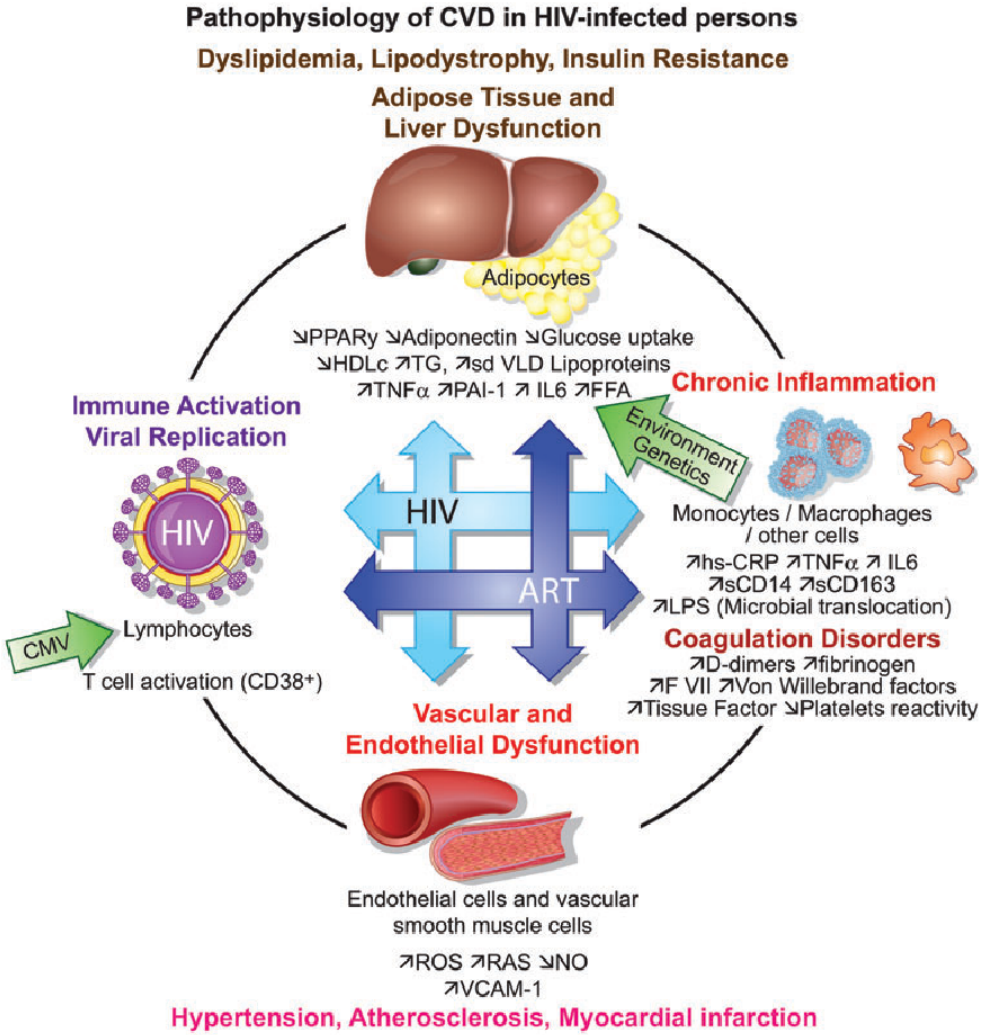

Figure 1.1. Hypothetical model for the pathogenesis of cardiovascular disease in HIV-infected persons taking antiretroviral therapy based on a figure from Boccara et al. (Boccara et al., 2013) (used with permission from Elsevier).

differs between antiretroviral drugs and drug classes. First-generation compared with second-generation protease inhibitors (PIs; e.g. Indinavir, Lopinavir vs. Atazanavir, and Darunavir) lead to higher increase in total cholesterol, LDL-cholesterol, and triglycerides, whereas non-nucleoside reverse transcriptase inhibitors (NNRTI; like Efavirenz) lead to higher increase in total and LDL-cholesterol compared with newer PIs. Typically, increases in triglycerides are the most prominent lipid changes in ART recipients. However, elevation of triglycerides carries only a spurious extra risk for CHD in analyses adjusting for all remaining lipid parameters and other CHD risk factors. Antiretroviral therapy-induced lipid changes are in particular driven by a change in particle size with a preponderance of highly atherogenic small dense lipoproteins. Small dense lipoproteins are increased in HIV-infected patients

with a CHD event and may be associated with a small additional risk for a CHD event independent from other lipid parameters. In HIV-infected individuals, basal lipolysis and hepatic de novo lipogenesis are increased, ability of insulin to suppress lipolysis in adipocytes is reduced, and peripheral fatty acid trapping is impaired. These mechanisms might be directly induced by HIV, in particular due to circulating inflammatory cytokines like interferon alfa.

1.4.2 Lipodystrophy

Human immunodeficiency virus-infected patients may also experience important changes in body fat composition following exposure to ART. Patients may develop lipoatrophy in the face and limbs or lipohypertrophy with central visceral fat gain, increase in breasts or ectopic fat deposition in liver, muscles, or adipose tissue and develop, for example, a buffalo hump . Some patients may experience both lipohypo- and hypertrophy. Nearly half of the patients with long-term ART exposure develop changes in body composition. An Italian study found incidence rates of lipoatrophy and fat accumulation of 8.2 and 4.8 per 100 PY, respectively. Simple anthropomorphic measures like waist circumference are highly correlated with MRI-based anthropomorphic measure of fat distribution and should therefore be used for routine monitoring in ART recipients. Lipohypertrophy and visceral fat deposits in individuals receiving ART is frequently associated with dyslipidaemia and hypertriglyceridemia, low-HDL-cholesterol, reduced insulin sensitivity, and diabetes. These metabolic changes resemble those found in HIV-negative individuals with metabolic syndrome. Mechanisms for lipohypertrophy are highly complex, different from those for lipoatrophy, and not known in detail, but include elevation of inflammatory cytokines, high levels of circulating triglycerides, and free fatty acids that are stored in the visceral fatty tissue and the liver. Increased levels of high-sensitivity C-reactive protein, adiponectin, tumour necrosis factor-a, and Il-6 have been found in HIV-infected men with lipohypertrophy similar to those seen in obese non HIV-infected men. Individuals with peripheral lipoatrophy and central lipohypertrophy have increased Framingham risk scores and higher coronary calcium scores and are thus at increased risk for CHD. In a nested cohort study, lipoatrophy and lipohypertrophy were both associated with increased overall mortality. Unfortunately, changes in body composition cannot be reverted to a clinically relevant extent in most patients and are typically seen in HIV-infected patients with long-time exposure, in particular, to first generation antiretroviral drugs.

1.4.3 Insulin resistance and diabetes

The incidence of type II diabetes in the D:A:D study was 4.2 per 1000 PY. Low CD4 cell count (200 cells/mL) and lipodystrophy have been reported as HIV-related factors associated with type II diabetes. In analyses of D:A:D and a recent analysis from Denmark, none of the newer antiretroviral drugs significantly contributed to the increased risk of diabetes (in contrast to previous observations with older drugs). It appears that antiretroviral drug-induced risk of diabetes is associated with the use of PIs of the first-generation and with Thymidine-containing analogues Reverse Transcriptase Inhibitors that have known mitochondrial toxicity. In non-

resource-limited settings, these drugs have now been greatly replaced in HIV care. Mitochondrial toxicity may lead to impaired insulin sensitivity, and in vitro models indicate that first generation PIs block glucose transporter GLUT4 and may also affect glucose-sensing b-cells, both causing impaired glucose sensitivity. Other factors that may be associated with an increased risk of diabetes are high-sensitivity C-reactive protein and tumor necrosis factors 1 and 2.

1.4.4 Chronic inflammation

A growing body of data indicate that HIV-related inflammatory and immunologic processes may contribute to additional risk for cardiovascular events in HIV-infected patients. Most convincing evidence for such a mechanism comes from the unanticipated findings from the SMART trial. In SMART, HIV-infected were assigned to continuous use of ART (viral suppression group) or treatment interruption (drug conservation group) with deferral of therapy until a CD4+ count decrease, 250 cells/mL. The trial rationale was to limit ART-related toxicity and cardiovascular side effects. The trial was stopped prematurely, because patients in the drug conservation arm experienced a higher hazard for AIDS or death. Intriguingly, patients in the drug conservation group compared with the viral suppression group also experienced more CVD events (1.3 vs. 0.8 events per 100 PY; HR 1.6; 95% CI, 1.0 –2.5). Subsequent studies from SMART showed that ART interruption was associated with significant increases in blood levels of interleukin-6 (IL-6) and D-dimer. Interleukin-6 is a non-specific inflammatory biomarker (like high-sensitivity C-reactive protein) and D-dimer is a fibrin degradation product which primarily reflects increased activity in the thrombotic process and may be elevated in response to inflammatory stimuli and bacterial translocation. Chronic inflammatory processes in endothelial cells that promote atherosclerosis represent a very complex interplay of inflammatory cells with lymphocyte and macrophage activation, damage to the mucosal barrier, metabolic changes, and other factors directly or indirectly related to HIV replication. Higher levels of IL-6, high-sensitivity C-reactive protein, and D-dimer were associated with increased all-cause mortality and predicted CVD independent of other risk factors. However, the model improvement for risk prediction when added to the Framingham risk score was modest. There is further evidence that HIV-infected individuals with advanced immunosuppression (200 CD4 cells/mL) and not fully suppressed viral load (0.5 copies/mL) have a higher prevalence of elevated Il-6, D-dimer, and soluble CD14 than HIV-uninfected individuals of similar CVD risk. Human immunodeficiency virus may lead to a compromised mucosal barrier resulting in subsequent translocation of microbial products, such as lipopolysaccharide that bind to soluble CD14 and may lead to systemic immune activation. Soluble CD163 is expressed by macrophages in atherosclerotic plaques, correlates well with arterial inflammation as measured with fluorine-2-deoxy-D-glucose positron emission, and may be a more promising marker for endothelial inflammation in HIV infection. In a study of ART-treated patients with well-suppressed viral load, arterial inflammation in the aorta was higher than in HIV negative healthy controls and of similar magnitude as in HIV-negative patients with established atherosclerosis. Findings from this study are particularly intriguing because all HIV-infected patients had been well treated for years and this may indicate that endothelial inflammation in HIV infection may

persist independently from ART. Endothelial cells that are altered by injury or inflammation express chemokines and vascular cell adhesion molecule-1 (VCAM-1) which have a prominent role for attracting monocytes and promoting inflammatory cell entry. Soluble VCAM-1 is increased in HIV infection and evidence from randomized controlled trials (RCTs) indicates that ART reduces this endothelial activation marker. Similar core mechanisms of inflammation have been described in the adipose tissue and adipocytes leading to the release of inflammatory mediators or the migration of inflammatory cells into adipose tissue and the exertion of systemic inflammatory responses. These similarities are of particular interest in HIV infection because HIV and certain antiretroviral drugs can induce important metabolic and body fat mass changes.

1.5 Clinical cardiovascular disease endpoints

A number of observational and experimental studies have examined the effect of ART and risk for CVD. The more recent observational data meta-analysis by Bavinger et al. (2013). showed an increased risk of Myocardial Infarction (MI) associated with recent exposure (e.g. within the last 6 months) to Abacavir, a reverse transcriptase inhibitor (RR: 1.91; 95% CI: 1.50 –2.42) and PIs (RR: 2.13, 95% CI: 1.05–1.17). Alternative analyses for cumulative ART exposure suggest an increased risk for MI with each additional year of treatment with the first-generation PIs Indinavir (RR: 1.11, 95% CI: 1.05–1.17) and Lopinavir (RR: 1.22, 95% CI: 1.01–1.47). Studies included into these meta-analyses were of mixed quality, estimates between studies were heterogeneous and the summary findings, therefore, have to be interpreted with caution. Following the first publication of an increased risk of MI with Abacavir exposure by the D:A:D study investigators Cruciani et al. re-analysed in a meta-analysis all RCTs comparing Abacavir with control reverse transcriptase inhibitors that were provided by the manufacturer of Abacavir and a second analysis was conducted by the Federal Drug Administration (FDA). In both analyses, no increased risk of MI with Abacavir exposure was found. Myocardial infarction was a rare event in these analyses and of similar frequency like in the D:A:D study. Evidence from a few small studies indicates that in HIV-infected individuals MI with ST elevation (STEMI) appear to be slightly more frequent than non-STEMI. Overall, based on the available evidence, it is unclear whether there is an increased risk for MI associated with current Abacavir use. A potentially existing absolute risk increase with Abacavir use would be moderate and needs to be put into perspective with the massive benefit from ART and possible side effects from other reverse transcriptase inhibitors (Hemkens and Bucher, 2014).

1.6 Cardiovascular disease risk prediction

HIV-infected patients are at increased risk for CVD and therefore assessment of cardiovascular risk should be routinely and regularly done in all patients and particular in those receiving ART. The coronary risk is defined as the probability to have a major cardiovascular event (angina pectoris, myocardial infarction) in a specific period of time (generally 10 years). It can be calculated by several algorithms:

- **Framingham score** Calculates the probability of a cardiovascular event in a specific period of time (usually 5-10 years), on males and females, between 35 and 70 years. It's based on age, gender, systolic and diastolic blood pressure, total and HDL cholesterol levels, the presence of diabetes and smoking status. The patients are classified as having low (<10%), medium (10 to 20%) or high (>20%) cardiovascular risk.

- **Procam** Calculates the probability of a cardiovascular event in a population of males, between 40 and 65 years, in a specific period of time of 8 years. It takes into account gender, age, serum HDL and LDL cholesterol and triglyceride levels, smoking status, diabetes, family history of coronary heart disease and systolic blood pressure. The patients are classified as having low (<10%), medium (10 to 20%) or high (>20%) cardiovascular risk. Score is based upon gender, age, systolic blood pressure, smoking status and total cholesterol/HDL cholesterol ratio. The patients are classified as having low (<1%), medium ($\geq$ 1 to $<$ 5%), high ($\geq$ 5 to $<$ 10%) or very high ($\geq$ 10%) cardiovascular risk.

- **DAD risk equation** Takes into account age, gender, total and HDL cholesterol, smoking status (current or past), blood pressure, history of diabetes, family history of CVD, and exposure to Indinavir, Lopinavir and Abacavir. They are classified as having low (<1%), moderate (1 to 5%), high (5 to 10%) or very high (>10%) risk of CHD over a 5-year period. High and very high risk patients were subsequently grouped into a single high risk category ($\geq$ 5%) to simplify comparison (Pirš et al., 2014).

PLWH are prone to develop sub-CV disease, despite the effectiveness of cART. Algorithms developed to predict CV risk in the general population could be inaccurate when applied to PLWH. One of the objectives of this thesis is to find a new algoritms to predict CV risk.

Chapter 2

Cardiac CT Principles

In the modern era, cardiac computerized tomography (CCT) provides a robust non-invasive assessment of Coronary Artery Disease (CAD) with a high degree of accuracy. It is capable of providing anatomical information about plaque stenosis and composition, and is now recommended in national guidelines. Its beginnings, however, were humble, and mainly of an exploratory nature. The evolution of CCT is directly proportional to the growing clinical demand for better imaging and the technological improvements seen with successive generations of scanners. This continuous evolution has now enabled coronary assessment with a high degree of accuracy at low levels of radiation for both acute and stable lesions. The invention of the CT scanner in 1971 is credited to Sir Godfrey Hounsfield, an English engineer, and Dr. Allan Cormack, a South African physicist, with the first human CT performed on a patient's brain in London (Hounsfield, 1973). Eight years after their invention, Hounsfield and Cormack were jointly awarded the Nobel Prize in Physiology or Medicine. Since then, the use of CT has expanded dramatically to include many organs, eventually incorporating the heart, first with coronary Calcium Scores (CS) and then coronary CT Angiography (CTA).

2.1 Coronary Calcium Score

Coronary artery calcium, as seen in established coronary atherosclerosis, results from the buildup of substances over time which have hardened and become calcified. The histological atherosclerotic process was classified by Stary et al. (1995), with calcification involved in the later stages. The presence of calcium suggests established CAD, with the CS calculating the total amount of coronary artery calcified plaque present collectively within all the coronary arteries (see figure 2.1). The first report regarding the ability of CT to measure CS was published by Guthaner et al. (1979), although it was Agatston et al. (1990) who introduced a practical application of CS. The technique proposed by Agatston for producing a standardized reproducible score has remained the standard method to the present day. The Agatston score is calculated using both the area and a weighted value related to the density of calcification. Any structure with a density greater than 130 Hounsfield units (HU) and with an area of 1 mm^2 or greater is quantified as a calcified focus. Foci within the anatomic site of coronary arteries represent calcified CAD plaques. The minimum

area of 1 mm^2 (comprising at least 2 pixels) required to be counted as part of the CS ensures that a single pixel, which could represent image noise, would not be counted. The area of foci is then multiplied by a density measurement conversion factor. A score of 1 is assigned for a value of 130–199 HU, a score of 2 for 200–299 HU, 3 for 300–399 HU, and 4 for values of 400 HU and higher. The weighted score is then multiplied by the area of the coronary calcification to calculate the Agatston score. A CS is obtained using a non-enhanced scan that produces a series of stacked transaxial images, which is associated with relatively low radiation exposure. Agatston scores are now calculated using a semi-automated analysis package validated algorithm.

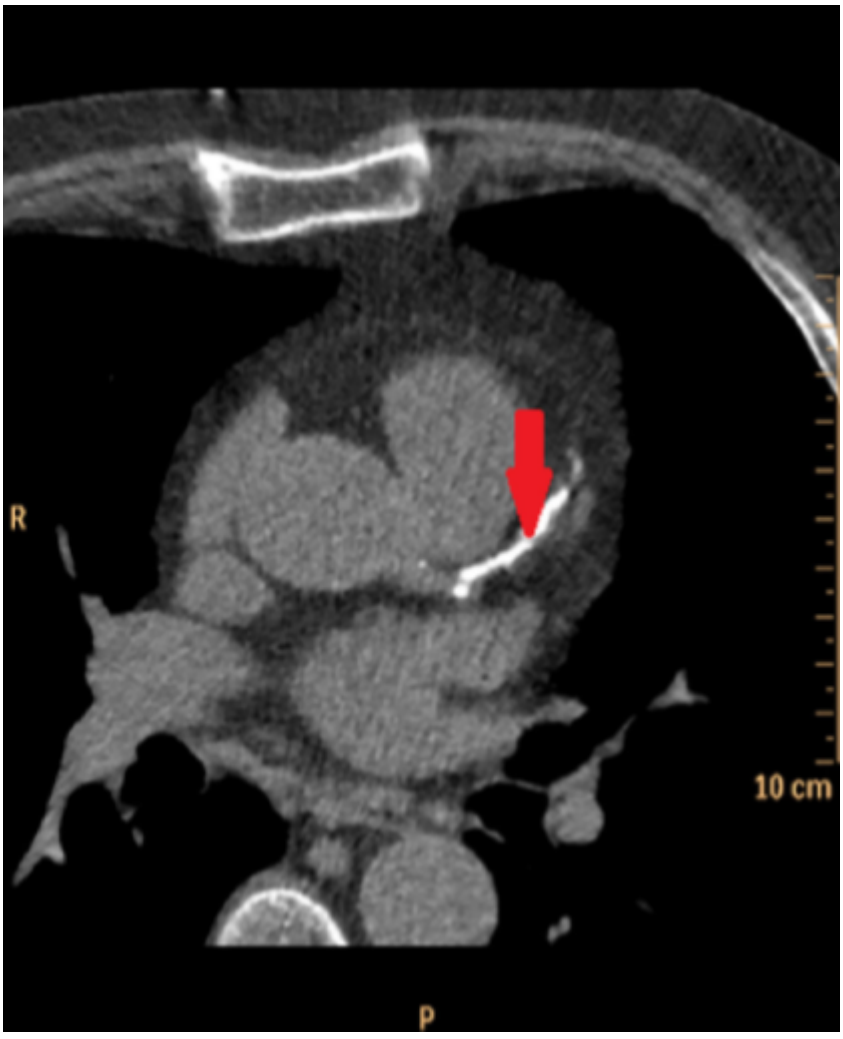

Figure 2.1. Coronary calcium within the left anterior descending artery. The calcium is seen as bright white and is highlighted by arrow.

2.2 Computerized Tomography Coronary Angiography

In the 1970's, attempts were made to image coronary arteries using CT, but the effects of rapid cardiac motion and long acquisition times resulted in images

of poor quality, with no practical value. In the 1980's, the detection of coronary arteries was possible, but the identification of stenosis for clinical purposes was not. Consequently, cardiac coronary CTA was virtually abandoned for a long period, and was seen as nothing more than a research tool. However, the introduction of helical CT systems in the late 1990's signaled the modern era of CCT with the creation of 16-slice scanners, and consequently the opportunity for clinical use of coronary CTA. Over the next few years, the number of detectors increased to 64, enabling greater clinical accuracy. Although artefacts have not been completely eliminated from CCT, the diagnostic performance of the standard 64-slice scanner is now well established. In particular, it has demonstrated high negative predictive value, ranging from 98% to 100% reliability, in excluding CAD. The ability of CCT to detect significant coronary stenoses has been validated against conventional coronary angiography and intravascular ultrasound. The evolution of this imaging technology has continued, with the number of detectors increasing, resulting in the wide availability of 128, 256, and 320 detector row scanners in clinical practice. This progression is ongoing, with 640 detector row scanners now citing even less radiation and scanning time, as well as improved image quality. Coronary CTA has the capacity to visualize the coronary arteries without the risks associated with invasive assessment. It can provide comprehensive information regarding coronary anatomy, the presence of obstructive and non-obstructive CAD, and plaque characteristics. This information can be used to predict long-term outcomes, as both plaque burden and non-obstructive disease have been associated with adverse prognosis. Conversely, the prognosis is excellent in the absence of disease. A meta-analysis by Hulten et al. (2011), in which 9592 patients were evaluated over a median follow-up of 20 months, found that the absence of CAD on coronary CTA was associated with a 0.17% annual rate of major adverse cardiac events, compared to 8.8% among patients with obstructive disease. Coronary CTA is performed by the injection of contrast into a peripheral vein, and images are obtained when the contrast reaches the coronary arteries (see figure 2.2).

The images are acquired relative to the patient's electrocardiogram (ECG) produced by surface electrodes. The R–R interval[1] of the ECG cycle is typically divided into phases which involve both the systolic and diastolic stages of the cardiac cycle. For most persons, the maximum relaxation of the heart is the best time to acquire images, which is approximately 75% along the R–R interval in mid-diastole. Methods of image acquisition can be either retrospective or prospective. Retrospectively gated studies use X-ray beams throughout the R–R interval. This was traditionally associated with a high level of radiation in full-dose retrospective studies.

It is now common practice, however, to use ECG dose modulation, which increases the dose of radiation around 75% along the R–R cycle in order to optimize the image without constant high levels of radiation. Retrospective studies use spiral scanning during table motion and more traditional cone beam reconstruction. This offers the ability to reconstruct images at various time points, potentially creating

[1]The time elapsed between two successive R waves of the signal on the electrocardiogram (and its reciprocal, the Heart Rate), is a function of intrinsic properties of the sinus node as well as autonomic influences.

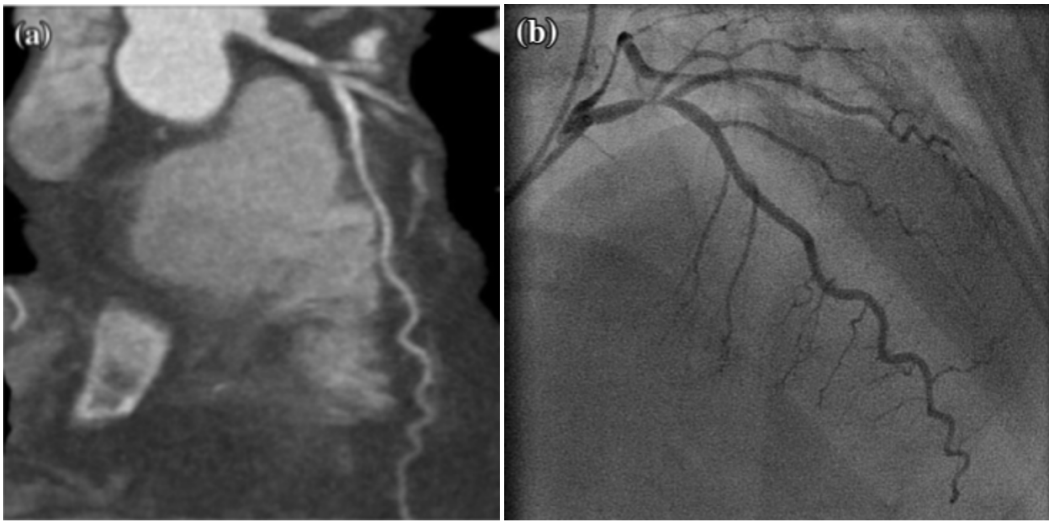

Figure 2.2. Comparison of coronary CTA and ICA. (a) Coronary CTA showing a severe proximal left anterior descending artery lesion. (b) ICA of the same patient. (CTA computed tomography angiography, ICA invasive coronary angiography), from Hulten et al. (2011).

greater diagnostic reassurance, and also the ability to assess left ventricular function. However, despite ECG dose modulation, retrospective studies are still associated with a higher radiation dose than prospective studies. Prospective studies use forward prediction of R wave timing, with no table motion during imaging, and non-spiral acquisition. Here, essentially, the radiation/image acquisition is turned on over several heartbeats when the predefined point in the R–R cycle is detected, which is generally 75% along the cycle. During the rest of the ECG cycle, there is no image acquisition or radiation exposure, resulting in a smaller radiation dose compared to retrospective studies. Prospective studies, however, generally require a slower steady constant heart rate, without which image acquisition may not occur at every heartbeat. Consequently, there may be a longer acquisition time than in retrospective studies, rendering it more vulnerable to heart rate and breathing artefacts.

2.3 Analysis of plaque characteristics

Most Acute Coronary Syndromes (ACS) are caused by atherosclerotic plaque rupture, causing sudden luminal thrombosis. The prediction of specific plaques that may rupture may be possible through coronary CTA plaque analysis. In 2007, Motoyama et al. compared the plaque characteristics of patients with ACS and stable angina, and concluded that plaque characteristics associated with ACS included Positive-vascular Remodeling (PR), Low Attenuation Plaque (LAP), non-calcified plaque, and Spotty Calcification (SC), which were not present instable angina patients. In further work by the same author, which followed over 1000 patients who experienced an ACS event post-coronary CTA, again found that PR and LAP

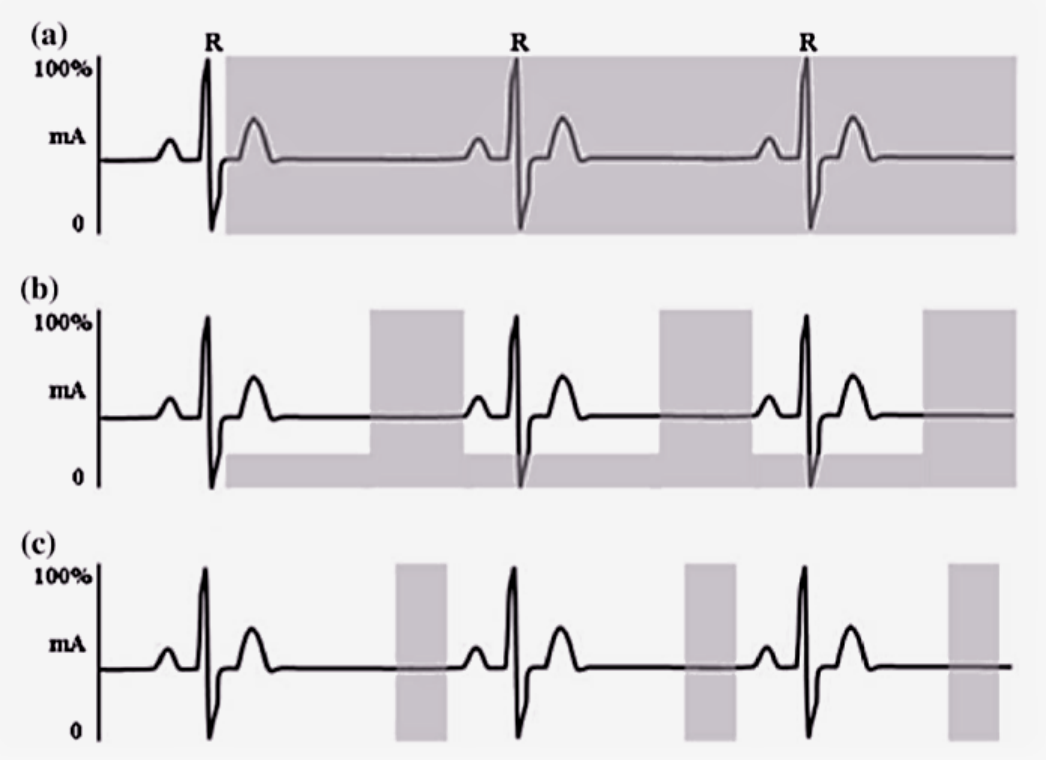

Figure 2.3. Diagram illustrating image acquisition (and thus radiation exposure) during the different types of gating. (a) Full dose retrospective gating, with a constant high level of radiation. (b) Electrocardiogram tube dose modulation, with a constant low level of radiation, which is increased during mid-diastole when the main part of the image is acquired. (c) Prospective imaging during which the image acquisition (and thus radiation exposure) occurs only at pre-set intervals, again generally during mid-diastole. (Reproduces from Weustink and de Feyter (2009)).

were predictors of ischemia culprit lesions. More recent work, also by Motoyama et al. (2007), with long-term follow-up has once again suggested that patients with high-risk features on CTA are likely to develop ACS at a significantly higher rate. ACS occurred in 23% of patients with two high-risk features, 10.7% of patients with one high risk feature, 1.6% of patients with no such features, and 0.6% of patients without any plaque. Another interesting plaque characteristic is the Napkin Ring Sign (NRS), which has been defined as a ring-like peripheral higher attenuation of the non-calcified portion of a coronary plaque. It indicates a rupture-prone plaque, comprising a necrotic core covered by a thin cap, also referred to as so-called thin-cap fibroatheroma. The presence of a fibroatheroma thin cap itself, however, cannot be detected by coronary CTA due to limited spatial resolution. The NRS has also been shown to predict advanced lesions and ACS events. Recent plaque analysis from the ROMICAT (Rule Out Myocardial Infarction/Ischemia Using Computer-Assisted Tomography) study has also demonstrated the importance of ACS plaque characteristics such as PR, LAP, NRS, and SC. In patients presenting with acute chest pain but negative initial ECG and Troponin, the presence of high-risk plaques on coronary CTA is said to increase the likelihood of ACS independent of significant

CAD and clinical risk assessment (age, sex, and number of cardiovascular risk factors). These high-risk plaque features may represent a way of identifying patients most at risk, although routine clinical assessment for them has not yet been widely adopted, presumably due to the difficulty of recognition and unclear management. Nevertheless, their detection offers hope for the identification and management of ACS-prone patients.

2.4 Cardiac computed tomography radiations exposure

Although the diagnostic importance of CT is undisputed, it does expose patients to radiation, and thus the worry of malignancy. In general, CT is estimated to account for approximately 50–70% of radiology-induced radiation exposure overall, but only 15% of all radiological examinations. The number of cardiac investigations using radiation is also rising more rapidly than non-cardiac methods. The concern with radiation is particularly high in cardiac patients given the potential cumulative dose that repeated investigations and therapy may produce. Radiation-induced cancers cannot be distinguished from other tumors, and consequently it is only by epidemiological studies that the rate of radiation-induced cancer can be detected. The exact degree to which imaging radiation exposure contributes to cancer remains unknown, but research has suggested that there is no increased cancer risk associated with radiation exposure less than 20 mSv. The effects of radiation on human tissue can be divided into two fundamental types:

- Non-stochastic (deterministic) effects: are dose-dependent, and occur only once a threshold has been reached, with the severity increasing with higher radiation dose. With deterministic effects, the radiation itself causes cell damage or death and thus functional impairment of the tissue. These effects are generally acute reactions, and include hair loss, cataracts, skin burns, bone marrow suppression, and diminished fertility. Deterministic effects are not routinely encountered in CT, but would be expected at higher doses.

- Stochastic effects: are caused by the radiation effect on cell division. As the word “stochastic” itself suggests, these effects are more random in nature, likely the result of long-term events and not a definite physical outcome. The higher the dose absorbed, the higher the likelihood of an event, although the dose received does not predict the severity of the effect. As such, stochastic effects are seen as independent of the absorbed dose and follow a linear no-threshold hypothesis. The two common types of stochastic effects are malignancies and heritable disease in offspring. Cancers post-exposure have a latency period thought to be approximately 5–10 years for solid tumors and 2 years for leukemia.

For years, physicians have battled with the issue of image quality versus radiation dose. The past few years have witnessed unprecedented advances in reducing radiation exposure, with now standard practices such as retrospective tube dose modulation and prospective axial ECG-triggered gated image acquisition. Other methods include individualized protocol selection, bismuth breast shields, and the rebirth of iterative reconstruction (McKavanagh et al., 2015).

2.5 Indications for CTA

Although CCT is experiencing exponential growth, with an increasing number of applications, the health community is working on defining appropriateness criteria for the correct use of this technique. Appropriate indications for CCT are as follows:

(i) chest pain, intermediate pretest probability for CAD (ECG cannot be interpreted or patient is unable to exercise), persistent chest pain after equivocal stress test, or suggestion of coronary anomalies;

(ii) acute chest pain in emergency department: intermediate pretest probability for CAD (no changes in ECG and negative enzyme test results);

(iii) pulmonary vein isolation, biventricular pacemaker implantation, or coronary arterial mapping in repeat cardiac surgery;

(iv) cardiac masses or pericardial disease with technically limited images from echocardiogram, MRI, or trans-esophageal echocardiography;

(v) complex congenital heart disease, assess anatomy.

Uncertain indications for CCT are as follows:

(i) chest pain: intermediate pretest probability for CAD (ECG can be interpreted and patient is able to exercise) or low or high pretest probability for CAD (no changes in ECG and negative enzyme test results);

(ii) acute chest pain: rule out obstructive CAD, aortic dissection, and pulmonary embolism if the pretest probability for one of them is intermediate;

(iii) high risk of CAD in asymptomatic patients;

(iv) chest pain after revascularization (percutaneous intervention or coronary artery bypass grafts): evaluate bypass grafts or history of revascularization with stents;

(v) intermediate perioperative risk of cardiac events in patients undergoing intermediate or high-risk non-cardiac surgery;

(vi) valvular disease (native or prosthetic valves) with technically limited images from ECG, MRI, or transesophageal echocardiogram.

The indiscriminate use of CCT in low-risk populations is not justified, given the risks associated with ionizing radiation and intravenous iodinated contrast material. Image quality can compromise diagnostic accuracy in patients with irregular or fast heart rates, morbid obesity, severe calcifications, or coronary stents. New scanners with acquisitions of up to 256 slices per rotation or multiple x-ray tubes have been developed to seek to improve temporal and spatial resolution and reduce artifacts (Prat-Gonzalez et al., 2008).

2.6 Limitations of Cardiac Computed Tomography

In addition to radiation exposure, there are several other limitations of CCT. The 64-detector system takes a number of cardiac cycles to acquire images, and as such is prone to patient motion, arrhythmias, and patient breath-hold failure, which can produce motion artefacts and diagnostic uncertainty. Newer 256- and 320-detector scanners with faster gantry rotation times, increased X-ray tube power, and shorter scanning time have improved, but not eliminated, this tendency for artefacts. Other issues with CCT include the need for beta-blockers and sublingual nitrate, potential allergic contrast reactions, poor contrast filling of distal vessels resulting in diagnostic uncertainty, and contrast-induced renal toxicity. In comparison to invasive angiography, CCT frequently overestimates the degree of coronary stenosis. There are several reasons for this. First, the presence of coronary calcium can cause blooming artefacts, increasing the perceived level of stenosis. Second, the potential for motion artefacts can make lumen assessment difficult. Third, inherent differences exist between the two techniques, with invasive angiography allowing the assessment of lumen with precise classification of stenosis, while CT is a tomographic approach that provides an estimate of overall plaque burden. The accuracy of 64-slice CT was addressed in a recent review which reported sensitivity of 89% (95% CI: 87–90), specificity of 96% (95% CI: 96–97), and positive and negative predictive values of 78% (95% CI: 76–80) and 98% (95% CI: 98–99), respectively. The excellent capacity of CT for excluding disease means that it is recommended in low- to medium-risk patients (McKavanagh et al., 2015).

2.7 The future of Cardiac Computed Tomography

There is a large body of published studies involving other uses of coronary CTA not previously mentioned, such as in structural heart disease intervention, bypass graft assessment, congenital heart disease, and acute chest pain. These well-established indications, together with UK, US, and European guidelines now advocating its use, will ensure that CCT adoption will continue to grow. Nowadays CCT is considered to be the first test for the diagnosis and management of Chronic Coronary Syndrome, according to the European Society of Cardiology (2019).

In patients in whom CAD cannot be excluded by clinical assessment alone, non-invasive diagnostic tests are recommended to establish the diagnosis and assess the event risk. The current Guidelines recommend the use of either noninvasive functional imaging of ischaemia or anatomical imaging using coronary CT Angiography (CTA) as the initial test for diagnosing CAD. Anatomical non-invasive evaluation, by visualizing the coronary artery lumen and wall using an intravenous contrast agent, can be performed with coronary CTA, which provides high accuracy for the detection of obstructive coronary stenoses defined by ICA, because both tests are based on anatomy. The presence or absence of non-obstructive coronary atherosclerosis on coronary CTA provides prognostic information, and can be used to guide preventive therapy. The SCOT-HEART (Scottish Computed Tomography of the HEART) trial demonstrated a significantly lower rate of the combined end point of cardiovascular death or non-fatal MI (2.3 vs. 3.9% during 5 year follow-up) in

patients in whom coronary CTA was performed in addition to routine testing, which consisted predominantly of exercise ECG. Other randomized, prospective clinical trials have demonstrated that diagnostic testing with coronary CTA is associated with clinical outcomes similar to those for functional imaging in patients with suspected CAD. In patients with extensive CAD ,coronary CTA complemented by CT-based FFR was non-inferior to ICA and FFR for decision-making, and the identification of targets for revascularization. Coronary CTA is the preferred test in patients with a lower range of clinical likelihood of CAD, no previous diagnosis of CAD, characteristics associated with a high likelihood of good image quality, local expertise and availability and information on atherosclerosis desired. It detects subclinical coronary atherosclerosis, but can also accurately rule out both anatomically and functionally significant CAD (Knuuti et al., 2020).

Chapter 3

ECV: from Cardiac MRI to CT

Myocardial fibrosis is a frequently unwanted, common end point in the majority of pathological mechanisms affecting heart muscle. It can occur as focal scarring due to replacement fibrosis following myocyte death (apoptosis, autophagy or necrosis) or as diffuse fibrosis due to expansion of the collagen fiber network around individual myocytes or myocyte bundles. The best non-invasive technique for visualizing focal fibrosis is Cardiovascular Magnetic Resonance (CMR) using Late Gadolinium Enhancement (LGE), because of the high contrast, high spatial resolution and whole heart coverage. Although resultant image quality is currently reduced, myocardial fibrosis can also be assessed with Cardiac Computed Tomography (CCT); both use an extracellular, extravascular contrast agent that lingers in extracellular water in areas of scar, due to a higher volume of distribution and slower kinetics. Visualization of diffuse fibrosis until now has remained challenging and limited to the domain of the pathologist, who was able to measure the Extracellular Matrix (ECM) directly on histological sections using stains specific for connective tissue. Coupled with this, no useful blood biomarkers of myocardial fibrosis are currently extant. In the last 7 years, the same contrast agents have begun to be used to measure diffuse interstitial expansion (as well as focal scar), by measuring the Extracellular Volume fraction (ECV).

3.1 Development of an Extracellular Contrast Agent

An extracellular contrast agent (ECA) has a key set of properties:

- homogeneous distribution;
- high water, but no fat solubility;
- not adsorbed, actively transported, protein-bound or metabolized;
- non-toxic, stable and freely cleared from the body;
- readily measurable.

Iodine and gadolinium compounds both fulfil these requirements as contrast agents. They diffuse rapidly and passively from the vascular space into extracellular tissue, but not into the intracellular space, leading to the term extracellular,

Extravascular Contrast Agent (ECA). Following an intravenous bolus, they enter the myocardium down a concentration gradient ("wash-in phase"), and later, while being cleared, they return to the blood pool down the reverse concentration gradient ("wash-out phase"). This occurs over seconds to minutes in healthy myocardium, but in scar tissue (focal or diffuse), these pharmacokinetics are delayed due to changes in coronary flow rates, capillary permeability, functional capillary density and the presence of a dense, hydrated collagen matrix. In addition, the increased volume of extracellular water present in scar compared to normal myocardium means total accumulation is higher. The combined result is that, at a certain time "late" after a bolus, there is more contrast agent in scar than in the blood or remote myocardium and measurable signal is therefore changed.

In CMR, gadolinium-based contrast agents (GBCAs) are used due to their unique magnetic properties (gadolinium is a paramagnetic material with the most unpaired electrons). They are particularly efficient T_1-relaxing agents, resulting in increased signal on T_1-weighted images and typically appearing bright on a T_1 inversion recovery image. The relaxation rate (R_1 or $1/T_1$) is directly proportional to the concentration of gadolinium. In CT, non-ionic iodinated contrast agents have become the most commonly used contrast agents; they are water soluble, extracellular, extravascular contrast agents, which are not metabolized and are excreted by the kidneys. CT attenuation values (represented as Hounsfield units, HU) are directly proportional to the concentration of iodine.

3.2 Extracellular Volume Imaging by CMR

Until recently, the gold standard of diagnosing diffuse fibrosis was endomyocardial biopsy, which is invasive and is prone to sampling errors. This has led to the development of new, non-invasive techniques to better quantify diffuse fibrosis. CMR allows non-invasive tissue characterization of the myocardium and as such, is being increasingly used to identify the aetiology of a range of Cardiomyopathies. LGE is the mainstay of this myocardial characterization and allows the detection of focal fibrosis. This technique combined with functional imaging is the main reason that CMR is so useful clinically. LGE imaging relies on the delayed post contrast difference in T_1 between areas of fibrosis (more gadolinium, shorter T_1) and healthy myocardium (less gadolinium, longer T_1), making it ideal for identifying focal areas of fibrosis. In diffuse fibrosis, this relative difference is lost, so conventional LGE imaging struggles being a difference test where the operator selects one normal tissue to null making all other tissues bright. GBCAs change tissue T_1; however, the native (non-contrast) T_1 also changes with pathology. Advances in CMR sequences now permit its quantification via T_1 mapping, which offers absolute values of T_1, rather than relative differences in signal intensity. Native T_1 describes the signal in the whole of the measured myocardium and therefore represents a composite signal from all species present; this signal is swamped by iron or gadolinium if present and in their absence is measuring the signal of both the cardiac myocytes and the ECM. Therefore, fibrosis, oedema, amyloid and associated water increase T_1, and conversely increased cellularity (athleticism), iron (Thalassemia) or fat (Anderson Fabry disease) decrease T_1.

The use of extracellular GBCAs in CMR offers the opportunity to quantify the extracellular (i.e. interstitial) space, relative to the intracellular (i.e. myocyte) space, which is the essence of ECV quantification. It dichotomises the myocardium into myocytes and matrix. In conjunction with myocardial volume, ECV can be used to calculate the relative volumes of each compartment. It is expressed as a volume fraction and provides us with unique insights into the pathophysiology of a range of myocardial diseases. T_1 mapping and ECV may provide an advantage over conventional LGE imaging, by enabling us to more accurately quantify diffuse fibrosis and potentially detect early fibrosis related changes not always detectable by LGE. Indeed, increases in ECV seen on CMR are associated with an increased mortality and may be as important to prognosis as left ventricular ejection fraction.

Typically, a paramagnetic contrast agent (0.1–0.2 mmol/kg) is injected into a patient to temporarily distribute in the extracellular space in the myocardium (Jellis et al., 2010). Under the condition of replacement myocardial fibrosis, the myocytes have been replaced by collagen fiber and the loss of viable cardiac cells results in an increased extracellular space where the contrast agent can accumulate in infarcted regions as shown in figure 3.1.

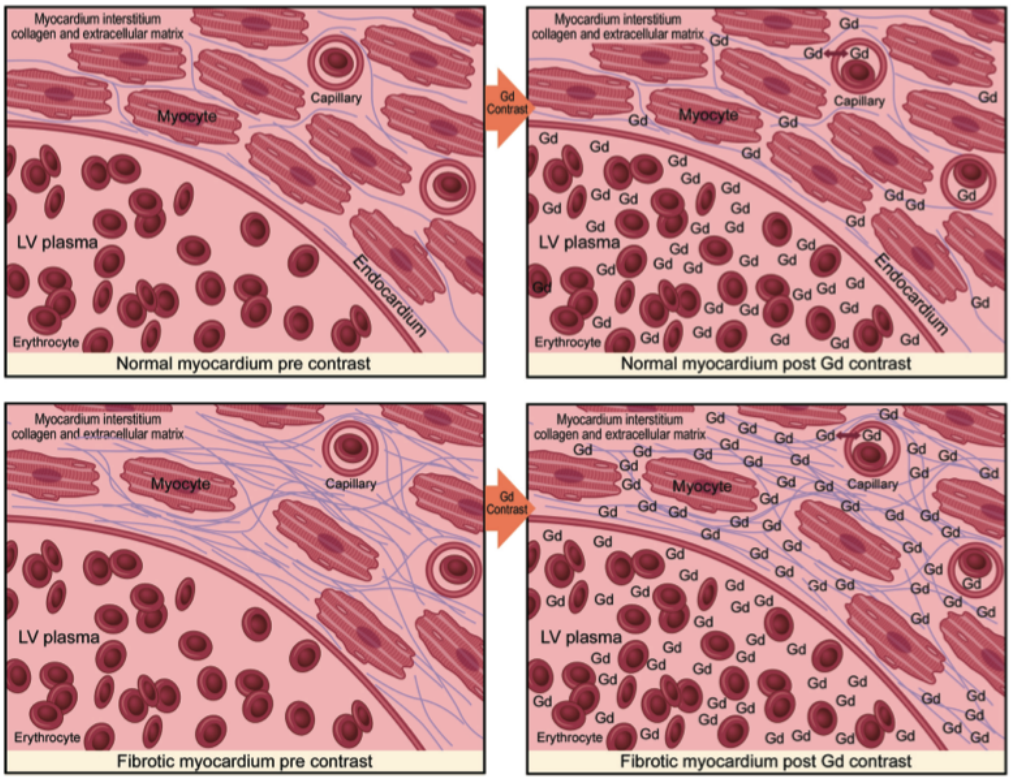

Figure 3.1. Pre and post contrast gadolinium (Gd) contrast dispersion in normal versus fibrotic myocardium, from Jellis and Kwon (2014).

The increased gadolinium concentration shortens the myocardial T_1 value, making higher signal intensity in scar tissue visible when an inversion recovery sequence is set to null the normal myocardium. LGE was initially developed for characterization

of myocardial damage after myocardial infarction (Jellis et al., 2010), (Pack et al., 2008). Using LGE ischemic scar appears bright in a subendocardial or transmural pattern following the vascular distribution of the major coronary arteries (Pack et al., 2008). Neverthless this technique presents some limitations. First, with conventional LGE sequences, signal intensity is expressed on an arbitrary scale that differs between scans and thus, is unsuitable for direct signal quantification in cross-sectional or longitudinal comparisons. Second, image contrast is on the basis of the difference in signal intensity between fibrotic and "normal" myocardium, and such differences may not exist if the myocardial fibrosis is diffusive because diffuse fibrosis will appear as normal. Thus, diffuse myocardial fibrosis cannot be detected by LGE, as signal intensity of each single voxel is a mixture which cannot represent the difference between normal and abnormal myocardium. Collagen often diffusively deposits in non-ischemic cardiomyopathy. Such interstitial fibrosis commonly shows no regional scarring on delayed contrast enhancement images and is often missed by LGE (Mewton et al., 2011; Flett et al., 2010). Although regional fibrosis is easily imaged with CMRI there is no noninvasive method for quantifying diffuse myocardial fibrosis and for this reason it has never been useful as a clinical marker. The only available method for assessment was invasive endomyocardial biopsy in which a small ($<1\ mm^3$) sample is obtained with biopsy forceps, typically from the right ventricular side of the distal myocardial septum during catheterization of the right side of the heart (example in figure 3.2). Even in those who undergo endomyocardial biopsy, results are limited by sampling bias (Becker et al., 1991).

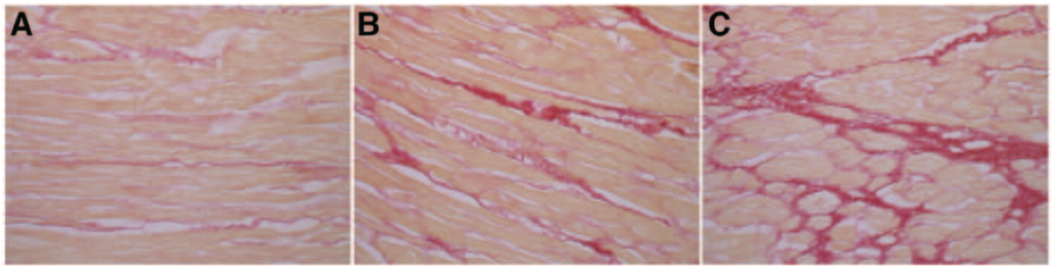

Figure 3.2. An example of histology to determine collagen volume fraction (CVF). Examples shown demonstrate (A) 8%, (B) 16%, and (C) 36% CVF from Miller et al. (2013).

Because of the invasive nature of this technique and the potential for complications and sampling errors, which limit diagnostic accuracy and reproducibility, other diagnostic methods are being investigated. Development of a technique which can noninvasively quantify the diffusive myocardial fibrosis is highly critical and desirable to stratify disease and evaluate newer therapies for the treatment of heart failure.

3.3 Evolution of ECV by CMR

Initial validation in humans utilizing CMR to quantify ECV (ECV_{CMR}) and in turn diffuse myocardial fibrosis was performed by Flett et al. (2010). They employed a technique they termed "equilibrium contrast CMR", which involved an initial bolus of GBCA, followed by a continuous infusion to achieve an equilibrium of contrast between the blood pool and the myocardium. They estimated the blood volume of

distribution from 1-Haematocrit (Hct) and then used CMR to measure the pre- and post-contrast equilibrium T_1. Using the formula 3.1, they then calculated the ECV (for more details see Appendix A).

$$ECV_{CMR} = (1 - Hct) \cdot \frac{\Delta(\frac{1}{T1_{myo}})}{\Delta(\frac{1}{T1_{blood}})} = (1 - Hct) \cdot \frac{\Delta R_{myo}}{\Delta R_{blood}} \tag{3.1}$$

They validated this technique by direct comparison with histological fibrosis quantification using Picrosirius red staining on surgical biopsy samples from patients undergoing aortic valve replacement for Aortic Stenosis (AS, n=18) and myomectomy for Hypertrophic CardioMyopathy (HCM, n=8) and showed excellent correlation (combined R^2 =0.80). Similar studies correlating ECV_{CMR} with histolr Ischaemic Heart Disease (IHD) awaiting cardiac transplantation, heart failure and myocarditis. A significant barrier to the adoption of the ECV_{CMR} technique was the use of the primed infusion protocol. This involved the patient being removed from the scanner after conventional LGE imaging and being given anothogy have been reproduced in patients with aortic and mitral regurgitation, Dilated CardioMyopathy (DCM) oer bolus of GBCA, followed by a 15 min pause and then an infusion. The patient would then be returned to the scanner any time between 45 and 80 min after the bolus for repeat T1 measurement. A bolus-only approach was proposed by Schelbert et al. (2011), who demonstrated in 10 volunteers that myocardial ECV_{CMR} could be reliably measured 15–20 min after a single bolus of GBCA. Further work by White et al., this time in 147 subjects, demonstrated a strong correlation between 15-min bolus only and infusion ECV_{CMR} measurement (R^2 =0.97). They did note that when the ECV was >40%, the bolus only technique consistently measured a higher ECV than the infusion.

Finally, the validation of ECV_{CMR} as part of a split-dose protocol (e.g. as part of stress perfusion) by McDiarmid et al. (2015). further increased the potential clinical utility of the technique; however, there are suggestions that ECV_{CMR} values may differ depending on the dose of GBCA used. Most recently, a synthetic ECV can be automatically generated during scanning, in which the haematocrit of blood is inferred from the T_1 of the blood pool (as the relationship between haematocrit and R_1=$1/T1_{Blood}$ is linear), removing the need for a blood test. It has also been replicated at 1.5 and 3T on other scanner platforms. The key advantage of this technique is the simplification of the ECV workflow, by removing the need for blood tests to measure haematocrit, which is burdensome in busy departments, is a source of user error and introduces reporting delay. Implementation of inline synthetic ECV tools (with instantaneous ECV maps) would reduce the barriers to clinical use of ECV and potentially increase quality of care as review is immediately available.

3.4 ECV by CMR in Clinical Practice

Normal ECV values depend on the field strength, T_1 mapping sequence and scanner manufacturer, but range between 20 and 26%, and appear to be slightly higher in women compared to men. With the exception of cardiac Amyloidosis and Oedema, increases in myocardial ECV are generally due to an increased Collagen

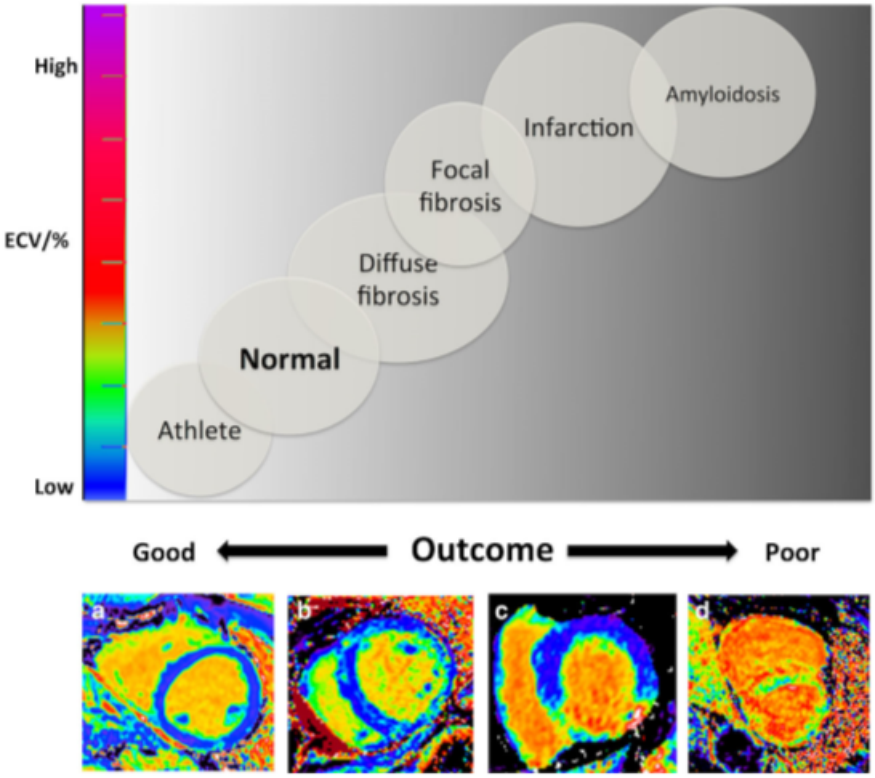

Figure 3.3. Extracellular volume fraction (ECV) variability and outcome at 1.5T by myocardial pathologies. Top panel depicts ECV and associated outcome across health and disease with increasing ECV on the y-axis and outcome on the x-axis. Bottom panel shows four exemplar ECV maps of a healthy volunteer with normal ECV of 24% (a), a patient with aortic stenosis with mild ECV elevation at 30% (b), a patient with an inferior myocardial infarct (c), and a patient with AL cardiac amyloidosis with an ECV of 50% and the poorest outcome (d). Adapted from Scully et al. (2018).

Volume Fraction (CVF), making it a marker of fibrosis. For example, acute Myocardial Infarction (MI) results in some of the highest ECV values (58.5±7.6%) and chronic MI is not far behind (51±8%). Diffuse fibrosis, however, rarely increases beyond 40%. Cardiac Amyloidosis, which is characterized by the extracellular deposition of misfolded protein, produces large increases in ECV (greater than any other non-ischemic cardiomyopathy) in the region of 46.6±7%. ECV is also mildly elevated in both Hypertrophic Cardiomyopathy (29.1±0.5%) and Dilated Cardiomyopathy (28± 0.4%). On the other hand, Anderson Fabry disease appears to have a similar ECV to healthy volunteers (25±2.3%), at least in the early stages of the disease (see figure 3.3).

3.5 Evolution of ECV by CT

ECV imaging by cardiac CT (ECV_{CT}) lags behind the CMR field, but is potentially an attractive alternative. ECV_{CT} relies upon the same principle as ECV_{CMR} and is calculated using the formula 3.2 (for more details see appendix A).

$$ECV_{CT} = (1 - Hct) \cdot \frac{\Delta(\frac{1}{HU_{myo}})}{\Delta(\frac{1}{HU_{blood}})} \tag{3.2}$$

where ΔHU is the change in Hounsfield unit attenuation pre-contrast and post-contrast (i.e. HU post-contrast HU pre-contrast). Early data was presented in abstract form by Ugander et al. (2011), which showed, in dogs that underwent coronary occlusion and reperfusion (n=10),that ECV_{CT} and ECV_{CMR} correlated well (R^2=0.80, p<0.001), with a small mean difference between ECV_{CMR} and ECV_{CT} (3±9%).

Myocardial ECV_{CT} was first validated in humans by Nacif et al. (2012). They compared ECV_{CMR} and ECV_{CT} in 24 subjects (both healthy volunteers and those with heart failure) and found good correlation between the two (r=0.82, p<0.001). Post-contrast images were taken after a 10 min delay, copying the exact parameters of the initial precontrast calcium score scan. Overall radiation dose was low (<2 mSv). The average duration of ECV_{CT} in this study was 13±1.5 min, compared to 47±5 min for ECV_{CMR}. ECV_{CMR} results were slightly lower (28.6±4.4%) compared to ECV_{CT} (31.6±5.1%). The same group went on to compare ECV_{CT} in healthy volunteers and those with either systolic or diastolic heart failure. They used a similar protocol, only this time, taking the post-contrast images after a shorter 7-min delay. They found that the ECV was significantly higher in participants with systolic heart failure (41±6%) compared to healthy subjects (33±2%) and those with diastolic heart failure (35±5%).

Bandula et al. (2013) in the same year validated ECV_{CT} against the gold standard invasive endomyocardial biopsy, as well as ECV_{CMR} in 23 patients with severe aortic stenosis. This time, they used an initial bolus of contrast agent, followed by a slow infusion to achieve equilibrium. They found that ECV_{CT} showed significant correlation with both histological measures of fibrosis (r=0.71, p<0.001) and ECV_{CMR} (r=0.73).We subsequently compared 5-and 15-minute time points post-contrast bolus for equilibrium CCT in 53 patients (26 with systemic amyloidosis and 27 with aortic stenosis). We demonstrated that ECV_{CT} at 5-minute post-contrast showed a stronger correlation with ECV_{CMR} than at15-minute post-contrast (r^2 =0.85 compared to 0.74). We think this is because, although earlier imaging risks non-equilibration, iodine is a weaker contrast agent than GBCAs, so the higher signal-to-noise ratio of earlier imaging outweighs this. ECV_{CT} was consistently higher in those patients with confirmed cardiac amyloid compared to those with aortic stenosis (54±11% compared to 28±4%, p<0.001) and was able to discriminate between patients with definite cardiac amyloid and those with aortic stenosis in all cases. Work is also being done using dual-energy CT to quantify myocardial ECV, which is an attractive concept, as it would potentially avoid mis-registration errors associated with the separate pre- and post-contrast scans, by obviating the need for the pre-contrast scan.

Hong et al. (2016) used dual-energy CT to estimate myocardial ECV Indoxorubicin-induced dilated Cardiomyopathy in rabbits. They showed equivalent ECV results by dual-energy CT from 3 up to 20 minute post contrast administration. ECV values were significantly higher at 6,12 and 16 weeks after starting twice weekly doxorubicin injections than at baseline (35.3, 41.9, 42.1% vs. 28.5%). ECV measured

by dual-energy CT showed excellent correlation with ECV_{CMR} (r=0.888, p<0.001) and with collagen volume fraction on histology (r=0.92, p<0.001). Work has also been done in humans using dual energy CT involving 30 subjects (7 healthy, 23 with hypertrophic or dilated cardiomyopathy, amyloidosis or sarcoidosis). The post-contrast dual-energy CT scan was performed at 12 minute and results for ECV were compared with ECV_{CMR} and showed good agreement. Those participants with disease had significantly higher myocardial ECV by dual-energy CT compared to healthy subjects (p<0.010). More recently, synthetic ECV has also been successfully implemented in CT, where the haematocrit of blood is inferred from the attenuation of the blood pool (as the relationship between haematocrit and HU is also linear), simplifying the ECV workflow and allowing instantaneous display of ECV maps (Treibel et al., 2017; Fent et al., 2017).

3.6 CT versus CMR for myocardial ECV quantification

While the evidence base for ECV_{CMR} may be larger and experience greater, the use of CT in this regard does have some distinct advantages.

- Likely to prove the biggest advantage is that ECV_{CT} measures the direct effect of iodine-based contrast agents on the measured signal (through the effect of iodine on x-ray absorption), whereas ECV_{CMR} relies on measuring the effect of GBCAs on protons (therefore making two assumptions—the first is that the relaxivity of tissues compared to blood is the same and the second is that water is rapidly exchanged between intra- and extracellular compartments).

- Another common contraindications to CMR such as claustrophobia and pacemaker implantation do not apply for CT.

- ECV_{CMR} is likely to be costly, both financially and in terms of patient throughput, with scans taking up to 60 min, whereas CT scans are significantly faster and more widely available.

- CT also offers higher spatial resolution particularly in plane and allows isotropic reconstruction.

Of course, these potential advantages should be weighed up against the risks of ionizing radiation from CT, especially in younger patients. Furthermore, CT is also prone to artefacts, (beam hardening and streak artefacts) that may hamper the evaluation of myocardial ECV. Finally, in delayed acquisitions, iodine contrast media provide less signal compared to GBCAs and differentiation between myocardium and left ventricular cavity is hampered, particularly when the myocardium is thinned (for example in Dilated Cardiomyopathy). GBCAs have been associated with the development of nephrogenic systemic fibrosis, seen with linear chelates rather than macrocyclic and in patients with significantly impaired renal function (eGFR<30 mL/min/1.73 m^2). These linear agents have also been associated with brain deposition. Iodinated contrast agents have in turn been associated with contrast-induced nephropathy and preexisting Chronic Kidney Disease (eGFR<60 mL/min/1.73 m^2) is the most important risk factor for this. It is important to bear in mind while

considering the pros and cons of both of these modalities that relative to the current gold standard for diagnosing diffuse fibrosis of invasive endomyocardial biopsy, both offer very attractive alternatives.

3.7 ECV Quantification beyond the Myocardium

The potential for ECV_{CT} and ECV_{CMR} extends beyond the myocardium. Wang et al., 2019 used CT to estimate liver ECV in order to measure hepatic fibrosis and validated this against histological hepatic fibrosis staging in 141 participants ($r=0.493$, $p<0.001$). Bandula et al. (2017) also demonstrated elevated ECV_{CMR} in the liver, spleen and skeletal muscle in patients with systemic amyloidosis, which tracked semiquantitative amyloid burden in the liver and spleen by serum amyloid P component (SAP) scintigraphy. Similar work has been performed by Yeung et al. (2017) using ECV_{CT}. They showed that in patients with hepatic and splenic amyloid, there was a significantly higher ECV compared to patients without liver and spleen involvement ($p<0.001$). They were also able to show that increases in ECV_{CT} positively correlated with the grade of hepatic and splenic uptake on SAP scintigraphy ($r=0.758$ for liver, $r=0.867$ for spleen).

3.8 Future Outlook

Currently, a poorer signal-to-noise ratio than CMR and the use of ionizing radiation have impeded wider application of myocardial tissue characterization by CT. Nevertheless, the possibility of providing an assessment of coronary anatomy, coronary flow and myocardial tissue characterization in a single modality is an attractive concept, with huge implications for imaging workflow. Beyond the optimization of dual-energy CT with minimization of image artefacts, radiation dose and iodinated contrast dose (e.g. using low-energy monochromatic imaging), more advanced technologies are on the horizon. Spectral CT imaging exploits the different K-edge behaviour of different tissues (calcium, blood, fat and myocardium). This technology goes beyond the two-photon energy levels used in dual-energy CT, and utilizes energy-sensitive photon counting detectors to obtain greater tissue information by differentiating photons at different energy levels. Early preclinical data suggests that spectral CT may improve image quality over conventional CT by eliminating beam hardening.

The other hand, T_1 mapping field has been rapidly advancing to the point of widespread clinical utility. Since the first T1 quantification with the original modified look-locker imaging (MOLLI) in 2004, new MOLLI variants, ShMOLLI (a shortened variation with long T_1 advantages), saturation recovery variants such as SASHA (offering complete heart rate insensitivity) or hybrid approaches have been developed, and incremental developments such as respiratory motion correction have gradually increased accuracy and precision. ECV maps are now routine in some centers, but ECV development and standardization are still on-going and will require global approaches. On the horizon, MR fingerprinting may offer more rapid multi-parametric tissue characterization in the future by providing myocardial T_1, T_2, and Proton Spin Density in a single breath-hold (Scully et al., 2018).

Part II

Experimental studies

Chapter 4

T1 and extracellular volume fraction mapping in cardiac magnetic resonance: estimation of accuracy and precision of a novel algorithm

In this chapter we present the ECV quantification and comparing it with those from well-consolidated methods. Late Gadolinium Enhanced (LGE) Cardiac Magnetic Resonance (CMR) is a diagnostic reference for focal myocardial fibrosis, whose importance grew further after the development and optimisation of the Inversion-Recovery (IR) sequence (Constantine et al., 2004; Kim et al., 1996; Flacke et al., 2001). T_1 mapping can also detect diffuse myocardial disease (Taylor et al., 2016; Puntmann et al., 2016; Iles et al., 2008), but the T_1 of the normal myocardium cannot be measured directly in diseased patients. Data for various tissues were reported recently in literature (Dabir et al., 2014), in most cases interpolating signal data by the Levenberg Marquardt (LM) algorithms (Marquardt, 1963). However, the Extracellular Volume Fraction (ECV, defined as the fraction of myocardial tissue not occupied by cells) has proven to be a more accurate and reproducible biomarker for myocardial disease (Kammerlander et al., 2016; Treibel et al., 2014), and can be determined calculating the myocardium/blood partition coefficient by mapping T_1 before and after the Gadolinium administration. The uncertainty and accuracy of T_1 values affects the ECV estimation. The level of precision (i.e., space and time reproducibility) and accuracy of T_1 measurement, are generally influenced by many components, such as technical factors (e.g. sequence-related, partial volume effects), physiological factors (e.g., breath-holds, cardiac motion, flowing blood, and haematocrit), procedural errors (e.g., sequence-related parameters, repeatability of the scanner acquisition, and data fitting), and assumptions related to the contrast-agent (Cameron et al., 2018). A new, time-sparing, procedure to obtain the ECV map was recently described (Altabella et al., 2017), in which a Nonlinear Least Squares (NLS) problem is solved to fit a five-parameter model to a dataset. In this method, the computational complexity of the problem was reduced to a search over one dimension.

The algorithm concurrently restored polarity if only signal magnitudes are available. In the present work, the reliability of this method is further explored, investigating precision (space and time reproducibility) and accuracy of T_1, calculating the propagated error for ECV and comparing the error range with the inter-patient variability. Firstly, the results obtained with the new methodology are compared with those from well-consolidated methods (previously published (Messroghli et al., 2010), and suggested by the scanner manufacturer). Secondly, the error contributions to T_1 values due to the fitting procedure and measurement repeatability are estimated (with phantom scans). Finally, the ECV values are calculated for a large cohort of patients (40 patients with known or suspected heart disorder and 20 healthy controls), comparing the error range with the inter-patient variability.

4.1 Numerical and experimental phantom

Eight flasks (3 cm of diameter and 4 cm high), containing 2% of agarose gel (Sigma-Aldrich©) and 0.5% of NaCl (to mimic the tissue electrical conductivity), were prepared varying the concentration of CuSO4 (Sigma-Aldrich©) between 0.25 mM and 2 mM, obtaining T_2 around 50 ms (i.e. the normal myocardium value) and T_1 values in the range 250-1000 ms. A ninth flask was a vial filled with 0.5% agarose gel and 0.025 mM of $CuSO_4$, to mimic blood T_1 and T_2 (about 1500 ms and 200 ms, respectively) (Salerno et al., 2013). The flasks were tied among them, and imaged with a 1.5 T MR tomograph (Magnetom Avanto, Siemens Healthcare, at Erlangen Germany). The reference T_1 values of the flasks were measured with an IR (gold-standard) sequence using 25 inversion times (TIs) in the range 100-2500 ms and interpolating signal data with the LM algorithm, (also, T_2 values were measured with a standard spin-echo pulse sequence using 10 echo times, but data are not shown)(figure 4.1, left panel).

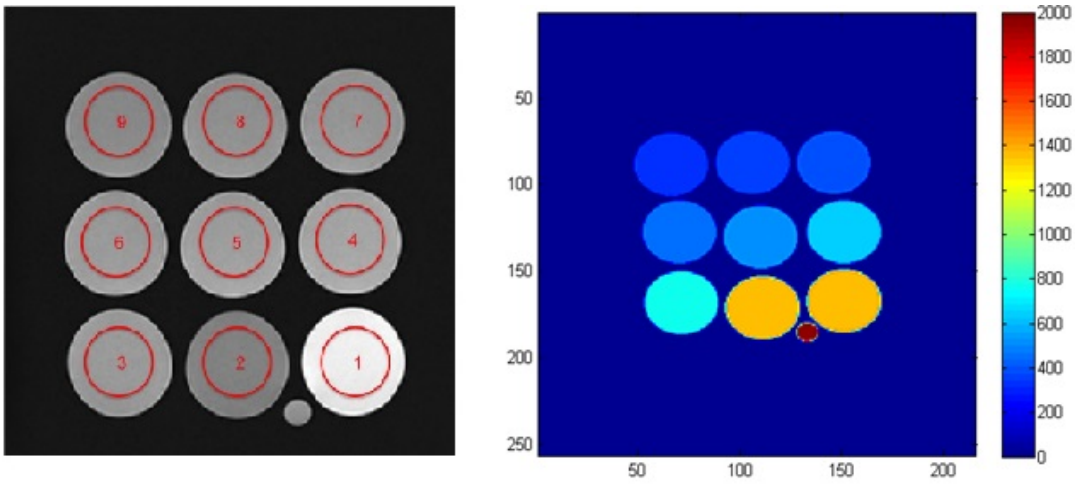

Figure 4.1. Left panel, real phantom to mimic the tissue electrical conductivity. Right panel, numerical phantom generated with MATLAB (reference T_1 values are in ms and represented with a colorbar).

The T_1 for each test object was determined from the T_1 map as mean value in a ROI, covering about 80% of the cross-sectional area of the selected flask. A numerical phantom was generated with MATLAB (R2009b, version 7.9.0.529), oversampling the acquisition matrix (from a pixel size of 1.41×1.41 mm^2 to 0.71×0.71 mm^2) and assigning to each flask the corresponding reference T_1 value (figure 4.1, right panel). The phantom was scanned also with MOLLI (Modified Look-Locker Inversion-recovery) sequences for cardiac imaging, provided by the scanner manufacturer, comparing so measured T1 values with the reference values. A pre-contrast sequence scheme of 5(3)3 (i.e., five images are acquired starting from the first TI, and after a three-cardiac cycle pause, three additional images are acquired starting from the sixth TI), or 4(1)3(1)2 for the post-contrast sequence, was chosen to decrease the scanning time with comparable accuracy and precision (Altabella et al., 2017). Other sequence parameters were: matrix size=218x256, voxel size=1.41x1.41 mm^3, TR/TE=2.8/1.12 ms, and Flip Angle=35°. TI values pre-defined by the scanner manufacturer were used. Image analysis and data interpolation for the MOLLI sequences are reported in the following.

4.2 Image analysis and fitting procedures for MOLLI sequences

Firstly, median filtering and thresholding with a variable cut-off were used to remove salt-and-pepper and random noise of the images. Data interpolations were performed by the Fast Nonlinear Least Squares (FNLS) algorithm implemented in Altabella et al. (2017), obtaining pixel-wise mapping of T_1. The following fitting model (including also T_1* correction) was used:

$$\begin{aligned} S(i,j,TI) &= A(i,j) + B(i,j) \cdot e^{-TI/T_1^*(i,j)}, \\ T_1(i,j) &= T_1^*(i,j) \cdot \frac{T_1^*(i,j) \cdot B(i,j)}{A(i,j)} - T_1^*(i,j) \end{aligned} \tag{4.1}$$

where A represent the scaling factor for signal intensity, B reflect the quality of the inversion, and T_1* is the apparent T_1.The aim is to find the best fitting T_1(i, j) in the least squares sense (i.e. in terms of sum of squares) (Messroghli et al., 2010). Equation 1 was solved using a reduced dimension approach, separating the unknown variables in S (i, j, TI), as also proposed previously by Barral et al. (2010). Using this approach, T_1 can be found through one-dimensional search, without need of initial parameter estimation as a global search in the selected range of values is performed (Messroghli et al., 2010). The results of FNLS were compared with those obtained from the method of Messroghli et al. (2010) and from the scanner manufacturer. Both of them use the LM algorithm, with a difference in the stop conditions for the iterations. Hereinafter, the three methods will be referred to as FNLS, MM and MS respectively. The accuracy associated to mean T_1 measured by MOLLI (with the same ROI used for IR acquisition, see phantom section) is defined as follows:

$$T_1 Accuracy(\%) = \frac{T_{1,MOLLI} - T_{1,IR}}{T_{1,IR}} \cdot 100. \tag{4.2}$$

Spatial reproducibility was estimated as the Standard Deviation (SD) in the ROI. Time reproducibility (test-retest reproducibility) was assessed repeating the MOLLI acquisition once a day, for 9 days, calculating the associated SD for the mean T_1. The T_1 uncertainty was estimated assuming that the total uncertainty consists in the composition of two independent random errors normally distributed, so combining the time-dependent and spatial-dependent term into a quadratic sum. The Gamma-tool analysis, commonly used in radiotherapy to study the pixel-wise agreement between measured and reference spatial distribution of absorbed dose Low et al. (1998); Low and Dempsey (2003), was here implemented (in MATLAB) to perform paired comparisons between reference (IR) and tested (MOLLI) T_1 maps. The reference T1 map was obtained by down-sampling the numerical phantom aforementioned to the experimental acquisition matrix (i.e., matrix size 218x256 and pixel size 1.41x1.41 mm^2). The tolerance criteria in terms of Distance to Agreement (DTA) and pixel-by-pixel Difference (D) were set. The DTA tolerance was selected as 3 pixels (4.23 mm), as the general rule states that the sampling pitch (i.e. the pixel size) should be less than or equal to one third of the DTA tolerance (Low et al., 1998). The D tolerance was varied in the range 2-5%. Gamma (γ) values higher than 1 indicate failure to comply with the tolerances adopted.

4.2.1 Patient population and data acquisitions

40 patients with known/suspected heart disorder (5 dilated cardiomyopathy, 5 pulmonary hypertension, 5 hypertrophic cardiomyopathy, 5 non-compacted cardiomyopathy, 15 myocarditis, and 5 cases with other cardiac conditions) and 20 healthy controls were examined. The local ethics committee approved the study, and all subjects provided written informed consent. Apical, basal and mid-ventricular slice were acquired for each subject, pre- and post-injection (15 min later) of a Gd-BOPTA bolus (gadobenate dimeglumine, 0.1 mmol/kg) (Borrazzo et al., 2019), using the pre- and post-contrast MOLLI sequences described above ("Numerical and experimental phantom"). Signal images referred to various TI were systematically motion-corrected and co-registrated, using software provided by the manufacturer (Xue et al., 2012).

4.2.2 ECV calculation

The ECV maps were calculated from the pre- and post-contrast T_1 map, applying the following expression:

$$ECV(\%) = (1 - Hct) \cdot \frac{\Delta R_{1,myo}}{\Delta R_{1,blood}} \cdot 100, \tag{4.3}$$

where $\Delta R_{1,myo} = (1/T_{1,postmyo} - 1/T_{1,premyo})$ and $\Delta R_{1,blood} = (1/T_{1,postblood} - 1/T_{1,preblood})$ are the longitudinal relaxation rate (R_1) enhancement for myocardium and blood pool, respectively, and Hct is the patient hematocrit (i.e., the ratio between red blood cell volume and total blood volume, for more details see appendix A). The ECV maps were calculated by the FNLS method (the MM and MS methods do not calculate directly ECV, but just T_1 maps), performing also preliminary

affine co-registration of pre-contrast and post-contrast T_1 map (Altabella et al., 2017). Patient myocardial ECV was also used to compare several methods. Patient myocardial ECV was obtained as an average in a ROI delineating the myocardium region, drawn on the pre-contrast T1 map excluding pixels with values higher than 1250 ms, and overimposed on the ECV map (see Borrazzo et al. (2019) for a more detailed description).

4.3 Results

4.3.1 Phantom studies

Differences (in paired comparisons) of mean T_1 datasets were not significant neither for Student's t-test, nor for Kruskal-Wallis test (always p-value>0.200). Analogously, paired comparison for mean T_1 with Bland-Altman plots did not evidence trend differences (figure 4.2 reports an example of Bland-Altman plots for the 4(1)3(1)2 MOLLI sequence).

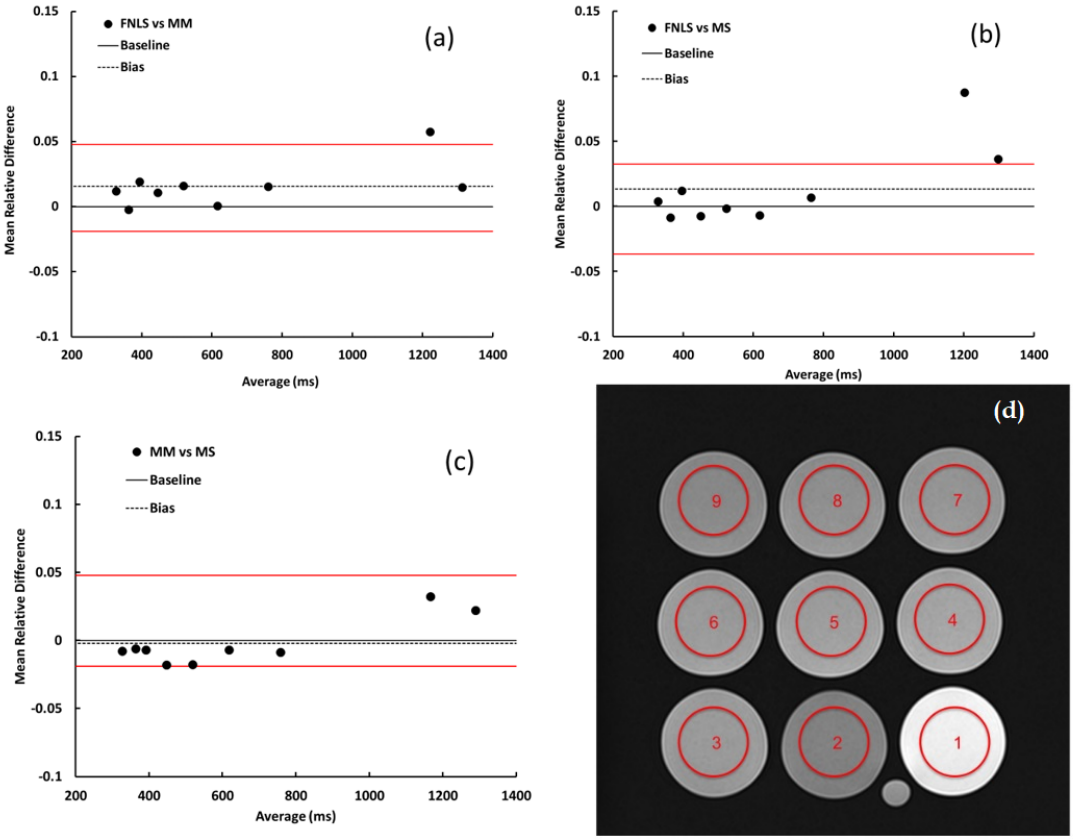

Figure 4.2. Bland-Altman plots showing paired comparisons for the MOLLI sequence 4(1)3(1): FNLS vs MM (a), FNLS vs MS (b), MM vs MS (c) and (d) real phantom. The 95% confidence interval (red lines) and bias (dotted lines) are also displayed.

The T_1 accuracy (equation 4.2) for each method is reported in Figure 4.3 for the 4(1)3(1)2 and 5(3)3 MOLLI sequence.

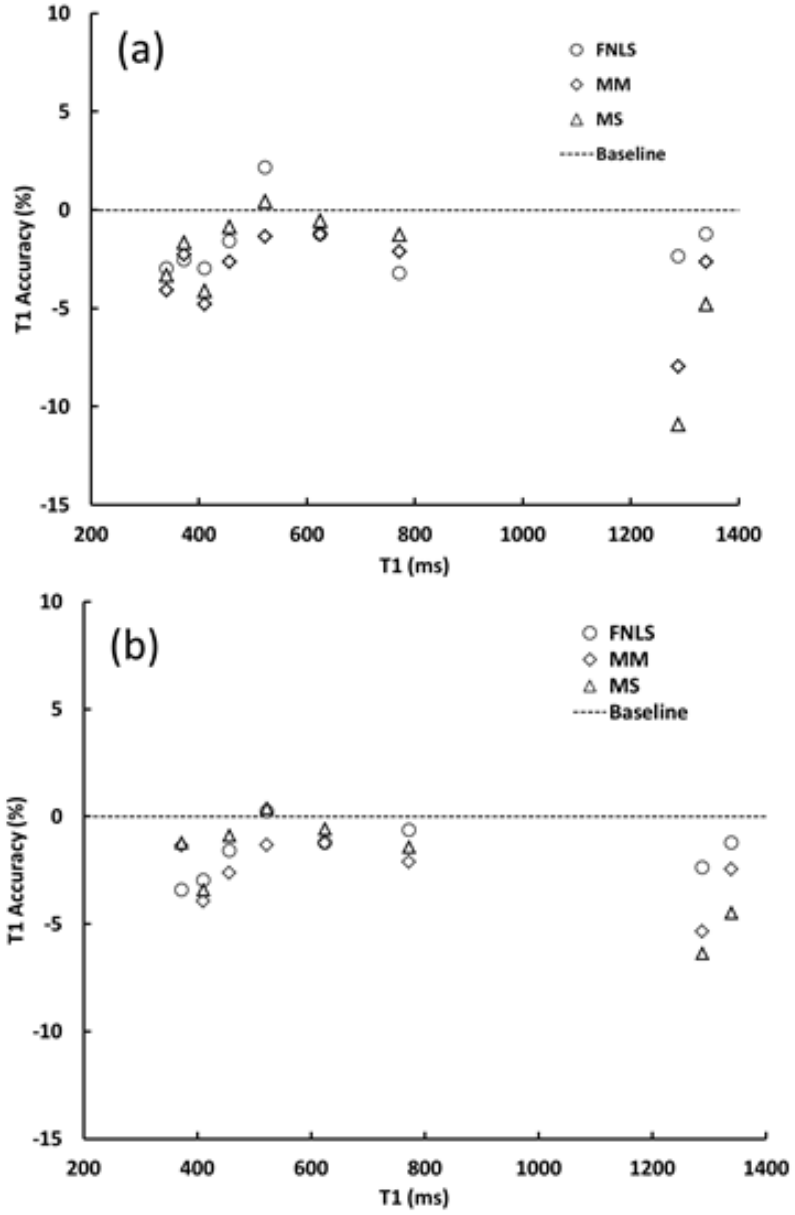

Figure 4.3. Accuracy of T1 measured by MOLLI sequences for all methods (FNLS, MM and MS) with respect to T1 values obtained by the IR spin-echo sequence: (a) 4(1)3(1)2 sequence, (b) 5(3)3 sequence.

The differences were between -12% and -1% across methods, with average differences for the 4(1)3(1)2 sequence of -3.2% for MM, -1.7% for FNLS and -2.9% for MS, and for the 5(3)3 sequence of -2.2% for MM, -1.6% for FNLS and -2.5% for MS. The FNLS showed the best computational efficiency, calculating T_1 maps in 18

s with a standard desktop PC, whereas the computational time was 822 s and 471 s for the MM and MS method, respectively. The Gamma analysis of the T_1 maps was performed for all the tested methods varying D from 2% to 5%. An example of this analysis in terms of mean γ value (γm) and Pass Rate (PR, i.e. the percentage of pixels with γ<1), is reported in Table 4.1 for the 4(1)3(1)2 sequence (data for the 5(3)3 sequence were almost the same).

Table 4.1. Results of the Gamma analysis for different methods, using the numerical phantom as reference T_1 distribution and the T_1 maps measured by the 4(1)3(1)2 sequence. The reported γm (mean γ value) and the PR (Pass Rate) were calculated for the three methods varying D from 2% to 5%.

Methods	D=2% γ_m PR(%)	D=3% γ_m PR(%)	D=5% γ_m PR(%)
FNLS	1.15 (63.9%)	1.03 (67.9%)	0.98 (70.3%)
MM	1.27(56.7%)	1.11 (64.4%)	1.07 (68.6%)
MS	1.70 56.5%	1.32 (60.7%)	1.14 (64.9%)

Figure 4.4(a-c) reports an example of Gamma distributions for the T_1 map from the same sequence, obtained with D=3%, and referred to FNLS (a) MM (b) and MS (c).

The uncertainty on the T_1 measured by MOLLI was estimated. For the FNLS method, the SD in the ROI on each test object (representing the spatial reproducibility of the T_1 value) was at most about 2.4%, similarly to the other methods (up to 2.5%). Table 4.2 summarizes the mean T_1 (averaged over repeated measurements) and percent SD for the three methods, obtained by the phantom studies with the 4(1)3(1)2 sequence, repeating the acquisition once a day for 9 days.

Table 4.2. Mean T_1 (averaged over repeated acquisitions) and corresponding SD, repeating the acquisition with the 4(1)3(1)2 sequence, once a day, for 9 days.

Phantoms	IR T_1 reference	FNLS Mean (T_1) (± SD)	MM Mean (T_1) (± SD)	MS Mean (T_1) (± SD)
9	1339	1322.0 ± 2.0	1303.8 ± 3.21	1275.1 ± 2.14
8	1288	1257.6 ± 7.4	1185.9 ± 4.67	1147.0 ± 5.94
7	771.6	746.9 ± 2.25	755.3 ± 3.74	761.9 ± 1.94
6	624	616.4 ± 1.85	616.3 ± 3.22	620.7 ± 1.7
5	522	533.3 ± 1.63	515.1 ± 2.87	523.3 ± 1.59
4	455.8	448.6 ± 1.43	443.9 ± 2.59	451.9 ± 2.04
3	410.3	398.2 ± 1.44	390.7 ± 2.72	393.5 ± 6.75
2	371.5	362.1 ± 1.56	363.1 ± 3.54	365.4 ± 2.90
1	339.6	329.5 ± 0.80	325.7 ± 2.74	328.3 ± 2.05

The maximal SD of the time reproducibility (considering also data from the 5(3)3 sequence, not shown) was about 7.4% (see Table 4.2). The quadratic sum of the time/spatial-dependent errors yields an uncertainty of about 8%, according to the literature Kellman et al. (2012). The final uncertainty for the two other methods was similar, so an overall uncertainty of 10% was conservatively adopted for the T_1.

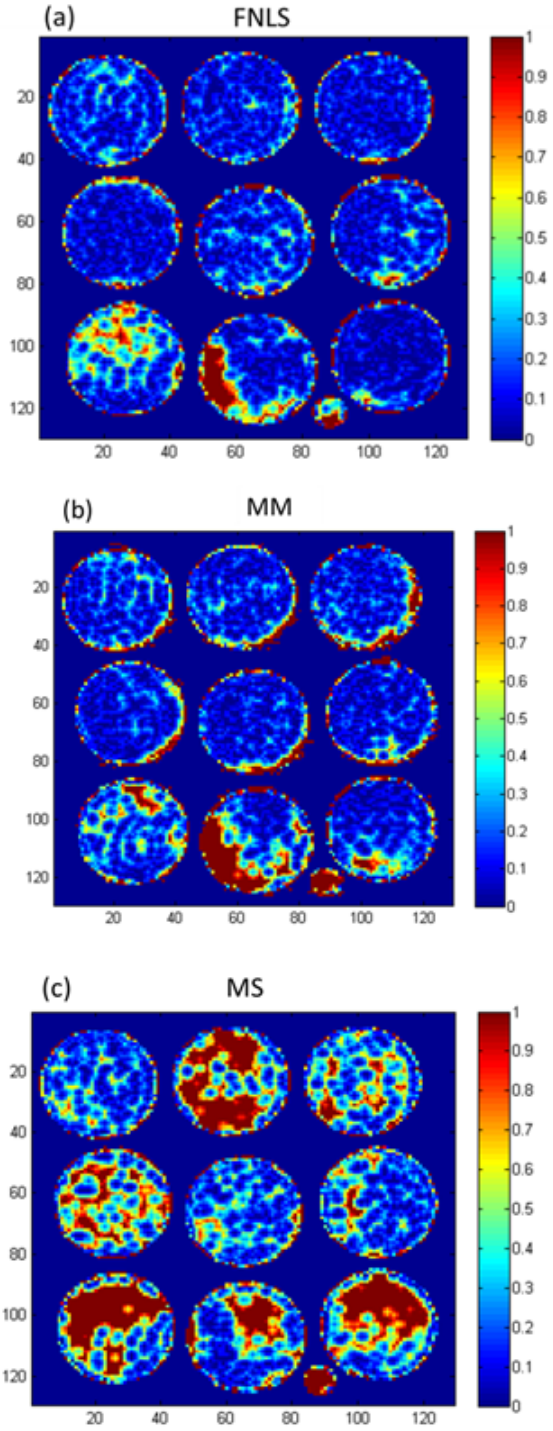

Figure 4.4. Gamma distributions obtained by the comparison between experimental and numerical (reference) T_1 maps: (a) FNLS (b) MM and (c) MS. Tolerance criteria were D=3%, and DTA=4.21 mm. The Gamma values are represented with a colorbar.

4.3.2 Patient studies

The mean heart-rate value during the acquisitions was 62±10 bpm. ECVs of healthy and diseased patients are represented in boxplots (Figure 4.5 a-c).

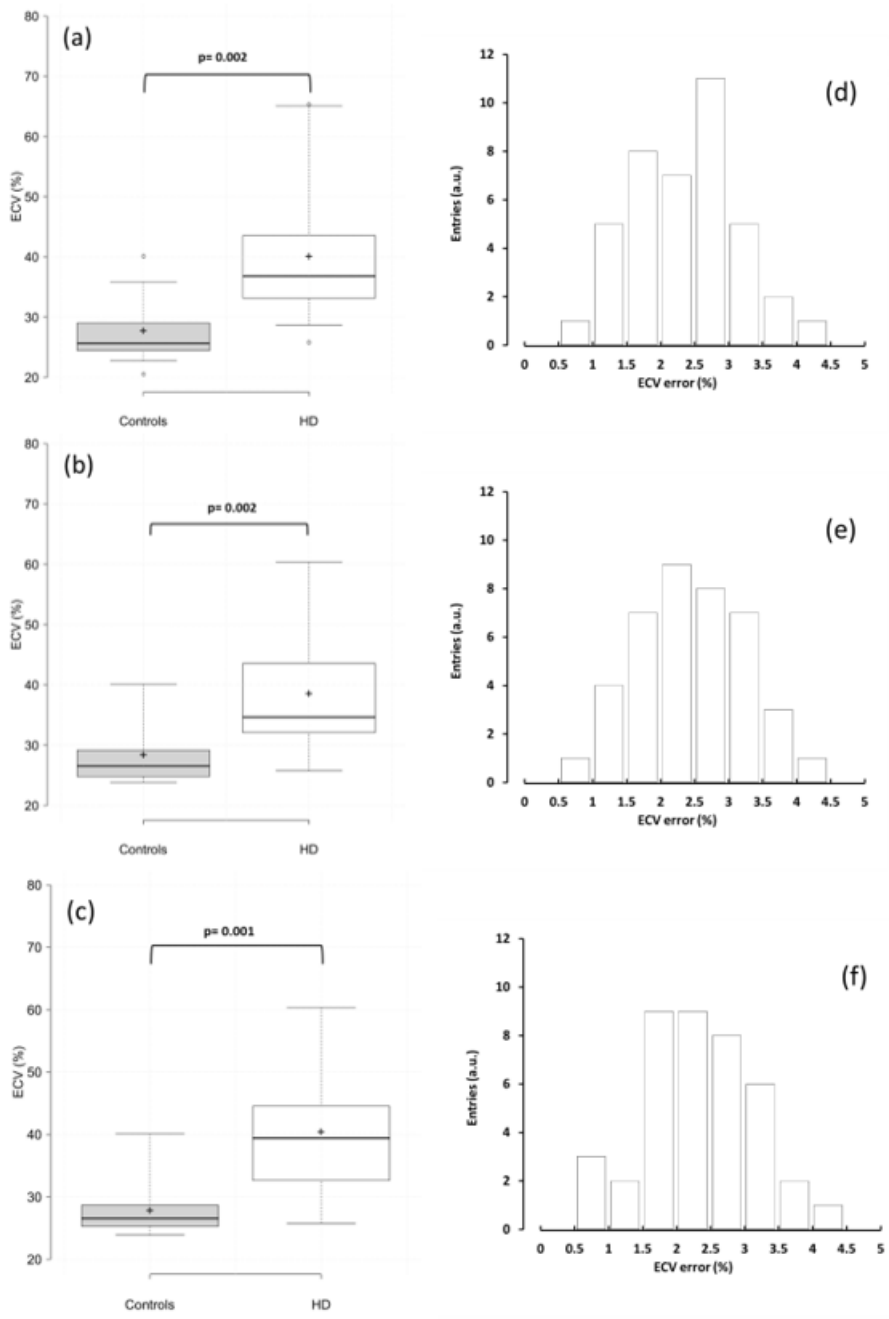

Figure 4.5. Left panels: boxplot comparing ECV (%) in controls and diseased (heart disorder, HD) patients for (a) FNLS, (b) MM and (c) MS (p-value of the Kruskal-Wallis test is also reported). Right panel: histograms of the error distribution of the ECV for (d) FNLS, (e) MM and (f) MS.

The ECV values of the healthy controls ranged for FNLS from 23.4% to 29.8% (median value: 25.8%), whereas for MM from 24.1% to 30.1% (median value: 26.9%) and for MS from 23.9% to 30.6% (median value: 26.2%). For diseased patients, the FNLS yielded ECV values ranging from 31.0% to 53.9% (median value: 33.7%), MM values ranged from 28.7% to 45.9% (median value: 36.8%) and MS values ranged from 31.5% to 54.9% (median value: 39.4%). The two groups of values significantly differ from each other for all methods. The ECV error was calculated by error propagation for each patient, considering an overall T_1 uncertainty of 10% (aforementioned). ECV error distributions are reported in figure 4.5 d-f. The mean error on ECV was 2.5% for FNLS, 2.2% for MM and 2.2% for MS.

4.4 Discussion and Conclusion

Statistical tests and Bland-Altman analysis did not show significant differences among mean T_1 datasets from various methods. Also, the estimated uncertainty due to space and time reproducibility for T_1 was similar among the methods. The results of the Gamma analysis confirm the similarity of the findings (see table 4.1 for a result example). No patterns of disagreement result from a visual analysis of γ maps (figure 4.4 reports sample data), except for high gradient regions where out-of-tolerance (>1) values at the edges of each flask are systematically present. This is probably due to partial volume effects at the flask edges, reducing the SNR (signal is not present outside the flasks), so noise-related dispersion or bias of the data are more probable.

On the other hand, out-of-tolerance values are almost systematic in the vial (where the highest T_1 value is present) mainly for MM and MS, and this is also noticeable in plots of T_1 accuracy (figure 4.3), indicating a better performance for FNLS. Also, the results of the Gamma analysis seems to show slightly better results for FNLS than other methods, as evidenced by lower γm and higher PR reported in table 4.1. A trend T_1 underestimation for all methods is also noticeable from figure 4.3. This is probably due to linear phase-encode ordering, mostly used for T_1 mapping, so the amplitude of the phase-encoding gradient increments in steps. This avoids signal perturbations related to eddy-currents, but on the other hand, it causes a progressive signal saturation related to T_2 when approaching the k-space centre (Cameron et al., 2018). The proposed method reduces the range of search of T_1 values, avoid the input of initial parameter, and yield solutions that intrinsically have physical meaning. Consequently, the resulting T_1 maps should be less sensitive to the starting seed, and this seems confirmed by the mean accuracy slightly better for the FNLS method (figure 4.3). A further benefit of this approach is undoubtedly true: the computational time is at least 25-fold decreased compared to other (LM-based) methods, making possible also real-time ECV estimation, as well as paves the way to Big Data-related applications (Andreu-Perez et al., 2015).

The distribution of the ECV errors (figure 4.5) shows a maximum of 4.25%, yielding an experimental uncertainty (with k=2) of 8.5%, well below the ECV interpatient variability observed for the healthy subjects (36.0% at 2SD), confirming the reliability of diagnosis based on ECV. Myocardial ECV estimations for normal subject were in a good agreement with previous studies that reported values between

25-26% (Kellman et al., 2012; Dabir et al., 2014). For the diseased subjects examined here the ECV values were in the range 32-54.3% (median 33.7%), also in this case in a good agreement with the values reported by previous studies (32%-69%) (Kellman et al., 2012). The results obtained with FNLS were indistinguishable from those derived by other well-consolidated methods. However, the new methodology appeared slightly more accurate and more robust, providing solutions having always a physical meaning. The computational efficiency improves by a factor of at least 25, making this method more suitable for Big Data related applications.

Chapter 5

Accuracy and clinical relevance of extracellular volume fraction in MR and CT examinations

In the last 10 years, the use of Contrast Agents (CAs) to measure diffuse interstitial expansion (as well as focal scar) has become widespread. This technique is based on measurements of Extracellular Volume (ECV) fraction and can be applied in different fields such as oncology, nuclear medicine, cardiology, or infectious diseases (Zamecnik, 2005; Scully et al., 2018). For instance, the best non-invasive technique for visualising and assessing ECV in cardiac focal fibrosis is magnetic resonance imaging (MRI) using Late Gadolinium Eenhancement (LGE), because of the high contrast, high spatial resolution and whole tissue coverage (Scully et al., 2018). Recent studies show that the ECV fraction can also be assessed with Computed Tomography (CT) (Altabella et al., 2017). Both techniques use an extracellular CA that lingers in extracellular water in areas of fibrosis, due to a higher volume of distribution and slower kinetics. It is noteworthy that until recent years, diagnosis and quantification of diffuse fibrosis remained challenging and limited to the domain of the pathologist, who was able to measure the extracellular matrix directly on histological sections using specific stains for connective tissue (Anderson et al., 1979). Moreover, no useful blood biomarkers are currently extant. The increasing interest for ECV (jointly with the development of MRI and CT techniques) is highlighted by the increase in publications on this topic: for instance, the total number of publications on ECV just exceeded a 5 per year until 5 years ago, whereas currently reached a six-fold increase, with over 30 publications per year. The aims of this work were

i) to investigate on the accuracy of ECV measurements obtainable by CT or MRI;

ii) to investigate on possible uses in clinics.

In the first part of this work, several test objects were implemented for ECV estimation with both MRI and CT, covering the relevant range of ECV values associated to tissues of interest. The test objects were vials (falcon, or blood test

vial) in which solid objects (which were inert chemicals, at room temperature and pressure) were inserted, creating a physical compartmentalisation of the water content. The test objects were examined with CT and MRI conventional imaging protocols used for clinical examinations, to investigate on the quantification accuracy.

The second part of this work focused on ECV quantification in some clinical applications. In the first application, a group of patients, undergone MR examination for known or suspected heart disorder was examined, assessing the ECV performance as predictive value for cardiologic diseases. In the second application, CEMRI (Contrast-Enhanced MRI) data of patients with newly diagnosed brain tumors were retrospectively reviewed, calculating the ECV values. Finally, the third application examined the possibility to perform a patient-specific estimation of the Red Marrow (RM) ECV, which is needed to calculate the absorbed dose to RM for evaluating tolerability of radioimmunotherapy treatments, or other treatments with radiopharmaceutical having large carrier molecules, in a nonmyeloablative setting.

5.1 Test objects design and materials

Several test objects were made to test the accuracy in ECV estimation with MR and CT. Each test object consisted of a vial (falcon, or blood test vial), containing some solid objects (inert chemicals at room temperature and pressure) and water, to create a physical compartmentalisation of the water content. The materials constituting the solid objects used in this work consisted in plastic beads, glass spheres and some commercial spongy materials. Figure 5.1 shows some of the test objects by means of zoomed images.

These materials are not certified by regulatory institutions, but main features declared by manufacturer were considered and summarised in table 5.1 (Klyosov, 2007; Vasile and Pascu, 2005).

Table 5.1. Main features (such as, dimension and nominal density) for the materials used: LDPE, Low-Density Polyethylene; PE, Polyethylene; PP, Polypropylene. PS, Polystyrene; n.a., not applicable.

Test Objects	Material [Reference]	Density g/cm^3	Nominal diameter (mm)
Beads (B1)	PS (Wypych, 2016)	1.1	1
Beads (B2)	PS (Wypych, 2016)	1.1	2
Beads Mix ($Bmix^a$)	PS (Wypych, 2016)	1.1	n.a
Beads (B3)	Glass (Zhou et al., 2004)	2.4	3
Spheres (S)	Oroglas (Klyosov, 2007)	1.18	6
Sponge (S1)	LDPE (Klyosov, 2007)	$0.915 - 0.925^b$	n.a
Sponge (B2)	HDPE (Klyosov, 2007)	$0.941 - 0.965^b$	n.a
Sponge (B3)	PP (Klyosov, 2007)	$0.895 - 0.920^b$	n.a

The test objects were examined with CT and MRI conventional imaging protocols used for in-vivo clinical examinations. After the first scan, the water in each test object was replaced by a CA solution, and the examination was repeated. The iopromide (Ultravist® 370, Bayer Inc.) and gadobenate dimeglumine (Gd-BOPTA, Multihance, Bracco, Milan, IT) were used as CAs for MR and CT, respectively, preparing two stock solutions in which the CA dosage for a patient weighing 70

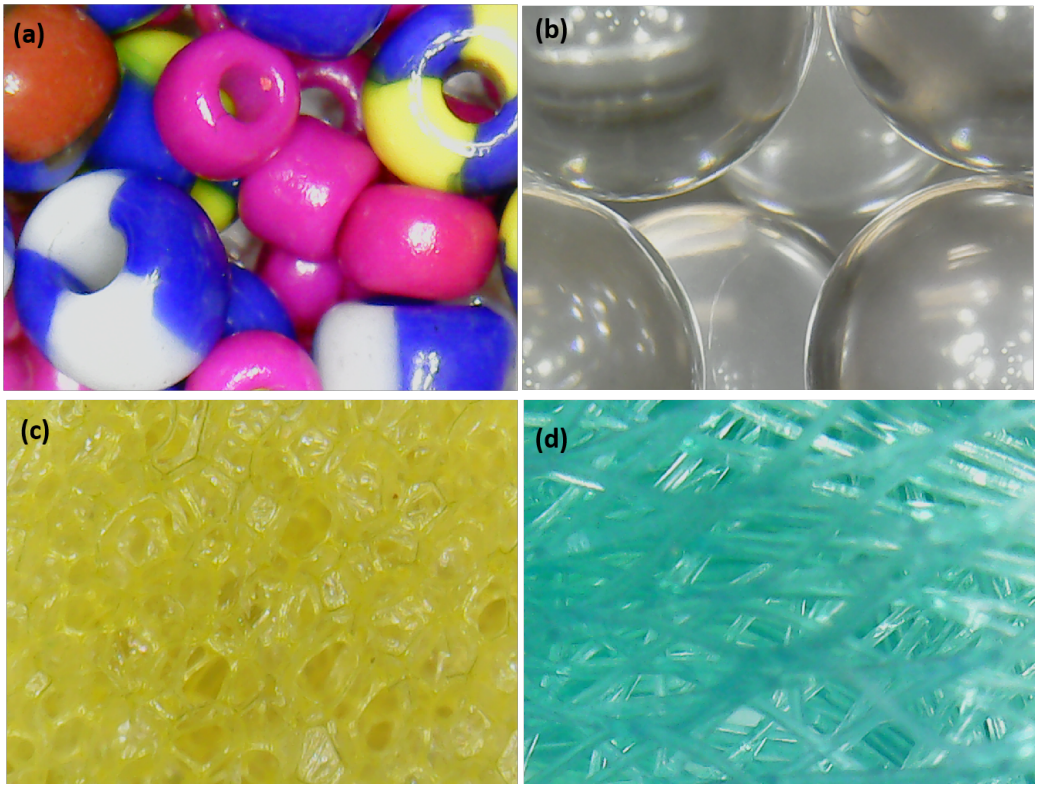

Figure 5.1. Example images of visual appearance of the test objects obtained with a 40x microscope: (a) Beads mix (BMIX), (b) Spheres (S), and in (c) and (d) two types of Sponge (S1 and S3, respectively).

kg (Aime et al., 2005) was diluted in 5 L of water to mimic the dilution in blood, obtaining final concentrations of about 40 g/L, and 70 mg/L, respectively. For each test object, reference ECV (ECV_{ref}) was calculated by the following expression

$$ECV_{ref}(\%) = \frac{V_{water}}{V_{water} + V_{material}} \cdot 100 \tag{5.1}$$

where Vwater and Vmaterial are water and material volume contained in the test object. V_{water} and $V_{material}$ were assessed by precision weighing of materials (using a Mettler AE 200, Mettler Toledo GMBH, Switzerland) and with density values reported in table 5.1. A mean value was assumed for the spongy material density, as solely the density range was available. Values of water and material volume are reported in table 5.2, for each test object, together with the corresponding reference value for ECV (ECV_{ref}). The values of ECV_{ref} were compared with those obtained from MR and CT images of the test objects. Flasks of physiological solution were tied around the test objects, to simulate tissue in-vivo conductivity during MR acquisitions, or surrounding tissue attenuation for CT images. Reminding that the fraction of distribution in the blood volume is 1-Hct (where Hct is the patient haematocrit, i.e., the ratio between red blood cell volume and total blood volume), the ECV for a given tissue can be calculated from images using the following expression:

$$ECV(\%) = (1 - Hct) \cdot \lambda \cdot 100, \tag{5.2}$$

where λ is a ratio between the change of a given tissue parameter due to the CA presence and the change of the same parameter referred to blood. For test objects, water mimics the blood, so expression 5.2 was applied assuming Hct = 0. For MR, λ can be expressed as follows:

$$ECV(\%) = \frac{\Delta R_{1,Tissue}}{\Delta R_{1,Blood}} \tag{5.3}$$

where $\Delta R_{1,tissue} = (1/T_{1,post} - 1/T_{1,pre})_{tissue}$ and $\Delta R_{1,blood} = (1/T_{1,post} - 1/T_{1,pre})_{blood}$ are the enhancement of the longitudinal relaxation rate (R_1) for tissue and blood pool, respectively, due to the presence of the CA. Using the test objects, $\Delta R_{1,tissue}$ represents the change of the relaxation rate in the test object, whereas $\Delta R_{1,Blood}$ is the change of the relaxation rate in water. The test objects were imaged with a 1.5 T MR tomograph (Magnetom Avanto, Siemens Healthcare). T_1 maps were obtained with an IR (gold-standard) sequence with 25 inversion times (TIs) in the range 100-2500 ms and interpolating signal data with the well-known three-parameter-curve for modelling longitudinal relaxation and the Levenberg Marquardt algorithm (Borrazzo et al., 2019). For CT, λ assumes the following expression:

$$ECV(\%) = \frac{\Delta HU_{1,Tissue}}{\Delta HU_{1,Blood}} \tag{5.4}$$

where ΔHU= $HU_{post} - HU_{pre}$ (i.e., the change in Hounsfield units pre and post-injection of the CA, with tissue and blood represented by test object and water, respectively) (Scully et al., 2018) (for more details see appendix A). The ECV value was calculated as mean value in a three-dimensional ROIs (Regions of Interest) encompassing the whole vial content (test object or water, with or without CA), and applying expressions 5.2 and 5.3 to mean T_1 values obtained from MR images, or expression 5.2 and 5.4 to mean HU obtained from CT images. The accuracy associated to mean ECV measured by CT or MR is defined as

$$ECV(\%)\, accuracy = \frac{ECV_{measured} - ECVref}{ECV_{ref}} \cdot 100. \tag{5.5}$$

5.2 Patient studies

5.2.1 Heart disorders

60 patients with known/suspected heart disorder (17 myocarditis, 16 hypertrophic cardiomyopathy, 12 dilated cardiomyopathy, 5 pulmonary hypertension, 5 non-compacted cardiomyopathy and 5 cases with acute amyloidosis conditions) and 20 healthy controls were examined with CEMRI. MR acquisitions were performed with 1.5 T MR tomograph (Magnetom Avanto, Siemens Healthcare, at Erlangen Germany). For each subject, 3 slices were acquired on short axis views in apical, basal and mid-ventricular plane, pre- and post-injection (15 min later) of a Gd-BOPTA bolus (gadobenate dimeglumine, 0.1 mmol/kg) (Borrazzo et al., 2019). Pre- and post-contrast acquisitions were performed using MOLLI (modified Look-Locker

inversion-recovery) sequences: a pre-contrast sequence scheme of 5(3)3 (i.e. 5 images are acquired starting from the first TI, and after a three-cardiac cycle pause, 3 additional images are acquired starting from the sixth TI), and a 4(1)3(1)2 post-contrast sequence were chosen to decrease the scanning time assuring comparable accuracy and precision (see appendix A). The sequence parameters were matrix size = 218 x 256, voxel size = 1.41 x 1.41 x 8 mm^3, TR/TE = 2.8/1.1 ms, and Flip Angle = 35°. Signal images referred to various TI were systematically motion-corrected and coregistrated, using software provided by the manufacturer (Xue et al., 2012). Signal processing was performed by a method based on a Fast Non-linear Least Squares (FNLS) algorithm (Altabella et al., 2017), obtaining a T_1 map and lastly an ECV map (for more details see section 4.2). Values of patient myocardial ECV reported here were obtained as an average in a ROI delineating the myocardium region in the basal slice. The ROI was drawn on the pre-contrast T_1 map (thresholding pixels with values equal or higher than the typical blood T_1 at the given frequency), and overimposed on the ECV map (see Borrazzo et al. 2019 for further details).

5.2.2 Brain cancers

Three patients (2 men, 1 women) were studied with MRI for neurological disorder (2 pilocytic astrocytomas and 1 glioblastoma multiform). MRI studies were performed on a 3T scanner (Siemens, Erlangen, Germany). Standard MR imaging in all patients consist of multiplanar pre- and post-contrast T_1-weighted images. The sequence parameters were: matrix size = 112 × 122, FOV = 230 mm, voxel size = 2.05 × 2.05 × 3 mm^3, TR = 5 s, and Flip Angle = 15°. Seventy dynamic scans were performed with a temporal resolution of 5 s. The total acquisition time for CEMRI was 6 min. A single bolus of Gd-BOPTA (gadobenate dimeglumine, 0.1 mmol/kg) was injected 20 s after the start of scanning at an injection rate of 2 ml/s. 2D ROIs were drawn manually to delineate the tumour and the blood region (a visible blood vessel) in the same slice, on the pre- and post-contrast signal image. The mean pre- and post-contrast T_1 values were obtained in each region with the same methodology for signal fitting reported in the section 5.1, and the ECV was estimated applying expressions 5.2 and 5.3.

5.2.3 Radioimmunotherapy

The radioactivity into the RM due to a treatment with radio-labelled monoclonal antibodies (or with another radiopharmaceutical having larger molecules than tissue cells) can be calculated by the "blood method" (Sgouros, 1993), in which the radioactivity concentrations in RM is expressed by multiplying the radioactivity concentrations in blood by the ratio between the RM extracellular fluid fraction (RMECFF) and the ECV of blood (i.e., 1-Hct). This proportionality factor is usually named red marrow-to-blood activity concentration ratio (RMBLR):

$$RMBLR = \frac{RMECFF}{1 - Hct} \tag{5.6}$$

where RMECFF is estimated here by the RM ECV (Sgouros, 1993). In this clinical application, the factor reported in expression 5.6 was assessed by that

reported by expression 5.3 or 5.4 (depending on the images used). Ten patients (6 men, 4 women) randomly selected from the 20 healthy controls mentioned above (see subsection "Heart disorders") were examined. The mean ECV of the Spongiosa Volume (SV) inside a thoracic vertebra at the heart level (visible vertebrae were one or two, between T1 and T4) was obtained as mean value in a 2D ROI, delineating the SV on the ECV map previously calculated (see subsection "Heart Disorders"). Another group of 10 patients (5 men and 5 women) examined by CT and resulting not affected by diseases were also included in this study. CT examinations were performed with a 64-detector row CT scanner (Somatom Sensation 64; Siemens Medical Solutions, Erlangen, Germany). Cardiac scans (tube voltage, 120 kV; tube current-time product, 160 mAs; section collimation, 64 detector rows, 1.2-mm section thickness; gantry rotation time, 330 ms) were acquired with prospective gating (65%-75% of R-R interval) and reconstructed into 3-mm-thick axial sections, using a B20f kernel. The mean HU pre- and post-injection of the CA was calculated, with 2D ROIs delineating the SV of a dorsal vertebra at the heart level (as in the case of the MR patients above mentioned), and a blood region (typically located in the left ventricular blood pool). The ECV of the SV inside the dorsal vertebra was then obtained using expressions 5.2 and 5.4.

5.3 Results

5.3.1 Test objects

Figure 5.2 reports an example of axial and sagittal plane images of the S test object, acquired with MRI and CT (left and right, respectively), pre- and post- CA administration top and bottom, respectively).

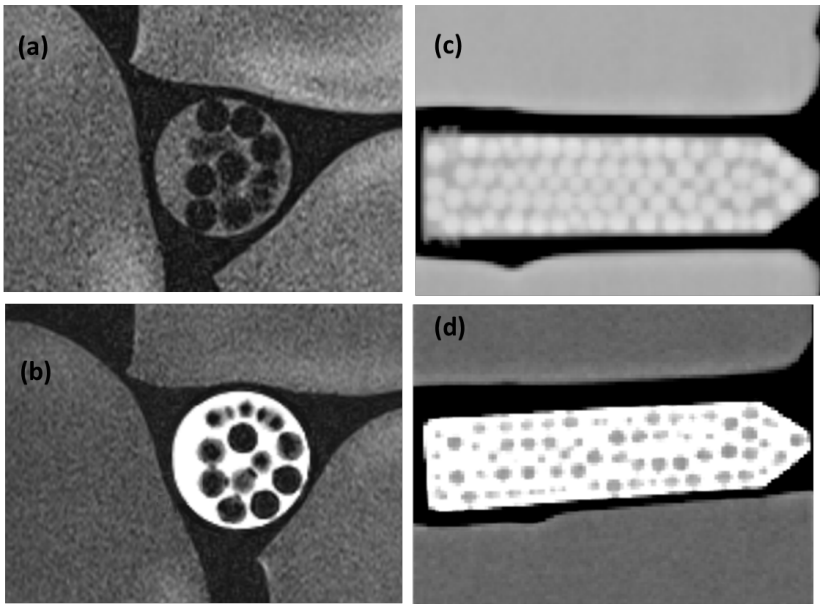

Figure 5.2. . Examples of test object images: pre-contrast (a) and post-contrast (b) axial T_1-weighted MR images, and pre-contrast (c) and post-contrast (d) sagittal CT images for the S test object.

Table 5.2 summarizes the ECV values calculated by CT and MR images, together with the corresponding ECV_{ref}.

Table 5.2. ECV values obtained from test object images acquired by CT and MRI.

Test objects	ECV_{ref}	ECV_{CT}	ECV_{MR}
B1	0.182	0.191	0.202
B2	0.316	0.309	0.281
BMIX	0.468	0.481	0.442
B3	0.521	0.545	0.455
S	0.471	0.469	0.493
S1	0.865	0.886	n.a
S2	0.711	0.769	n.a.
S3	0.479	0.522	n.a.

Figure 5.3 (a) provides a scatterplot of data reported in table 5.2, showing the correlation between the ECV_{ref} and values measured on images, differentiating between CT (white circles) and MRI (black rhombus). A linear correlation can be observed: a slope of 0.945 (95%CI: 0.93-1.15) and an R-value of 0.98 (95%CI: 0.96-1.1) were obtained. The accuracy of ECV measurements, calculated according to expression 5.5, is reported in figure 5.3 (b) for each test object, differentiating between CT and MRI. The overall differences were between -9% and 13%, with mean differences for CT of 3%, and for the MRI of -2%.

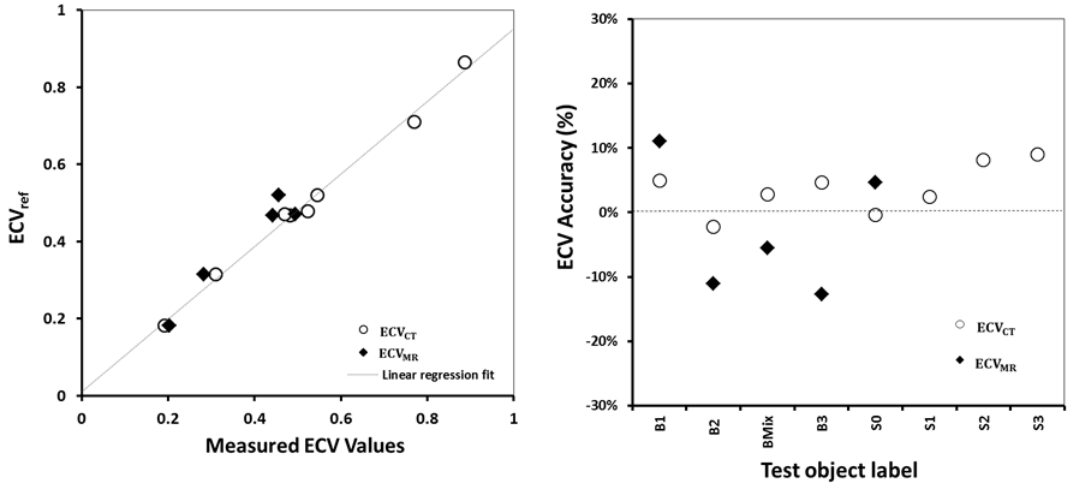

Figure 5.3. Correlation and accuracy in ECV measurements of test object: (a) correlation between reference and measured values, (b) accuracy of ECV measured by CT and MRI images. White circles and black rhombus represent measurements in CT and MRI, respectively.

Analogously, paired comparison for ECV with Bland-Altman analysis (reported in figure 5.4) did not evidence significant differences except for one point slightly outside the limits of agreement.

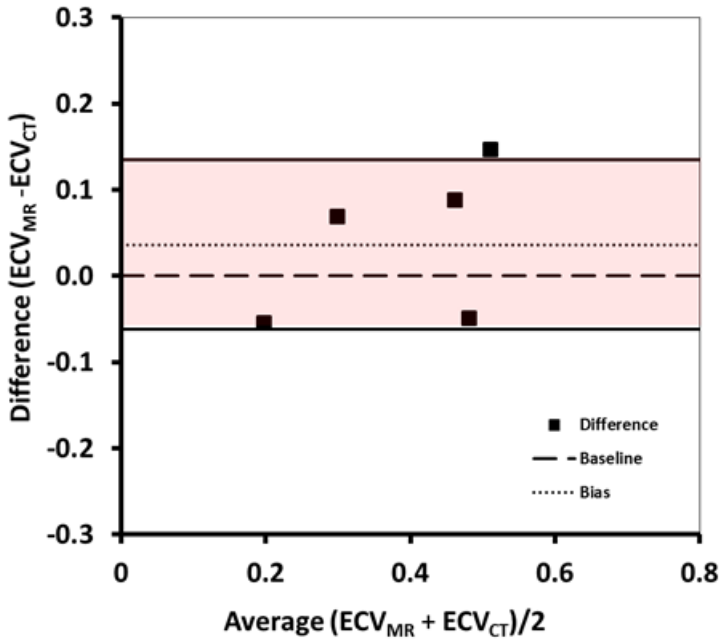

Figure 5.4. Bland–Altman plots showing paired comparisons for the ECV measurements: The 95% confidence interval (red region) and bias (dotted line) are also displayed.

5.3.2 Patient studies

The second part of this work focused on ECV quantification obtained in clinical applications (see section 5.2). Figure 5.5 shows MR (a-c) and CT (d) images from four sample clinical cases, showing also the ROI encompassing the target tissue.

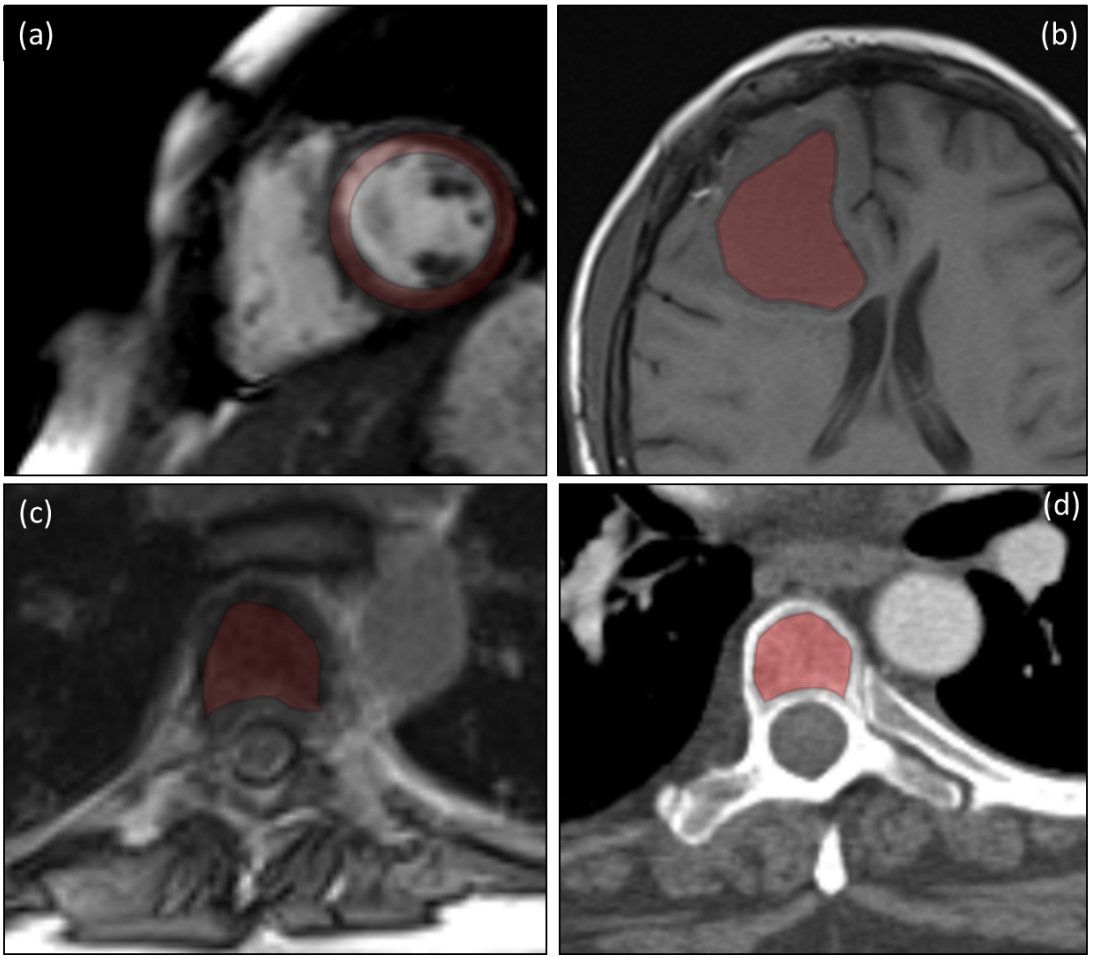

Figure 5.5. Examples of MRI and CT post-contrast images from clinical cases: (a) gadolinium-enhanced MR signal image with a ROI encompassing the myocardium wall, in axial slice. (b) Axial MR signal image of a patient with a glioblastoma in the right temporal lobe, and the associated ROI. (c) Axial MR signal image of a thoracic vertebra at the heart level (T1), with the ROI drawn on the spongiosa volume. (d) Axial CT image of a thoracic vertebra at the heart level (T2), with the ROI encompassing the spongiosa volume.

Myocardial ECV

Data are reported in table 5.3, differentiating according to the disease: median and IQR were reported, together with the corresponding p-value of the Mann Whitney test, with respect to healthy patients.

Table 5.3. . Myocardial ECV (median and IQR) were reported, differentiating data among diseases (17 myocarditis, 16 hypertrophic cardiomyopathy, 12 dilated cardiomyopathy, 5 pulmonary hypertension, 5 non-compacted cardiomyopathy and 5 cases with Amyloidosis conditions), together with the corresponding Mann Whitney p-value with respect to healthy patients (20 patients).

Patients	ECV (%) Median (IQR: 25%-75%)	p-value
Healthy	26.1 (23-30.0)	–
Myocarditis	35.2 (33-37.3)	<0.001
Hypertrophic cardiomyopathy	31.1 (27-39.6)	0.002
Dilated cardiomyopathy	27.8 (27-28.8)	0.061
Pulmonary hypertension	28.6 (27-33.7)	0.113
Non-compacted cardiomyopathy	27.9 (25-29.5)	0.450
Acute amyloidosis	46.7 (44-47.9)	<0.001

Figure 5.6 (a) reports a Boxplot comparing the ECV in healthy and diseased patients, considering the latter as a whole dataset. The ECV median values of the healthy controls was 26.1% (IQR: 23%-30%) (mean value: 27%). The ECV median values of the diseased patients was 34.2% (IQR: 31%-54%) (mean value: 40.1%).

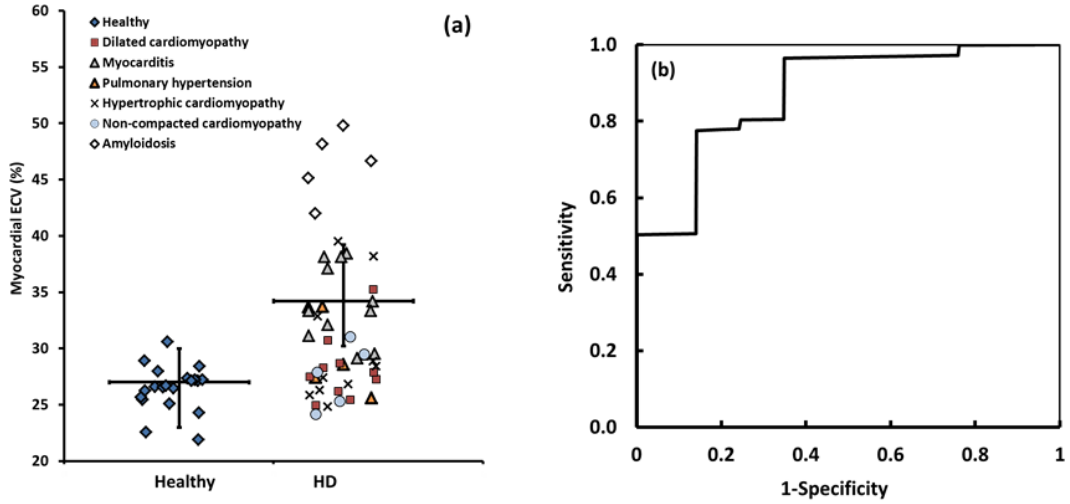

Figure 5.6. (a) Boxplot comparing ECV (%) in healthy controls and patients affected by heart disorders. The p-value of the Mann-Whitney test is also reported. (b) ROC curve obtained using the ECV as score.

The two groups of values differed significantly between them (p=0.002). The ROC curve in figure 5.6 (b) (calculated assuming ECV as score) highlights that ECV has a predictive value, indeed ROC curve analysis showed an AUC of 0.882 (95%CI: 0.757-0.987). The optimal threshold for ECV was 28.4 (about the same

value obtained as mean value from the healthy patients), obtaining a sensitivity of 0.920 (95%CI: 0.591-0.982) and specificity of 0.857 (95%CI: 0.518-0.997), with a diagnostic accuracy of 76.1%.

Brain cancers

Three patients having enhanced tumors confirmed by biopsy were selected: 2 tumors were classified as low-grade (2 pilocytic astrocytomas) and 1 were classified as high-grade (1 glioblastoma multiform). Median ECV was 23% (IQR: 20%-27%) (95% CI: 14%-31%), but for the high-grade tumour ECV seemed lower (value: 16%) than for low-grade tumors (23% and 32%).

Red marrow ECV

The median ECV of the SV was 22% (IQR: 17%-23%) for CT and 23% (IQR: 22%-26%) for MR, considering two different groups of healthy patients. Mann-Whitney test did not evidence any significant differences between the two imaging modalities (p=0.100). Considering the two groups as a whole dataset, values are normally distributed (p=0.406) around a value of about 22% (95% CI: 20%-25%, see table 5.4). RMBLR was calculated by expression 5.6, considering the ECV as the estimation of the RMECFF, and accounting for the patient HCT (values ranging from 0.34 up to 0.49): the median RMBLR was 33% (range of 19%-47%), in a good agreement with the range of 20%-40% generally reported in the literature (Sgouros, 1993).

Table 5.4. Patient-specific RM ECV (%) and RMBLR.

Patients	Medical imaging Technique	$ECV(\%)$	RMBLR
1	CT	19.1	36.9
2	CT	29.2	44.7
3	CT	22.3	33.7
4	CT	22.6	32.7
5	CT	23.3	35
6	CT	16.4	24.5
7	CT	23.1	33.5
8	CT	24.7	36.7
9	CT	15.3	23
10	CT	17.4	26.4
11	MR	21.3	31.6
12	MR	27	40.3
13	MR	23.3	39.4
14	MR	26	35
15	MR	23.4	35.3
16	MR	32.1	47.1
17	MR	26.2	41.6
18	MR	19.1	28.9
19	MR	23.1	36
20	MR	13.4	19.1
Mean 95%CI	–	22(20-25)	34(30-37)

5.4 Discussion and Conclusion

This study is the first to propose the creation and use of test objects dedicated to validation measures for ECV in MR and CT applications, but the error affecting experimental estimation of ECV_{ref} are difficult to quantify due to some limitations, mainly:

i) use of non-certified materials, for which only the nominal density (or the density range) is known;

ii) the vials containing the materials were filled with water or CA solution and subsequently closed, creating percolation processes and air bubbles' trapping.

The former produced an error that cannot be evaluated. The latter causes that an image parameter obtained by a ROI drawn on a single slice may not be representative of the entire test object; so, its influence was minimized by a 3D contouring of the test object content, which in turn could introduce errors, even if of a lesser extent than those due to the presence of air bubbles not taken into account. Additional source errors on ECV estimations should derive from the imaging of the object and were reported for MR in a previous publication (Borrazzo et al., 2019). Nevertheless, even though an exhaustive error analysis is not possible here, a maximum inaccuracy of 13% (referred to MR, see figure 5.3) seemed encouraging when compared to the uncertainty of ECV previously published (about 10%) (Borrazzo et al., 2019), considering the above-mentioned limitations. It is also noteworthy that the creation of test objects for both MR and CT, covering a relevant range of ECV values for clinical applications (Scully et al., 2018; Luetkens et al., 2019), is straightforward, even though the determination of the accuracy on ECV_{ref} would require certified materials.

Statistical tests and Bland–Altman analysis did not show significant differences between ECV values measured by MR and CT. The estimated inaccuracy affecting the ECV obtained from images was similar between CT and MR, probably basically and slightly higher for MR (differences between -13% and 11%) than for CT (differences between -2% and 9%, see also figure 5.3). This study confirmed that the ECV determination is technically feasible also as part of a conventional pre- and post-contrast CT examination, without extra amount of CA and at a standard exposure level.

In recent years, some studies showed that the ECV fraction can also be evaluated with CT (Graser et al., 2009; Hong et al., 2016). ECV imaging by CT lags the MR field but is potentially an attractive alternative. Though the evidence base for ECV in MR may be larger and experience greater (above all, in cardiology examinations), the use of CT could present some advantages. In CT, ECV measures the direct effect of iodine-based contrast agents on the measured signal (through the effect of iodine on x-ray absorption), whereas ECV in MR relies on measuring the effect of CAs on protons, therefore making two assumptions: i. the relaxivity of tissues compared to blood is the same, and ii. water is rapidly exchanged between intra- and extracellular compartments. Also, common contraindications to MR such as claustrophobia and pacemaker implantation (the latter being not uncommon, for example in patients with cardiac amyloid where ECV quantification could prove

helpful) do not apply for CT. Other authors used also dual-energy CT to quantify myocardial ECV, which is attractive, in principle, as it would potentially avoid mis-registration errors associated with the separate pre- and post-contrast scans, by obviating the need for the pre-contrast scan (Graser et al., 2009; Hong et al., 2016). On the other side, CT examinations imply the patient exposure to ionising radiations, differently from MR.

The second part of this work focused on ECV quantification in some clinical applications. In the context of heart disease, myocardial ECV values obtained in normal subjects (range: 23%-30%) were in a good agreement with previous studies, reporting values between 22%-34%. Also, for the diseased subjects examined here, the ECV median value was 34.2% (IQR: 31%-54%), in a good agreement with the values reported by previous studies (Borrazzo et al., 2019). The ROC analysis was performed to investigate on the ECV predictive value to distinguish between healthy and disease patients, obtaining an optimum threshold of 28.4%, corresponding to an excellent sensitivity (92%) and a good specificity (88.9%). This threshold value could be tentatively assumed for clinical studies. ECV optimum threshold for myocardial disease obtained here was in a good agreement with previous studies (threshold value: 28%-30%) (Chen et al., 2019). Considering disease patients as a whole dataset, the wide variability of data reflects the heterogeneity in clinical conditions, but some data stratification appears differentiating data among pathologies and according to the number of cases, also in a substantial agreement with the literature (Scully et al., 2018). In the second example of application, CEMRI data of patients with diagnosed brain tumors were retrospectively reviewed. After estimation of ECV values with the methodology proposed in this work, the obtained results were also compared with those obtained from MR perfusion images (also available for the three patients here considered), analysing data with the Tofts model (Borrazzo et al., 2018), obtaining a good agreement (within 10%, data not shown). The obtained ECV values were also in a good agreement with a previous study concerning paediatric patients (38 patients; range: 19%-26%; methodology: Tofts model) (Vajapeyam et al., 2017), but at the same time another recent study reports significantly different values (83 adult patients; range: 6%-21%; methodology: Tofts model.) (Conte et al., 2019), thus highlighting the need for further studies in this area.

In the third example of application, the ECV for the spongiosa volume of thoracic vertebrae was derived from images and assumed as RM ECV. These data are of interest for RM dosimetry in radioimmunotherapy, or when large carrier molecules are used in a nonmyeloablative setting. When a slow clearance is involved (e.g., antibodies), the RM is the dose-limiting organ, so RM dosimetry should be performed to evaluate the treatment tolerability, considering a threshold value of absorbed dose of 2 Gy. RM dosimetry is usually performed by a two-compartment model (RM, i.e., self-irradiation, and remainder of body) (Sgouros, 1993). The self-irradiation contribution can be estimated by the "blood method" Sgouros (1993), i.e., the radioactivity concentrations of blood samples is used to estimate that in RM, multiplying the blood radioactivity concentrations by the RMBLR, calculated as the ratio between patient-specific RMECFF and 1-HCT Wessels et al. (2004); Sgouros (1993). Individual quantification has never occurred so far, assuming a baseline value of 0.19 (derived from a study of rabbit femur). The possible use of both MR and CT for estimating the patient-specific RMECFF (i.e., the RM ECV) was here

investigated, obtaining no significant differences between them. Considering the overall dataset, a mean ECV of 22% was obtained, which is in a worthy agreement with the traditional baseline value of 0.19, but a wide variability range of 13-32% was also observed. Even though the overall results in terms of RMBLR are in a good agreement with the range of 20-40% generally reported in the literature (see table 5.4 in the results), the individual results evidence that the estimation of the absorbed dose to RM could lead to inaccuracies when just the baseline value of 0.19 is used. So far, a satisfactory correlation between RM dosimetry and adverse effects has never been highlighted in radioimmunotherapy with pure beta emitters, and this could be an indication of the importance of patient-specific RM ECV in dosimetric estimations. Currently, the characterisation of the spongiosa complex micro-anatomy is still an issue and ECV quantification could also be helpful. A further and indubitable result of this work is that ECV is easy to obtain also when examinations are not performed directly for this purpose, making possible also real-time ECV estimation, as well as paves the way to machine learning-related applications (Borrazzo et al., 2019).

CT and MR can be used to estimate ECV without the need of invasive biopsy. Each modality has strengths and weaknesses, with CT resulting as an attractive alternative to MR, particularly when contraindications to the MR are present. Accuracy improvements and uncertainty estimation for ECV obtained from images are currently under investigation. Additional investigations would be also required for brain cancers, as the literature reports conflicting data. Possible corrections for RM ECV estimations, due to the heterogeneity of trabecular bone (e.g., presence of yellow marrow/fatty tissue into the SV), are still under study. However, the results obtained in this work from patient studies are mostly in a very good agreement with those reported in the literature, confirming that the ECV estimation from clinical examination is promising and easy to obtain also when examinations are not performed directly for this purpose.

Chapter 6

Unexpected increase of myocardial extracellular volume fraction in low cardiovascular risk HIV patients

Myocardial Extra-Cellular Matrix (ECM) is a complex biological network consisting of a wide variety of proteins (principally glycoproteins, proteoglycans, and glycosaminoglycans) in which cardiac myocytes, fibroblasts, vascular cells, and leukocytes dwell. ECM proteins participate to myocardial strength and plasticity and play a fundamental role in cardiac development, homeostasis, and remodelling (Rienks et al., 2014). ECM alterations may indicate a loss of cardiac morphological homeostasis and may represent an indicator of Cardiovascular Diseases (CVD). ECM expansion has been linked to electrical, mechanical and vasomotor dysfunctions, cardiac fibrosis and, eventually, increased mortality (Schelbert et al., 2014; Wong et al., 2014). Contrast enhanced Cardiac Computed Tomography (CCT) and Cardio-Vascular Magnetic Resonance (CMR) use extracellular extravascular contrast agents to non-invasively quantify the myocardial ExtraCellular Volume (ECV) Wong et al. (2014); Altabella et al. (2017); Borrazzo et al. (2019). In particular, CCT is increasingly used in experimental and clinical setting, due to its opportunity to assess lots of cardiac features other than ECV and fibrosis (such as coronary anatomy, calcification etc) in a very shorter time and with a higher spatial resolution than MRI (Altabella et al., 2017; Borrazzo et al., 2019). Although combined Antiretroviral Therapy (cART) has improved both the length and quality of life of people living with HIV (PLWH), cardiovascular diseases represent a challenge for clinicians and are still a leading cause of death in this population. Several studies have shown an increased frequency of coronary atherosclerotic disease, myocardial infarction, arrhythmias and sudden cardiac death (SCD) in PLWH (Shah et al., 2018). Interestingly, recent studies have shown that severe CV diseases are more frequent than expected in PLWH with a low Atherosclerotic Cardiovascular Disease (ASCVD) score, possibly as a result of premature aging due to inflammation, immune-activation, cART side effects and direct viral effect (Grunfeld et al., 2009).

Therefore, algorithms developed to predict CV risk in the general population

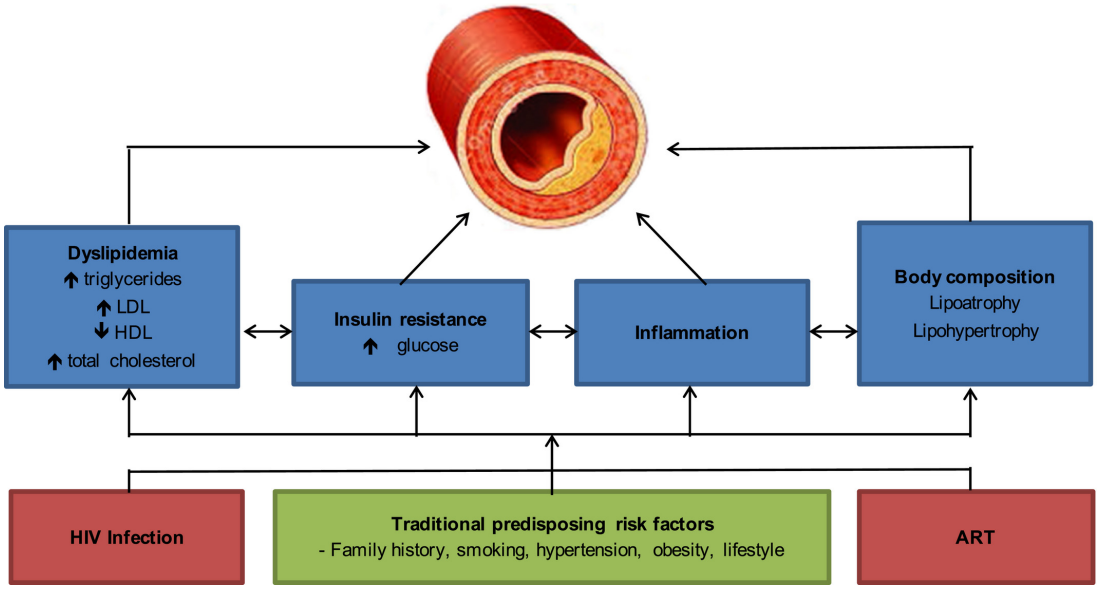

Figure 6.1. Multifactorial pathogenesis of increased risk of coronary artery disease (CAD) in treated HIV-infected patients. ART, antiretroviral therapy; HDL, high-density lipoprotein; LDL, low-density lipoprotein (Nadel and Holloway 2017).

could be inaccurate when applied to PLWH (Ceccarelli et al., 2013). In this scenario, the aim of our study was to assess ECV in PLWH with low-ASCVD score and to compare ECV of HIV+ subjects to that of a control group.

6.1 General Characteristics

A total of 71 subjects were included in the present study (18 controls and 53 asymptomatic HIV-positive patients). The main characteristics of participants are summarised in table 6.1 (anthropometrics, CV risk factors, metabolic status, immune-virologic status of HIV+ subjects). No significant differences were found between the two groups in terms of gender distribution, age and other major risk factors (p-value$>$ 0.050).

Severity of HIV disease was categorized following the Center for Diseases Control and Prevention classification: 20 (38%) patients were in category A2, 10 (19%) patients in category A3, 2 (4%) patients in category B3, 3 (6%) patients in category C2 and 18 (34%) patients in category C3. Median CD4+ nadir before initiation of cART was 181 (IQR: 94-300) cells/μL. During their therapeutic history, 38 of the 53 HIV+ participants received at least one protease inhibitor (PI) for a median of 3 (IQR: 0-14) years, while 23 HIV+ received a nonnucleoside reverse transcriptase inhibitor (NNRTI) for a median of 1 (IQR: 0-9) years. With cART, plasma viremia was undetectable (lower limit of detection of 37 copies/mL) in all HIV+ subjects.

Table 6.1. Baseline characteristic of the study cohort. Median and interquartile range (IQR: 25%-75%) or mean ± SD are reported for continuous variables. Simple frequencies (n) and percentages are reported for categorical variables. Abbreviations: BMI^a, Body mass Index; HR^b, Heart Rate; HDL^c, High Density Lipoprotein; $PLWH^d$, People living with HIV; NA^e, not applicable).

Parameters	HIV-infected (n=53)	Control group (n=18)	p-value (*)
General characteristics			
Male, n (%)	45 (85)	14 (77)	0.129
Age, Years	48 (42.5-48)	55 (44.5-56)	0.122
BMI[a], kg/m^2	22 (20.3-22)	27 (24–32)	0.116
HR[b], bpm	67 (±9.1)	65 (±11.3)	0.211
Systolic blood pressure, mmHg	119 (±10)	114 (±11)	0.131
Diastolic blood pressure, mmHg	75 (±9)	67 (±6)	0.061
Laboratory results			
Total cholesterol, (mg/dl)	189 (177-189)	188 (154–201)	0.557
HDL[c], (mg/dl)	39 (35-39)	54 (46–66)	0.046
Triglycerides, (mg/dl)	101 (78-170)	124 (80–177)	0.077
Other factors			
Diabetes, n (%)	0 (0)	0 (0)	1.000
Smoking, n (%)	9 (17)	4 (22)	0.686
Framingham Risk (%)	4 (1-6.5)	3 (1-5)	0.182
ASCVD 10 years, calculated risk	4.6 (2.7-4.6)	4.6 (1.7-3.5)	0.286
Immune-virologic status			
Years of therapy, Years	9 (6-9)	-	NA[a]
Years of exposure to HIV infection, Years	10 (1-23)	-	NA[a]
CD4 enrolment (cell/µl)	450 (328-750)	-	NA[a]
CD4 nadir (cell/µl)	181 (94-300)	-	NA[a]
% of PLWH[e] naïve for cART	12.7	-	NA[a]
HIV-RNA copies/ml in cART treated PLWH	<37	-	NA[a]
HIV-RNA copies/ml in cART naive PLWH	55.000	-	NA[a]

The hematocrit value was 35 ± 4% in HIV+ participants and 41 ± 3% in controls (p-value=0.122). No significant differences were observed regarding Heart Rate (HR) during CCT examination (p-value=0.211).

6.2 Measurements of Myocardial ECV

The median ECV value was 27.4% (IQR: 25%-28%) in healthy controls and 31% (IQR: 28%-31%) in HIV+ participants, respectively. In our study population, ECV differed significantly between the two groups (p-value<0.001), thus indicating the presence of ECV expansion in the myocardium of HIV+ subjects (figure 6.2 a and b).

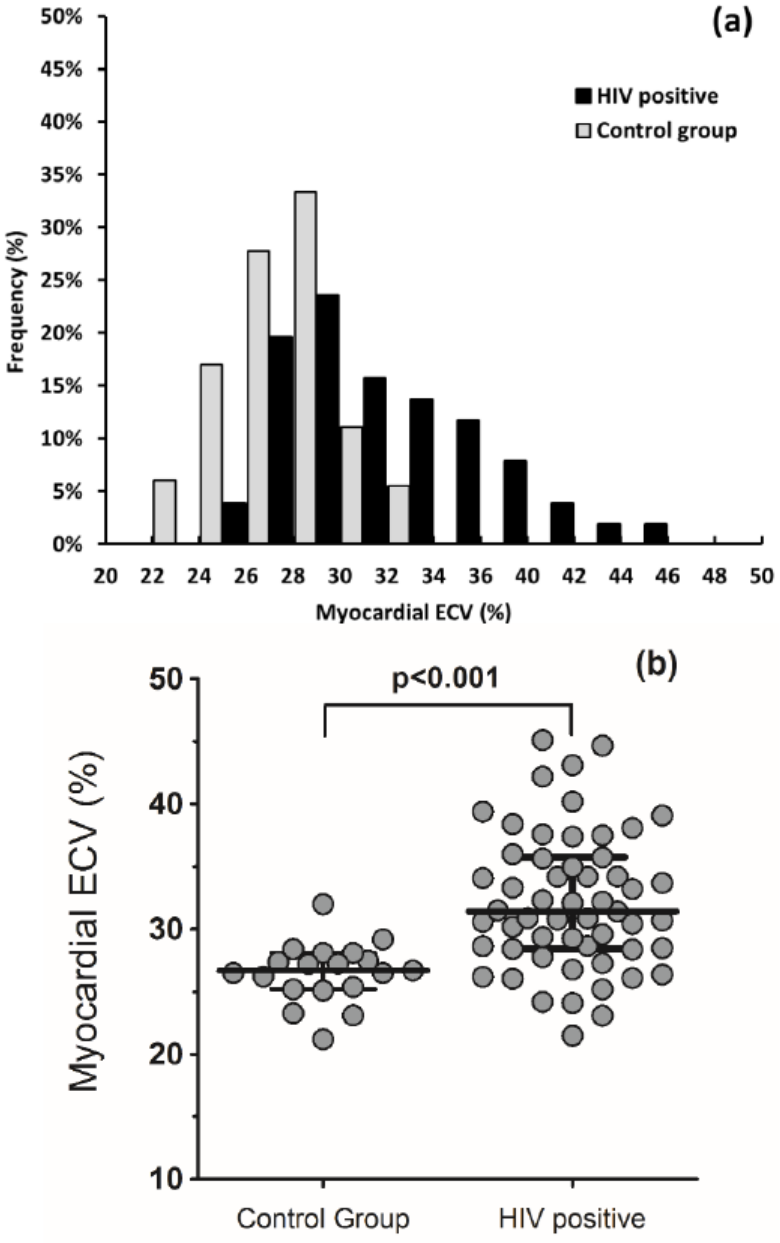

Figure 6.2. (a) Frequency histograms of ECV fraction. (b) Boxplot comparing ECV in controls and HIV+ patients: median, interquartile range (25%-75%) and p-value of the Mann-Whitney test for significance are also reported.

ECV values were not affected by patient's age neither in the HIV+ group (r=0.12, p-value=0.145. Figure 6.3 a) or in controls (r=0.11, p-value=0.102).

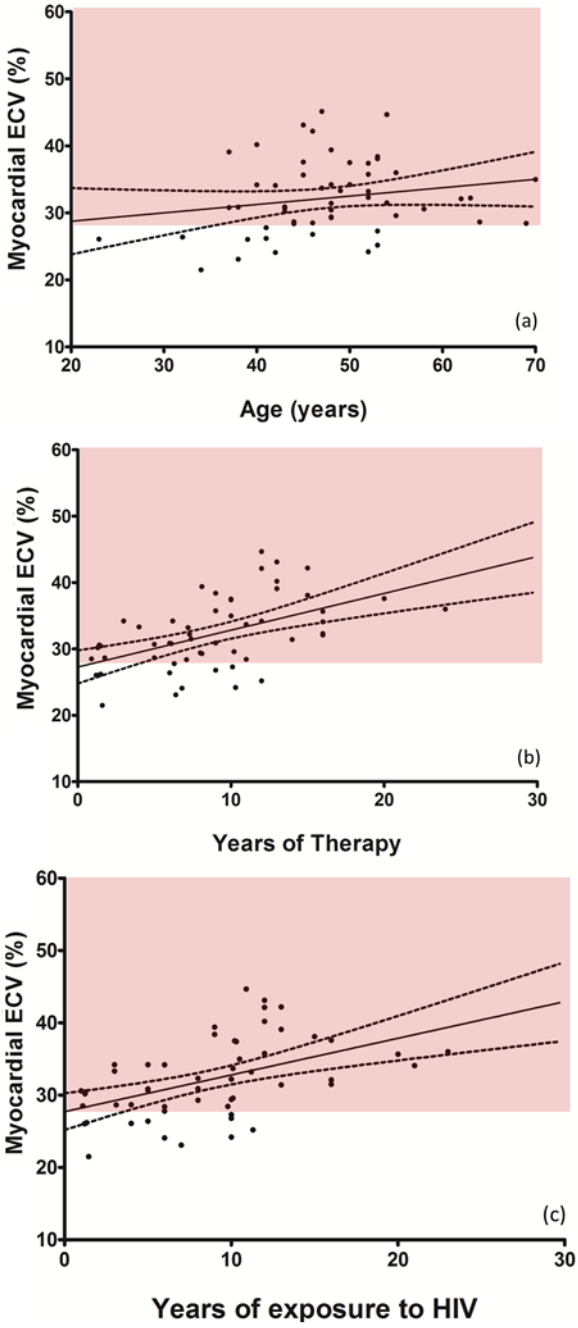

Figure 6.3. Scatter plots and best-fit regression curves (Solid line) with 95% CI bands (shown as dashed lines) of ECV versus age (a), years of therapy (b), and years of exposure to HIV (c) are shown for HIV+ patients. r and p-value are also reported. Red shading denotes the ECV range of the disease zone. Reference intervals are defined from the work of Scully et al. (3).

On the contrary, ECV was found to significantly correlate with the number of years of exposure to HIV infection (r=0.54, p<0.001. figure 6.3 b), and the years on cART (r=0.62, p<0.001. Figure 6.3 c), showing a trend toward ECV expansion over time in HIV infected patients. Based on the years on cART and years of exposure to HIV, all HIV+ patients were divided into three groups: (A) <5 years, (B) 5 to 10 years and (C) >10 years. (There was a significant difference in ECV (ANOVA, p< 0.001) among controls and groups (see table 6.2).

Table 6.2. Myocardial ECV comparisons between control group and HIV-positive patients selected by (A) less than 5 years, (B) from 5 to 10 years and (C) greater than 10 years. Data are shown as Median and interquartile range (IQR: 25%-75%).

Parameters	Controls (n=18)	<5 y (A)	5-10 y (B)	>10 y (C)	p-value (*)
Myocardial ECV (%)	27.4 (25-28)	-	-	-	-
Years of therapy	-	29 (26-30)	30 (27-32)	37 (33-39)	<0.001
Years of exposure to HIV	-	29 (26-30)	31 (28-34)	35 (31-39)	<0.001

The multivariable stepwise linear regression showed that the duration of therapy (β was 0.56 (0.33-0.95), p-value=0.014) and years of HIV infection (β was 0.53(0.4-0.92), p-value<0.001) were independent predictors of ECV expansion (table 6.3).

Table 6.3. (A) Univariate correlation analyses between ECV and characteristics of the HIV+ population. (B) Multivariate regression models for predictors of ECV expansion. Age, Heart Rate (HR), systolic and diastolic blood pressure, years of therapy and years of exposure to HIV infection were entered in this model. P-values as assessed by Pearson's correlation for normal distributions, Spearman's correlation for non-normal distributions as well as β estimates and p-values from multivariate regression models are reported.

Variable	Univariate		Multivariate	
	R (95% CI)	p-value	β (95% CI)	p-value
Intercept	25.5 (21-29.5)	0.210	25.7 (20.2-30)	0.062
Age	0.12 (0.02-0.35)	0.805	0.42 (0.33-0.89)	0.084
Gender	0.29 (0.13-0.42)	0.149	0.19 (0.01-0.34)	0.122
Heart Rate (HR)	0.15 (0.01-0.33)	0.301	1.29 (1.01-1.5)	0.062
BMI (kg/m^2)	-0.26 (-0.01-0.2)	0.068	-	-
Systolic blood pressure	-0.02 (-0.01-0.2)	0.278	-	-
Diastolic blood pressure	-0.05 (-0.02-0.1)	0.191	-	-
Years of Therapy	0.62 (0.44-0.96)	<0.001	0.56 (0.33-0.95)	0.014
Years of exposure to HIV infection	0.54 (0.36-0.90)	<0.001	0.53 (0.4-0.92)	<0.001

6.3 Discussion and Conclusion

Given the efficacy of newer, effective antiretroviral therapies, life expectancy of PLWH has shown a widespread improvement; on the other hand, following the introduction of cART, CVD and cardiovascular deaths have increased dramatically among this population (Shah et al., 2018). Several studies conducted in PLWH with CCT angiography, showed an increased presence and extent of coronary artery disease, including non-calcified and high-risk coronary plaques, that were associated with an increase in indicators of systemic immune activation (Foldyna et al., 2018; Tarr et al., 2018). In a previous work, increased myocardial inflammation has been described in HIV+ patients (Luetkens et al., 2019). Specifically in an interesting prospective study, Luetkens et al. that compared the results of comprehensive CMR studies in HIV+ asymptomatic patients and controls and observed an increase in CMR markers of myocardial inflammation in the HIV+ group, thus suggesting the presence of subclinical myocardial inflammation in this population, which may in the end lead to the impairment of left ventricular myocardial function. The major limitation of the cited study, as well as of our present study, is that no histological assessment has been carried out. Luetkens et al. suggested that, although direct HIV infection of myocytes is rare, it is possible that HIV itself together with other cardiotropic viral infections may lead to myocarditis and to a subsequent left ventricular dysfunction; this may also explain the high rate, observed among this population, of resting ECG abnormalities that are consistent with myocardial damage. Authors suggested that inflammatory condition and subsequent fibrosis may be responsible of the observed CMR findings. On the other hand, our results show relevant differences in respect to those of Luetkens et al.. Firstly, the statistical evaluation carried out by our colleagues is mainly descriptive and no regression analysis was performed due of the limited sample size. Moreover, since the study was conceived for preliminary investigation purposes, no correction analysis was performed, possibly leading to inflated type I errors. This assumption in our work is supported by a significant difference in ECV values between the different patient groups, which are known to represent an indirect measure of diffuse interstitial myocardial fibrosis or most serious heart diseases (Friedrich et al., 1998). In addition, the ECV values observed in our study were consistent with previous studies conducted in the HIV- population (Wiesmann et al., 2004). Lastly, in our study, due to a larger sample size, we were able to perform a multivariate regression analysis. It has been described previously that amyloid precursor protein (APP) may be an innate antiviral defence factor in macrophages and microglia that restricts HIV-1 release in the neurological environment. Highly expressed in macrophages and microglia, the membrane-associated APP binds the HIV-1 Gag polyprotein and blocks HIV-1 production and spread. To escape this restriction, Gag promotes secretase-dependent cleavage of APP, resulting in the overproduction of toxic Aβ isoforms. From a neuro-physiopathological point of view, this Gag-mediated Aβ production results in increased degeneration of primary cortical neurons. One interesting question is: could this mechanism be involved in the physiopathology of our findings of an increase in ECV? Could amyloid formation as a result of immunological response to virus in cardiovascular tissue explain cardiomyopathy and peripheral obstructive vascular lesions observed in HIV+ patients? Urgent studies are clearly needed to

better understand the complex dynamic that underlies the multiple peculiar features which are increasingly being observed in people chronically living with HIV, in order to design effective prevention strategies to counteract the increasing burden of cardiovascular events in our patients. Overall, these data suggest that an increase in systemic inflammation and immune activation may manifest as a premature CVD phenotype, including disease in large and small vascular beds in patients with HIV. Among PLWH, a relevant concern is whether scores that rely on traditional CV risk factors can accurately identify those individuals with a higher probability to develop CVD (d'Ettorre et al., 2016). In this study, we highlight that PLWH with low-ASCVD risk score are likely to suffer from a silent cardiac impairment. In fact, we found a significant difference in ECV levels between PLWH and healthy subjects (p-value$<$0.001), indicating the presence of ECM expansion in patients with HIV infection. More importantly, years of exposure to HIV, and years of antiretroviral therapy significantly correlated with ECV expansion. Quantification of ECM is an indirect measure of the expansion of extracellular matrix since, in absence of confounding conditions (e.g. oedema or amyloid), it is related to collagen excess in the interstitium. ECM expansion may therefore indicate vulnerable myocardium in PLWH and represent a potential therapeutic target (Shah et al., 2018). Indeed, abnormal fibrosis may be the underlying pathological finding in many cardiovascular disorders, particularly in Sudden Cardiac Deaths (SCD), an emerging issue in PLWH. Frieberg et al. report that PLWH had a 14% higher risk of SCD, with uncontrolled HIV infection representing a risk factor. Recently, a review of the health records from San Francisco between 2011 and 2016 outlined that the cause of death for autopsy-defined Sudden Arrhythmic Death Syndrome (SAD) and SCD were 83% and 82% higher respectively in the PLWH than in general population. Interestingly, the histologic exam identified higher rates of cardiac fibrosis in PLWH underling the excess risk of SAD. Indeed, specific tools are sought to measure in vivo the CV risk excess of PLWH which cannot be determined by common predictors of CV scores. Quantifying ECM expansion through ECV assessment may ultimately provide a basis to improve care in HIV individuals through a better risk stratification and the possibility of targeted treatment.

This study investigated the role of ECV measurements in the phenotypic characterization of CV risk, demonstrating that ECV can be easily and non-invasively assessed by CT-scan and used to characterize myocardial stiffness, a clear advantage with respect to alternative methodologies (Wessels et al., 2004). ECV could provide an important imaging tool to further understand the relationship between cardiac anatomy and heart function. HIV-positive subjects present ECV expansion in the myocardium. The duration of therapy and years of HIV infection are predictors of myocardial ECV expansion. Imaging technique in PLWH may be critical to identify patients with subclinical CVD and at risk for increased SCD and SAD events, where traditional risk scores may be inaccurate. Our data show that the measurement of ECV is a promising approach to identify asymptomatic patients with high risk of CV diseases despite a low-ASCVD traditional score risk prediction. Our findings, therefore, may help to explain the increased cardiac morbidity and mortality observed in patients with chronic HIV infection.

Part III

PROSPECTIVE, DISCUSSION AND CONCLUSION

Chapter 7

ECV in Clinical Practice from Research Tool to Clinical Application

This study contributes to our understanding about the role of ECV measurements in the phenotypic characterization of cardiologic risk and demonstrates that ECV measured by CT-scan can be used to evaluate myocardial stiffness, a metric that could only be assessed by high-fidelity invasive measurements. There is a growing body of published data suggesting that ECV provides novel information in diabetic patients and ultimately could guide selection of patients for novel-anti-fibrotic therapies. ECV could provide an important non-invasive imaging tool for further understanding the relationship between form and cardiac function. Imaging of CVD phenotypes in HIV may play an especially critical role to identify patients with subclinical CVD, at risk for increased SCD and SAD events, where traditional risk scores may be inaccurate. Our data show that the measurement of ECV may be a useful approach for identifying asymptomatic patients with high risk of SAD and/or SCD.
For clinical utilization, there needs to be standardized protocols in place for performing ECV. Furthermore, we need to employ this technique to better diagnose and understand disease processes and the effect of treatment on ECV (for example as a surrogate end point in drug trials). This has been implemented in the T_1 mapping consensus statement. For ECV to become a technique used in clinical practice, key steps need to be implemented—similar to developments in the CMR community, in particular standardization with phantom work, multicentre clinical data in health and disease, a consensus statement by national/international organizations and adoption by all major manufacturers.

The potential for ECV_{CT} and ECV_{CMR} extends beyond the myocardium. In chapter 5 we used CT to estimate ECV to validate measurements. This study is the first to propose the creation and use of test objects dedicated to validation measures for ECV in MR and CT applications, but the error affecting experimental estimation of ECV_{ref} are difficult to quantify due to some limitations, mainly:

1. use of non-certified materials, for which only the nominal density (or the

density range) is known; and

2. the vials containing the materials were filled with water or CA solution and subsequently closed, creating percolation processes and air bubbles trapping.

This study confirmed that the ECV determination is technically feasible also as part of a conventional pre- and post-contrast CT examination, without extra amount of CA and at a standard exposure level.
In recent years, some studies showed that the ECV fraction can also be evaluated with CT (Graser et al., 2009; Hong et al., 2016). ECV imaging by CT lags the MR field but is potentially an attractive alternative. Though the evidence base for ECV in MR may be larger and experience greater (above all, in cardiology examinations), the use of CT could present some advantages. In CT, ECV measures the direct effect of iodine-based contrast agents on the measured signal (through the effect of iodine on x-ray absorption), whereas ECV in MR relies on measuring the effect of CAs on protons, therefore making two assumptions: i. the relaxivity of tissues compared to blood is the same, and ii. water is rapidly exchanged between intra- and extracellular compartments. Also, common contraindications to MR such as claustrophobia and pacemaker implantation (the latter being not uncommon, for example in patients with cardiac amyloid where ECV quantification could prove helpful) do not apply for CT. Other authors used also dual-energy CT to quantify myocardial ECV, which is attractive, in principle, as it would potentially avoid mis-registration errors associated with the separate pre- and post-contrast scans, by obviating the need for the pre-contrast scan (Graser et al., 2009; Hong et al., 2016). On the other side, CT examinations imply the patient exposure to ionising radiations, differently from MR.

The second part of this work focused on ECV quantification in some clinical applications. In the context of heart disease, myocardial ECV values obtained in normal subjects (range: 23%-30%) were in a good agreement with previous studies, reporting values between 22%-34%. Also, for the diseased subjects examined here, the ECV median value was 34.2% (IQR: 31%-54%), in a good agreement with the values reported by previous studies (Borrazzo et al., 2019). The ROC analysis was performed to investigate on the ECV predictive value to distinguish between healthy and disease patients, obtaining an optimum threshold of 28.4%, corresponding to an excellent sensitivity (92%) and a good specificity (88.9%). This threshold value could be tentatively assumed for clinical studies. ECV optimum threshold for myocardial disease obtained here was in a good agreement with previous studies (threshold value: 28%-30%) (Chen et al., 2019). Considering disease patients as a whole dataset, the wide variability of data reflects the heterogeneity in clinical conditions, but some data stratification appears differentiating data among pathologies and according to the number of cases, also in a substantial agreement with the literature (Scully et al., 2018). In the second example of application, CEMRI data of patients with diagnosed brain tumors were retrospectively reviewed. After estimation of ECV values with the methodology proposed in this work, the obtained results were also compared with those obtained from MR perfusion images (also available for the three patients here considered), analysing data with the Tofts model (Borrazzo et al., 2018), obtaining

a good agreement (within 10%, data not shown). The obtained ECV values were also in a good agreement with a previous study concerning paediatric patients (38 patients; range: 19%-26%; methodology: Tofts model) (Vajapeyam et al., 2017), but at the same time another recent study reports significantly different values (83 adult patients; range: 6%-21%; methodology: Tofts model.) (Conte et al., 2019), thus highlighting the need for further studies in this area.
In the third example of application, the ECV for the spongiosa volume of thoracic vertebrae was derived from images and assumed as RM ECV. These data are of interest for RM dosimetry in radioimmunotherapy, or when large carrier molecules are used in a nonmyeloablative setting. When a slow clearance is involved (e.g., antibodies), the RM is the dose-limiting organ, so RM dosimetry should be performed to evaluate the treatment tolerability, considering a threshold value of absorbed dose of 2 Gy. RM dosimetry is usually performed by a two-compartment model (RM, i.e., self-irradiation, and remainder of body) (Sgouros, 1993). The self-irradiation contribution can be estimated by the "blood method", i.e., the radioactivity concentrations of blood samples is used to estimate that in RM, multiplying the blood radioactivity concentrations by the RMBLR, calculated as the ratio between patient-specific RMECFF and 1-HCT Wessels et al. (2004); Sgouros (1993). Individual quantification has never occurred so far, assuming a baseline value of 0.19 (derived from a study of rabbit femur). The possible use of both MR and CT for estimating the patient-specific RMECFF (i.e., the RM ECV) was here investigated, obtaining no significant differences between them. Considering the overall dataset, a mean ECV of 22% was obtained, which is in agreement with the traditional baseline value of 0.19, but a wide variability range of 13-32% was also observed. Even though the overall results in terms of RMBLR are in a good agreement with the range of 20-40% generally reported in the literature (see table 5.4 in the Results), the individual results evidence that the estimation of the absorbed dose to RM could lead to inaccuracies when just the baseline value of 0.19 is used. So far, a satisfactory correlation between RM dosimetry and adverse effects has never been highlighted in radioimmunotherapy with pure beta emitters, and this could be an indication of the importance of patient-specific RM ECV in dosimetric estimations. Currently, the characterisation of the spongiosa complex micro-anatomy is still an issue and ECV quantification could also be helpful. A further important result of this work is that ECV is easy to obtain also when examinations are not performed directly for this purpose, making possible also real-time ECV estimation. This PhD thesis work also paves the way to machine learning-related applications (Borrazzo et al., 2019).

Chapter 8

Novel CVD Risk Biomarkers in HIV

Recent studies have looked beyond traditional cardiovascular disease risk factors in an attempt to explain the excess cardiovascular disease risk observed in HIV. Among PLWH, an important concern is whether risk prediction algorithms that rely on traditional CV risk factors can accurately identify those individuals with a higher probability to develop CVD (Monroe et al., 2016). In the present thesis, we highlight that PLWH with low ASCVD risk score are likely to suffer from a silent cardiac impairment. In fact, we found a significant difference in ECV levels between PLWH and healthy subjects (p-value$<$0.001, chapter 6), indicating the presence of extracellular matrix expansion in the myocardium of patients with HIV infection. More importantly, years of exposure to HIV (r=0.54, p-value$<$0.001), and years of antiretroviral therapy (r=0.62, p-value$<$0.001) significantly correlate with myocardial ECV expansion. The quantification of Myocardial Extracellular Matrix (ECM) is considered as an indirect measure of cardiac fibrosis since it is related, in the absence of confounding conditions (e.g. oedema or amyloid), to the accumulation of excess collagen in the interstitium (Tarr et al., 2018). ECM expansion may therefore indicate vulnerable myocardium in PLWH and represents a potential therapeutic target (Hinderer and Schenke-Layland, 2019; Bacmeister et al., 2019; González et al., 2020).

Abnormal fibrosis may be the underlying pathological finding in many cardiovascular disorders: in particular, in Sudden Cardiac Death (SCD), which represents an emerging issue in PLWH. Freiberg and So-Armah (2016) report that PLWH had a 14% higher risk of SCD with uncontrolled HIV infection representing a risk factor (González et al., 2020). Recently, a review of the health records in San Francisco between 2011 and 2016 evidenced that the cause of death for autopsy-defined sudden arrhythmic death syndrome (SAD) and SCD were 83% and 82% higher respectively in the PLWH than in general population. Interestingly, the histologic exam identified higher rates of cardiac fibrosis in PLWH underling the excess risk of SAD (Tseng, 2019). Indeed, there is the need for specific tools to assess in vivo the excess CV risk of PLWH that is not estimated by common predictors of CV risk.

Quantifying ECM expansion through ECV evaluation may ultimately provide a basis to improve care in HIV+ individuals through a better risk stratification and

the possibility of a targeted treatment. Future studies should identify appropriate screening and risk assessment tools and protocols for the primary and secondary management of this unique population. T_1 and ECV mapping provide new opportunities to understand myocardial disease. T_1 is sensitive to myocardial processes that affect the myocardium globally and in different way as we can see from figure 8.1.

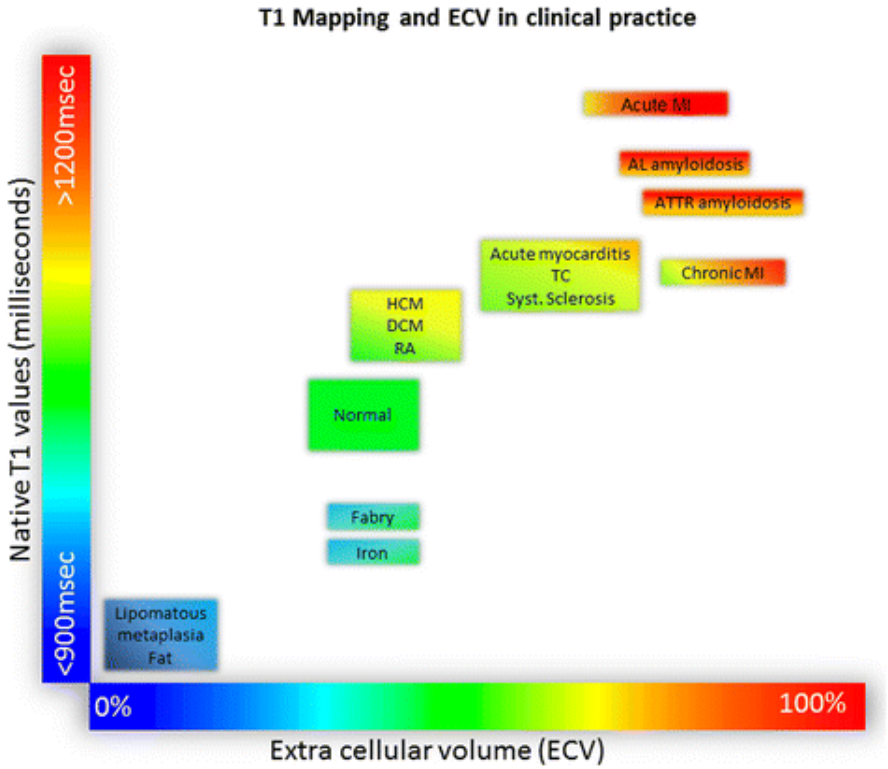

Figure 8.1. Schematic diagram for focal and global myocardial tissue characterization using native T_1 measured in milliseconds, and the extracellular volume fraction (ECV) measured in percent. Absolute cutoff values defining normality for native T_1 may vary depending on the exact sequence used for T1-mapping. From Haaf et al. (2017).

Conversely, ECV detects abnormalities limited to expansion of the extracellular compartment, typically fibrosis but also amyloidosis and edema (depending on the clinical context). Emerging work suggests that T_1 mapping and ECV mapping have the potential to improve the diagnosis of disease including the importance of disease. CT and MR can be used to estimate ECV without the need of invasive biopsy. Each modality has strengths and weaknesses, with CT resulting as an attractive alternative to MR, particularly when contraindications to the MR are present. Accuracy improvements and uncertainty estimation for ECV obtained from images are currently under investigation. Additional investigations would be also required for other clinical application, as the literature reports conflicting data. However, the results obtained in this work from patient studies are mostly in a very good agreement with those reported in the literature, confirming that the ECV estimation from clinical examination is promising and easy to obtain also when examinations are not performed directly for this purpose.

Chapter 9

Discussion and conclusion

This chapter concludes the thesis with a discussion of the main results and conclusions, and sets out the areas that require development in the future. This thesis contributes to the understanding of the role of ECV measurements in the phenotypic characterization of CV risk, suggests that ECV can be easily measured by CT-scan and used to characterize myocardial stiffness. Alternative methodologies to assess the same metric with good accuracy unfortunately are too invasive. A growing body of published data suggests that ECV provides novel information in HIV+ patients and ultimately could guide selection of patients for novel therapies.

In this work several aspects of the ECV mapping technique are developed, from image acquisitions to image anaysis and post processing. In fact, as reported in the chapter 4 we obtained in our scanner a robust and valid acquisition protocol. Furthermore, we developed an automatic software for ECV mapping images post-processing from motion correction to ECV mapping (chapter 4). Our starting point is the image acquisitions. Sequence protocol has been optimized and tested on our scanner to avoid several confoundig factors. We obtained an accuracy and reproducibility in line with literature (Kellman et al., 2012), in particular an accuracy lower than 10% for the whole range of investigated T_1 and an highly significant degree of reproducibility. Regarding image acquisitions, we have seen that a number of factors influence the accuracy of T_1 mapping technique through the MOLLI sequence. If these factors, which may depend on the protocol or scanner adjustments, are not well controlled, then they can contribute to reduced reproducibility and accuracy. Hence we can conclude that T_1 might become a powerful clinical tool despite the fact that the measurement may not be fully accurate.

The results of chapter 5 are related to MRI and CT techniques compared for the quantification of ECV. This study is the first to propose the creation and use of test objects dedicated to validation measures for ECV in MR and CT applications. The second part of this chapter 5 focused on ECV quantification in some clinical applications. In the context of heart disease, myocardial ECV values obtained in normal subjects (range: 23%-30%) were in a good agreement with previous studies, reporting values between 22%-34%. In the second example of application, CEMRI data of patients with diagnosed brain tumors were retrospectively reviewed. After estimation of ECV values with the methodology proposed in this work, the obtained results were also compared with those obtained from MR perfusion images (also

available for the three patients here considered), analysing data with the Tofts model (Borrazzo et al., 2018), obtaining a good agreement (within 10%, see section 5.3.2). In the third example of application, the ECV for the spongiosa volume of thoracic vertebrae was derived from images and assumed as RM ECV. These data are of interest for RM dosimetry in radioimmunotherapy, or when large carrier molecules are used in a nonmyeloablative setting. When a slow clearance is involved (e.g., antibodies), the RM is the dose-limiting organ, so RM dosimetry should be performed to evaluate the treatment tolerability, considering a threshold value of absorbed dose of 2 Gy.

In chapter 6 we have shown promising results regarding the measurement of ECV in asymptomatic HIV+ patients. ECV could provide an important non-invasive imaging tool to further understand the relationship between cardiac anatomy and heart function. Imaging technique in PLWH may play a critical role to identify patients with subclinical CVD and at risk for increased SCD and SAD events, when traditional risk scores may be inaccurate (Ceccarelli et al., 2013; Monroe et al., 2016). In conclusion, our data show that the measurement of ECV may be a promising approach for identifying asymptomatic patients with high risk of CV diseases despite a low ASCVD risk prediction.

This thesis work has largely focused on technical development of the equilibrium technique with early comparison of ECV with other markers of disease. Because of the observational and cutting edge design of this study, our approach has several limitations. Some limitations of this work have been the retrospective use of cohorts for additional analyses, introducing experimental constraints. Within this development, importantly evaluation of ECV measurement precision has been omitted, with no incorporation of repeatability or reproducibility assessment steps. Before proposing use of ECV as a diagnostic tool, these attributes, including intra and inter user variation, and variation between scanners, vendors and locations must be evaluated. Biomarker reference ranges, test sensitivity and specificity, and linkage to clinical outcomes can then be defined. This work will form the basis of the next phase of imaging development. It is my hope that future work will continue development of this technique towards a robust non-invasive test, with real clinical utility.

Appendix A

MRI and CT physics principles

A.1 Image formation

Magnetic resonance imaging (MRI) is a process involving the absorption and emission of energy by nuclei, mainly the hydrogen protons in human body, as a diagnostic tool. In 1946, Felix Bloch described nuclear MR phenomenon with a set of equations assuming that the ensemble of spins could be represented as a net nuclear magnetization ($\vec{M}$) (Bloch, 1946). These spins behave according to the laws of classical electromagnetism. If the spins that contribute to $\vec{M}$ interact only with an external magnetic field ($\vec{B}$), they will experience a torque given by the vector cross product $M\vec{O}\vec{B}$. Because the torque of a system is equal to the time rate of change of its angular momentum, Bloch described the motion of $\vec{M}$ as a precession around $\vec{B}$:

$$\frac{d\vec{M}}{dt} = \gamma[\vec{M} \times \vec{B}] \tag{A.1}$$

where γ represents the gyromagnetic ratio that is, for hydrogen nuclei, $2.68 \cdot 10^8 T^{-1} s^{-1}$ or $\gamma/2\pi = 42.7 MHz/T$. The precession motion of $\{vecM$ around the magnetic field $\vec{B}$ is shown in figure A.1. When the spin system is stimulated by a radiofrequency near proton Larmor frequency, spins will try to recover to the the equilibrium magnetization M0 therefore $\vec{M}$ will not simply precess indefinitely around $\vec{B}$.

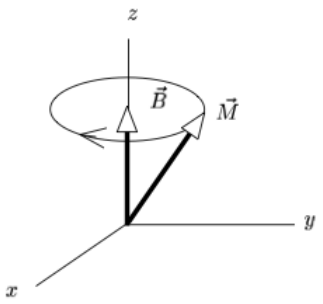

Figure A.1. The precession motion of $\vec{M}$ around the magnetic field $\vec{B}$.

During this recovery to the equilibrium state, spins interact with each other and with the external environment releasing their energy to the environment or each other. Bloch called this phenomenon relaxation and introduced two time constants (T1 and T2) to account for the reestablishment of the thermal equilibrium of the nuclear magnetization following a radiofrequency pulse. More in details we have:

i) Spin-Lattice or T1 relaxation: T1 relaxation causes the magnetization to return to alignment with the $\vec{B}$ in the z-direction. The cause of T1 relaxation is the transfert of spin energy to the environment (or "lattice").

ii) Spin-Spin or T2 relaxation: T2 relaxation causes the nuclei to lose phase with each other. This loss of choerence is caused by the individual nuclear spins exchanging energy with each other. The effect is to cause the transverse magnetization, the sum of all the spins, to decay.

For the purpose of this dissertation , we focus mainly on T1 relaxation, so we are interesting in the z component of magnetization. In fact T1 describes how fast the longitudinal magnetization (Mz) recovers to its equilibrium M0. By adding the T1 effect to the original equation A.2, in absence of any radiofrequency pulse, or other effects (such as magnetization transfer or perfusion), the recovery of longitudinal magnetization is described by the Bloch Equation (Bloch, 1946):

$$\frac{d\vec{M}_z}{dt} = \frac{M_0 - M_z}{T_1} \tag{A.2}$$

The solution of the equation A.2 is

$$\vec{M}_z(t) = M_z(0)e^{-\frac{t}{T1}} + M_0(1 - e^{-\frac{t}{T1}}) \tag{A.3}$$

The recovery curve of longitudinal magnetization is shown in figure A.2.

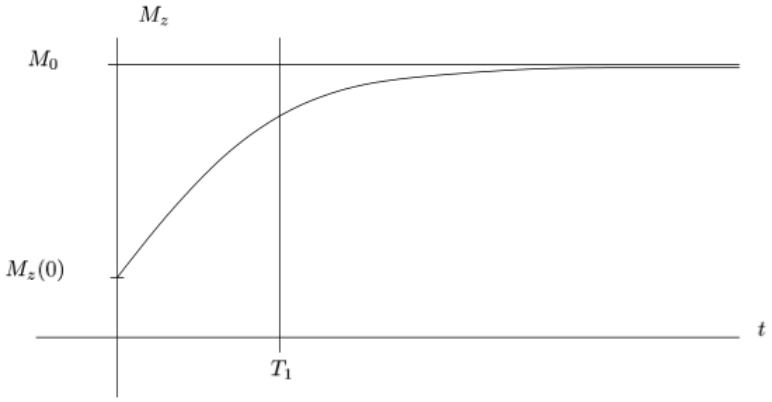

Figure A.2. The recovery curve of longitudinal magnetization.

Therefore the T1 recovery rate can tell us about the mobility of the molecules and hence the binding of water molecules, for instance to macromolecules. Typical T1 relaxation times for water protons in biological samples are 500 ms to 2000 ms,

with 1000 ms being typical for many tissues. T1 is an intrinsic biophysical property of the tissue, and the accurate measurement of T1 is important not only for tissue characterization, but also for contrast agent uptake studies, and measurement of perfusion and blood volume. In fact the effect of contrast agents in MR studies is to differently affect T1 values of different tissues in order to locally change contrast image.

T2 relaxation refers to the processes that bring the transverse magnetization M_{xy} back to its value at the equilibrium state, i.e., zero. T2 relaxation relates to the incoherent exchange of energy among neighboring spins. Because of this it is called spin-spin relaxation. T2 relaxation is generally exponential and described by the equation:

$$\frac{d\vec{M_{xy}}}{dt} = \frac{M_{xy}}{T_2} \tag{A.4}$$

The process of T2 relaxation reflects the dephasing of the transverse magnetization from the different nuclei after the RF pulse. The dephasing occurs due to local magnetic field inhomogeneities in the net main field. Ideally the main field should be B0 for all nuclei, which will also mean that all spins will have the same precession frequency for their transverse magnetization, namely $\omega_0 = \gamma B0$. However, there will be fluctuations in the longitudinal component of the local main field, and consequently in the resonance frequencies. These fluctuations occur due to both magnetic interactions between the nuclei and imperfections in the main field homogeneity. If the spins have slightly different resonance frequencies it means that, after the RF pulse, the transverse magnetization of some spins will precess faster (where the net field B > B0), whereas for other spins the precession will be slower (where the net field B < B0). We can visualize the effect of this in the rotating coordinate system: the magnitude of the net transverse magnetization vector will get smaller with time as the individual components from different spins get out of phase from each other. Relaxation properties of tissue are of primary importance in magnetic resonance imaging because T1 and T2 are at the basis of contrast in medical imaging. Typical values of native T1 values of myocardium are reported in figure A.3.

A.2 Myocardial T1 mapping techniques

Several T1 mapping techniques are available in order to obtain the true T1 of the tissues. In particular the most widely available T1 mapping methods are based on two different types of pre pulses: inversion recovery pulse and saturation recovery pulse. Pre pulse is necessary in order to move magnetization from the $\vec{B_0}$ direction and then to inizialize the recovery of longitudinal magnetization. In this framework myocardium represents a challenge for this type of measurements because of heart beat and breath.

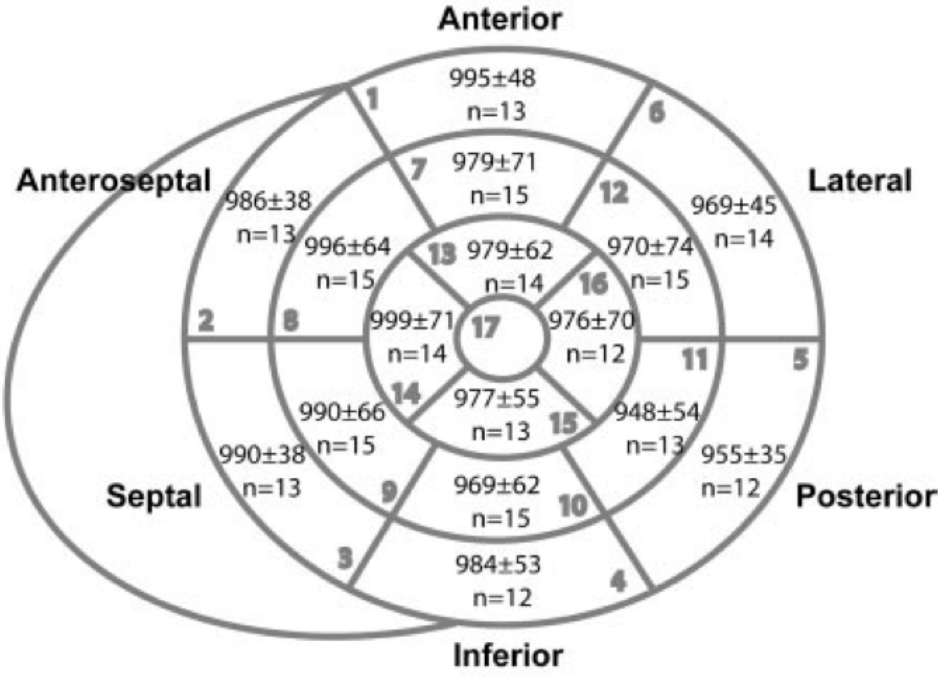

Figure A.3. Distribution of baseline segmental T1 values (in ms) in left ventricular myocardium from Messroghli et al. (2006). Values are reported as mean ± standard deviation.

A.3 Modified Look Locker (MOLLI) sequence

The Modified Look Locker inversion recovery sequence is a 2D sequence that allows the acquisition of single shot balanced Steady State Free Precession, bSSFP (or TrueFISP on Siemens scanners) images acquired at different inversion times after a single inversion pulse, all gated to the same cardiac phase, thereby enabling a pixel-based T1 quantification in the myocardium. The detailed overview of the bSSFP acquisitions will be dealt with in the next paragraph A.4. The sequence was developed by Messroghli et al. (2007) in order to overcome the limitations of Look Loker sequence in cardiac applications. After the inversion, the magnetization following the T1 relaxation curve is repetitively sampled in several heartbeats for a small duration until the longitudinal magnetization has fully recovered. By combining several (up to 3) inversions with slightly shifted TI times within one protocol, the relaxation curve is sampled in an interleaved manner, resulting in a sufficient number of points for accurate T1 quantification acquired within a single breath-hold as we can see in figure A.4.

The original protocol of MOLLI sequence shown in figure A.4 is called 3(3)3(3)5 because three images are acquired after the first inversion pulse, then a three cardiac cycle pause is taken before the second inversion pulse, other three images are recorded and then, after a pause of three cardiac cycles, the third inversion pulse is followed by the acquisition of five images. In the scheme name (i.e. 3(3)3(3)5), the numbers out of brackets refers to the number of images acquired after an inversion pulse, the

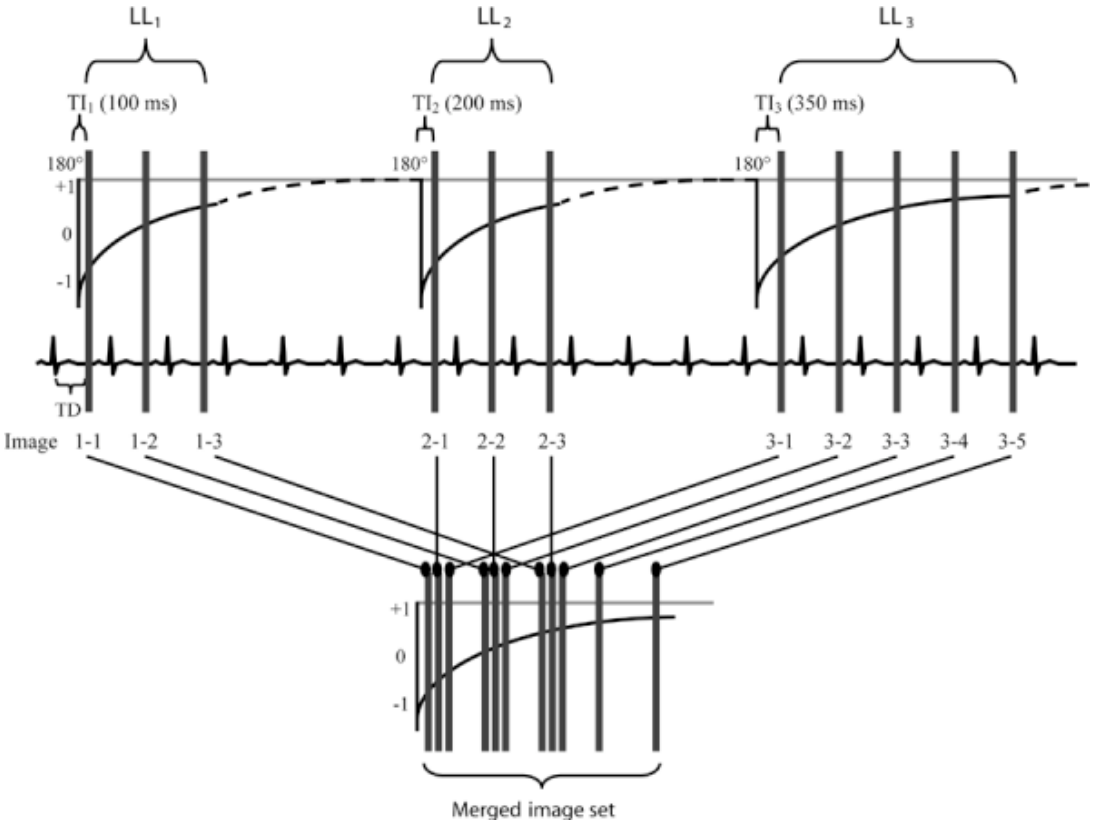

Figure A.4. MOLLI pulse sequence scheme. There are three Look-Locker (LL) experiments, each prepared by a separate 180° inversion pulse (I_p). The Inversion Time (TI) of the first LL experiment is defined as $TI_{minimum}$. TI of the second and third LL experiment are determined by $TI_{minimum} + TI_{increment}$ and $TI_{minimum} + 2 \cdot TI_{increment}$, respectively. After the inversion pulses, images are read out with a constant flip angle. There is a defined number of pausing heart cycles in between LL experiments in order to allow for undisturbed signal recovery. From Messroghli et al. (2007).

numbers in brackets refers to the numbers of cardiac cycles waited before the next inversion pulse (Messroghli et al., 2007). Other combinations in terms of number of acquired images and pauses are possible. Some important parameters to set in sequence are $TI_{minimum}$, $TI_{increment}$, the inversion numbers, the number of images acquired after each inversion and the number of pause phase cycles before the next inversion. Several papers considered different MOLLI scheme in terms of accuracy, precision and time of acquisition (Kellman and Hansen, 2014). Infact the original sequence scheme in figure A.4 lasts 17 heartbeats. This means about 17 s for subjects with a regular 60 bpm heartbeat. As the sequence is breath-hold, it could be difficult to use it with subjects affected by particular pathologies. For this reason other sequence schemes were developed to obtain good accuracy and precision but with lower scanning time. We chose to consider and optimize two different sequence schemes for pre and post contrast acquisitions: the protocol 5(3)3 that consists in 2 inversions with 5 images after the first inversion, 3 hearts beat of pause and then other 3 images were acquired and the protocol 4(1)3(1)2 that consists in the acquisition of four images after the first inversion pulse, one heart beat of pause for

the complete recovery of magnetization, then other 3 images where acquired, again one heart beat pause and then the last 2 images acquired after the third inversion pulse. We used two different MOLLI sequence scheme because it is well know that the first one lead to more accuracy in T1 measurement in tissue with high values of T1 (as for native myocardial T1); while the second scheme is more accurate in low T1 determination (as in post contrast images) (Kellman and Hansen, 2014).

A.4 The extracellular volume fraction

In chapter 3 the meaning and clinical relevance of the extracellular volume fraction were explained. Here we focus on the theory necessary to calculate this important output from pre and post contrast T1 maps. Taking the reciprocal of pre and post contrast T1 values we can define ΔR_1 as:

$$\Delta R_1 = \frac{1}{T_{1,post}} - \frac{1}{T_{1,pre}} \tag{A.5}$$

This value is proportional to contrast agent concentration:

$$\Delta R_1 = r_1 \cdot [CA] \tag{A.6}$$

where r_1 is a constant representing the T1-relaxivity of the given contrast agent and $[CA]$ is the concentration of that contrast agent. If the ratio of the contrast agent concentration between two tissues is in equilibrium or in dynamic equilibrium, then the contrast agent concentration ratio is equal to the ΔR_1 ratio of these tissues since r1 is a constant which calls off. For myocardium and blood then we have (Ugander et al., 2012):

$$\frac{\Delta R_{1,myo}}{\Delta R_{1,blood}} = \frac{[CA]_{myo}}{[CA]_{blood}} \tag{A.7}$$

where $\Delta R_{1,myo}$ is the ΔR_1 for myocardium, $\Delta R_{1,blood}$ is the ΔR_1 for blood, $[CA]_{myo}$ is the contrast agent concentration in the myocardium and $[CA]_{blood}$ is the contrast agent concentration in the blood. Gadolinium (Gd) chelates, such as Gd-DTPA, are extracellular agents because they freely pass across the vascular wall into the extracellular space but are excluded from the intracellular space. Using this type of contrast agents, the ratio of contrast agent concentrations between myocardium and blood equals the ratio of extracellular volume between the tissues:

$$\frac{[CA]_{myo}}{[CA]_{blood}} = \frac{ECV_{myo}}{ECV_{blood}} \tag{A.8}$$

where ECV_{myo} is the extracellular volume fraction (ECV) of the myocardium and ECV_{blood} is the ECV of the blood. The ECV is defined as the fraction of a given tissue which is comprised of extracellular space (range 0-100%). The ECV of the blood is defined as the fraction of the blood volume which is not composed of blood cells, in other words, the fraction composed of plasma. The plasma volume fraction can be measured as one minus hematocrit because hematocrit represents the percentage of corpuscular part in blood:

$$ECV_{blood} = 1 - HCT. \tag{A.9}$$

By combining equations A.7, A.8 and A.9 and solving for the ECV of the myocardium:

$$ECV_{myo}(\%) = (1 - HCT) \cdot \frac{\Delta R_{1,myo}}{\Delta R_{1,blood}} \cdot 100 \tag{A.10}$$

To obtain accurate ECV measurements, the measurement of T1 must be accurate in both myocardium and blood, both before and after contrast. Furthermore, the measurements are only valid for tissues where contrast agent concentration is in an equilibrium (steady state) or a dynamic equilibrium (dynamic steady state) with the contrast agent concentration in the blood pool. Following an intravenous injection, contrast agents such as Gd-DTPA are continuously cleared from the blood via renal clearance. Thus, after an initial period of equilibration, the contrast agent concentration in the blood will steadily decrease over time. However, if the contrast exchange rate between blood and the tissue of interest is faster than the renal clearance, then the ratio of contrast agent concentration between tissue and blood will, after the short initial equilibration period, achieve a dynamic equilibrium and remain unchanged over time (Arheden et al., 1999). As we can see from the formula A.10, we need to know the T1 value in the myocardium to obtain the ECV value. This can be done drawing a region of interest (ROI) in the myocardium and in the blood pool of the native and pre-contrast T1 map. In this way it is possible to know only the local ECV value, but not the extent and severity of ECV alterations. ECV mapping has the aim of deriving the extracellular volume fraction map in the whole myocardium. To do this, we need to calculate $\Delta R_{1,myo}$ on a pixel-by-pixel basis as the reciprocal of the T1 maps. The extracelluar volume calculated from T1 values positively correlated with histological analysis, which can help to guide the decision-making regarding when to send patients for invasive surgery and follow changes of fibrosis in the myocardium over time with noninvasive assessment.

A.5 Equilibrium contrast imaging CT

Soon after Roentgen discovered the X-ray, scientists appreciated the need for extraneous agents to improve radiographic soft tissue contrast. In 1896 Sehrwald compared the properties of in-vitro halogens (e.g. iodine and bromide) with other metal salts and organic compounds, before Haschek and Lindenthal administered a paste of mercury sulphide and lime into the blood vessels of an amputated hand to produce the first contrast angiogram.
Todays contrast agents are stable, inert, water (but not fat) soluble molecules, with negligible protein binding; Iohexol contains organically bound iodine and has been used widely in medical imaging for the past 30 years. Both iodinated and gadolinium based agents are extracellular tracers which when administered into the blood, circulate in the plasma and move passively into the tissue interstitium without crossing intact cell membranes, before being excreted by the kidneys. Their various vascular and interstitial phases provide exquisite soft tissue contrast and markedly enhance diagnostic performance when used. The CT protocol consisted of three steps

(Figure A.5 for flow chart): first, a CT scan to obtain baseline pre-contrast blood and myocardial attenuation in Hounsfield units (HU); second, contrast administration and delay so the contrast distributes into a blood:myocardial dynamic equilibration; third, a repeat scan to re-measure blood and myocardial attenuation. The ratio of the change in blood and myocardial attenuation (ΔHU) represents the contrast agent partition coefficient.

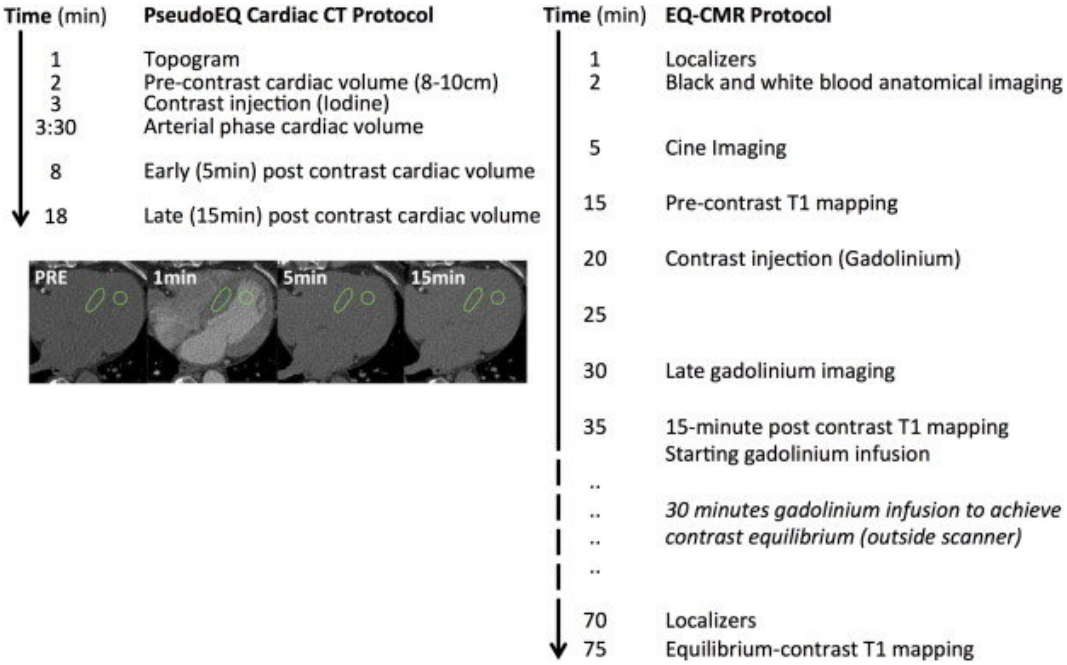

Figure A.5. Cardiac CT and CMR Protocols: CMR was performed either after or at least 24 hours prior to the CT to avoid residual gadolinium causing an increase in measured attenuation (from Treibel et al. 2014).

A.6 Extracellular volume fraction in Tomography

ECV (%) and post-contrast Hounsfield unit (HU) were measured on a PACS system. The same image, with MR short axis mid–left ventricle (LV) where the papillary muscles were visible, was chosen from the 13-min iodine map and post-contrast image. The regions of interest (ROI) were drawn at the septal segment, and a round ROI ($10mm^2$) that avoided the papillary muscle was drawn in the LV cavity (Figure 2A). The mean attenuation at the ROI was recorded in HU. Myocardial CT ECV (ECV_{myo}) was calculated using the following formula (Equation A.1):

$$ECV_{myo}(\%) = (1 - HCT) \cdot \frac{\Delta HU_{myo}}{\Delta HU_{blood}} \cdot 100 \tag{A.11}$$

where ECVm is myocardial ECV in dual-energy CT, HU_{myo} is HU corresponding to the myocardium ROI on the iodine map, and HU_{blood} is HU corresponding to the blood pool on the iodine map.

Appendix B

Proposal

- Progetti Medi anno 2018, Sapienza:assegnazione finanziamento di Euro 10.000 per la ricerca dal titolo Plasmonic photo-thermal ablation of cancer cells with radiopharmaceutical labeled gold nanoparticles - n. protocollo RM11816431206A2C.

Bibliography

Agatston, A. S., Janowitz, W. R., Hildner, F. J., Zusmer, N. R., Viamonte, M., and Detrano, R. "Quantification of coronary artery calcium using ultrafast computed tomography." *Journal of the American College of Cardiology*, 15(4):827–832 (1990).

Aime, S., Calabi, L., Biondi, L., De Miranda, M., Ghelli, S., Paleari, L., Rebaudengo, C., and Terreno, E. "Iopamidol: Exploring the potential use of a well-established x-ray contrast agent for MRI." *Magnetic Resonance in Medicine: An Official Journal of the International Society for Magnetic Resonance in Medicine*, 53(4):830–834 (2005).

Altabella, L., Borrazzo, C., Carnì, M., Galea, N., Francone, M., Fiorelli, A., Di Castro, E., Catalano, C., and Carbone, I. "A feasible and automatic free tool for T1 and ECV mapping." *Physica Medica*, 33:47–55 (2017).

Anderson, K., Sutton, M., and Lie, J. "Histopathological types of cardiac fibrosis in myocardial disease." *The Journal of pathology*, 128(2):79 (1979).

Andreu-Perez, J., Poon, C. C., Merrifield, R. D., Wong, S. T., and Yang, G.-Z. "Big data for health." *IEEE journal of biomedical and health informatics*, 19(4):1193–1208 (2015).

Arheden, H., Saeed, M., Higgins, C. B., Gao, D.-W., Bremerich, J., Wyttenbach, R., Dae, M. W., and Wendland, M. F. "Measurement of the distribution volume of gadopentetate dimeglumine at echo-planar MR imaging to quantify myocardial infarction: comparison with 99mTc-DTPA autoradiography in rats." *Radiology*, 211(3):698–708 (1999).

Bacmeister, L., Schwarzl, M., Warnke, S., Stoffers, B., Blankenberg, S., Westermann, D., and Lindner, D. "Inflammation and fibrosis in murine models of heart failure." *Basic research in cardiology*, 114(3):19 (2019).

Bandula, S., Banypersad, S., Sado, D., Taylor, S., Punwani, S., and Moon, J. "Measurement of tissue extracellular volume in health and amyloidosis using Equilibrium contrast MRI." (2017).

Bandula, S., White, S. K., Flett, A. S., Lawrence, D., Pugliese, F., Ashworth, M. T., Punwani, S., Taylor, S. A., and Moon, J. C. "Measurement of myocardial extracellular volume fraction by using equilibrium contrast-enhanced CT: validation against histologic findings." *Radiology*, 269(2):396–403 (2013).

Barral, J. K., Gudmundson, E., Stikov, N., Etezadi-Amoli, M., Stoica, P., and Nishimura, D. G. "A robust methodology for in vivo T1 mapping." *Magnetic resonance in medicine*, 64(4):1057–1067 (2010).

Bavinger, C., Bendavid, E., Niehaus, K., Olshen, R. A., Olkin, I., Sundaram, V., Wein, N., Holodniy, M., Hou, N., Owens, D. K., et al. "Risk of cardiovascular disease from antiretroviral therapy for HIV: a systematic review." *PloS one*, 8(3):e59551 (2013).

Becker, A., HEUMANS, C., and Essed, C. "Chronic non-ischaemic congestive heart disease and endoniyocardial biopsies. Worth the extra?" *European heart journal*, 12(2):218–223 (1991).

Bloch, F. "Nuclear induction." *Physical review*, 70(7-8):460 (1946).

Boccara, F., Lang, S., Meuleman, C., Ederhy, S., Mary-Krause, M., Costagliola, D., Capeau, J., and Cohen, A. "HIV and coronary heart disease: time for a better understanding." *Journal of the American College of Cardiology*, 61(5):511–523 (2013).

Borrazzo, C., Galea, N., Pacilio, M., Altabella, L., Preziosi, E., Carnì, M., Ciolina, F., Vullo, F., Francone, M., Catalano, C., et al. "Myocardial blood flow estimates from dynamic contrast-enhanced magnetic resonance imaging: three quantitative methods." *Physics in Medicine & Biology*, 63(3):035008 (2018).

Borrazzo, C., Pacilio, M., Galea, N., Preziosi, E., Carnì, M., Francone, M., Catalano, C., and Carbone, I. "T1 and extracellular volume fraction mapping in cardiac magnetic resonance: estimation of accuracy and precision of a novel algorithm." *Physics in Medicine & Biology*, 64(4):04NT06 (2019).

Cameron, D., Vassiliou, V. S., Higgins, D. M., and Gatehouse, P. D. "Towards accurate and precise T 1 and extracellular volume mapping in the myocardium: a guide to current pitfalls and their solutions." *Magnetic Resonance Materials in Physics, Biology and Medicine*, 31(1):143–163 (2018).

Ceccarelli, G., d'Ettorre, G., and Vullo, V. "The challenge of cardiovascular diseases in HIV-positive patients: it's time for redrawing the maps of cardiovascular risk?" *International journal of clinical practice*, 67(1):1–3 (2013).

Chen, Y., Zheng, X., Jin, H., Deng, S., Ren, D., Greiser, A., Fu, C., Gao, H., and Zeng, M. "Role of myocardial extracellular volume fraction measured with magnetic resonance imaging in the prediction of left ventricular functional outcome after revascularization of chronic total occlusion of coronary arteries." *Korean Journal of Radiology*, 20(1):83–93 (2019).

Constantine, G., Shan, K., Flamm, S. D., and Sivananthan, M. U. "Role of MRI in clinical cardiology." *The Lancet*, 363(9427):2162–2171 (2004).

Conte, G., Altabella, L., Castellano, A., Cuccarini, V., Bizzi, A., Grimaldi, M., Costa, A., Caulo, M., Falini, A., and Anzalone, N. "Comparison of T1 mapping and fixed T1 method for dynamic contrast-enhanced MRI perfusion in brain gliomas." *European radiology*, 29(7):3467–3479 (2019).

Dabir, D., Child, N., Kalra, A., Rogers, T., Gebker, R., Jabbour, A., Plein, S., Yu, C.-Y., Otton, J., Kidambi, A., et al. "Reference values for healthy human myocardium using a T1 mapping methodology: results from the International T1 Multicenter cardiovascular magnetic resonance study." *Journal of Cardiovascular Magnetic Resonance*, 16(1):1–12 (2014).

d'Ettorre, G., Ceccarelli, G., Pavone, P., Vittozzi, P., De Girolamo, G., Schietroma, I., Serafino, S., Giustini, N., and Vullo, V. "What happens to cardiovascular system behind the undetectable level of HIV viremia?" *AIDS research and therapy*, 13(1):21 (2016).

European Society of Cardiology, G. . "ESC guidelines 2019." 1(1):1–57 (2019).

Fauci, A. S. and Lane, H. C. "Human immunodeficiency virus (HIV) disease: AIDS and related disorders." *Harrisons Principles of Internal Medicine*, 2:1852–1912 (2001).

Fent, G. J., Garg, P., Foley, J. R., Swoboda, P. P., Dobson, L. E., Erhayiem, B., Treibel, T. A., Moon, J. C., Greenwood, J. P., and Plein, S. "Synthetic myocardial extracellular volume fraction." *JACC: Cardiovascular Imaging*, 10(11):1402–1404 (2017).

Flacke, S. J., Fischer, S. E., and Lorenz, C. H. "Measurement of the gadopentetate dimeglumine partition coefficient in human myocardium in vivo: normal distribution and elevation in acute and chronic infarction." *Radiology*, 218(3):703–710 (2001).

Flett, A. S., Hayward, M. P., Ashworth, M. T., Hansen, M. S., Taylor, A. M., Elliott, P. M., McGregor, C., and Moon, J. C. "Equilibrium contrast cardiovascular magnetic resonance for the measurement of diffuse myocardial fibrosis." *Circulation*, 122(2):138–144 (2010).

Foldyna, B., Fourman, L. T., Lu, M. T., Mueller, M. E., Szilveszter, B., Neilan, T. G., Ho, J. E., Burdo, T. H., Lau, E. S., Stone, L. A., et al. "Sex differences in subclinical coronary atherosclerotic plaque among individuals with HIV on antiretroviral therapy." *Journal of acquired immune deficiency syndromes (1999)*, 78(4):421 (2018).

Freiberg, M. S. and So-Armah, K. "HIV and cardiovascular disease: we need a mechanism, and we need a plan." (2016).

Friedrich, M. G., Strohm, O., Schulz-Menger, J., Marciniak, H., Luft, F. C., and Dietz, R. "Contrast media–enhanced magnetic resonance imaging visualizes myocardial changes in the course of viral myocarditis." *Circulation*, 97(18):1802–1809 (1998).

González, A., López, B., Ravassa, S., San José, G., and Díez, J. "Reprint of "The complex dynamics of myocardial interstitial fibrosis in heart failure. Focus on collagen cross-linking"." *Biochimica et Biophysica Acta (BBA)-Molecular Cell Research*, 1867(3):118521 (2020).

Graser, A., Johnson, T. R., Chandarana, H., and Macari, M. "Dual energy CT: preliminary observations and potential clinical applications in the abdomen." *European radiology*, 19(1):13 (2009).

Grunfeld, C., Delaney, J. A., Wanke, C., Currier, J. S., Scherzer, R., Biggs, M. L., Tien, P., Shlipak, M., Sidney, S., Polak, J. F., et al. "Pre-clinical atherosclerosis due to HIV infection: carotid intima-medial thickness measurements from the FRAM Study." *AIDS (London, England)*, 23(14):1841 (2009).

Guthaner, D. F., Miller, D. C., Silverman, J. F., Stinson, E. B., and Wexler, L. "Fate of the false lumen following surgical repair of aortic dissections: an angiographic study." *Radiology*, 133(1):1–8 (1979).

Haaf, P., Garg, P., Messroghli, D. R., Broadbent, D. A., Greenwood, J. P., and Plein, S. "Cardiac T1 mapping and extracellular volume (ECV) in clinical practice: a comprehensive review." *Journal of Cardiovascular Magnetic Resonance*, 18(1):1–12 (2017).

Hemkens, L. G. and Bucher, H. C. "HIV infection and cardiovascular disease." *European heart journal*, 35(21):1373–1381 (2014).

Hinderer, S. and Schenke-Layland, K. "Cardiac fibrosis–A short review of causes and therapeutic strategies." *Advanced drug delivery reviews*, 146:77–82 (2019).

Hong, Y. J., Kim, T. K., Hong, D., Park, C. H., Yoo, S. J., Wickum, M. E., Hur, J., Lee, H.-J., Kim, Y. J., Suh, Y. J., et al. "Myocardial characterization using dual-energy CT in doxorubicin-induced DCM: comparison with CMR T1-mapping and histology in a rabbit model." *JACC: Cardiovascular Imaging*, 9(7):836–845 (2016).

Hounsfield, G. N. "Computerized transverse axial scanning (tomography): Part 1. Description of system." *The British journal of radiology*, 46(552):1016–1022 (1973).

Hulten, E. A., Carbonaro, S., Petrillo, S. P., Mitchell, J. D., and Villines, T. C. "Prognostic value of cardiac computed tomography angiography: a systematic review and meta-analysis." *Journal of the American College of Cardiology*, 57(10):1237–1247 (2011).

Iles, L., Pfluger, H., Phrommintikul, A., Cherayath, J., Aksit, P., Gupta, S. N., Kaye, D. M., and Taylor, A. J. "Evaluation of diffuse myocardial fibrosis in heart failure with cardiac magnetic resonance contrast-enhanced T1 mapping." *Journal of the American College of Cardiology*, 52(19):1574–1580 (2008).

Jellis, C., Martin, J., Narula, J., and Marwick, T. H. "Assessment of nonischemic myocardial fibrosis." *Journal of the American College of Cardiology*, 56(2):89–97 (2010).

Jellis, C. L. and Kwon, D. H. "Myocardial T1 mapping: modalities and clinical applications." *Cardiovascular diagnosis and therapy*, 4(2):126 (2014).

Kammerlander, A. A., Marzluf, B. A., Zotter-Tufaro, C., Aschauer, S., Duca, F., Bachmann, A., Knechtelsdorfer, K., Wiesinger, M., Pfaffenberger, S., Greiser, A., et al. "T1 mapping by CMR imaging: from histological validation to clinical implication." *JACC: Cardiovascular Imaging*, 9(1):14–23 (2016).

Kellman, P. and Hansen, M. S. "T1-mapping in the heart: accuracy and precision." *Journal of cardiovascular magnetic resonance*, 16(1):2 (2014).

Kellman, P., Wilson, J. R., Xue, H., Bandettini, W. P., Shanbhag, S. M., Druey, K. M., Ugander, M., and Arai, A. E. "Extracellular volume fraction mapping in the myocardium, part 2: initial clinical experience." *Journal of Cardiovascular Magnetic Resonance*, 14(1):1–8 (2012).

Kim, R. J., Chen, E.-L., Lima, J. o. A., and Judd, R. M. "Myocardial Gd-DTPA kinetics determine MRI contrast enhancement and reflect the extent and severity of myocardial injury after acute reperfused infarction." *Circulation*, 94(12):3318–3326 (1996).

Klyosov, A. A. *Wood-plastic composites*. John Wiley & Sons (2007).

Knuuti, J., Wijns, W., Saraste, A., Capodanno, D., Barbato, E., Funck-Brentano, C., Prescott, E., Storey, R. F., Deaton, C., Cuisset, T., et al. "2019 ESC Guidelines for the diagnosis and management of chronic coronary syndromes: the Task Force for the diagnosis and management of chronic coronary syndromes of the European Society of Cardiology (ESC)." *European heart journal*, 41(3):407–477 (2020).

Low, D. A. and Dempsey, J. F. "Evaluation of the gamma dose distribution comparison method." *Medical physics*, 30(9):2455–2464 (2003).

Low, D. A., Harms, W. B., Mutic, S., and Purdy, J. A. "A technique for the quantitative evaluation of dose distributions." *Medical physics*, 25(5):656–661 (1998).

Luetkens, J. A., Klein, S., Träber, F., Block, W., Schmeel, F. C., Sprinkart, A. M., Kuetting, D. L., Uschner, F. E., Schierwagen, R., Thomas, D., et al. "Quantification of liver fibrosis: extracellular volume fraction using an MRI bolus-only technique in a rat animal model." *European radiology experimental*, 3(1):1–6 (2019).

Marquardt, D. W. "An algorithm for least-squares estimation of nonlinear parameters." *Journal of the society for Industrial and Applied Mathematics*, 11(2):431–441 (1963).

McDiarmid, A. K., Swoboda, P. P., Erhayiem, B., Ripley, D. P., Kidambi, A., Broadbent, D. A., Higgins, D. M., Greenwood, J. P., and Plein, S. "Single bolus versus split dose gadolinium administration in extra-cellular volume calculation at 3 Tesla." *Journal of Cardiovascular Magnetic Resonance*, 17(1):6 (2015).

McKavanagh, P., Walls, G., McCune, C., Malloy, J., Harbinson, M. T., Ball, P. A., and Donnelly, P. M. "The Essentials of Cardiac Computerized Tomography." *Cardiology and therapy*, 4(2):117–129 (2015).

Messroghli, D. R., Greiser, A., Fröhlich, M., Dietz, R., and Schulz-Menger, J. "Optimization and validation of a fully-integrated pulse sequence for modified look-locker inversion-recovery (MOLLI) T1 mapping of the heart." *Journal of Magnetic Resonance Imaging: An Official Journal of the International Society for Magnetic Resonance in Medicine*, 26(4):1081–1086 (2007).

Messroghli, D. R., Plein, S., Higgins, D. M., Walters, K., Jones, T. R., Ridgway, J. P., and Sivananthan, M. U. "Human myocardium: single-breath-hold MR T1 mapping with high spatial resolution—reproducibility study." *Radiology*, 238(3):1004–1012 (2006).

Messroghli, D. R., Rudolph, A., Abdel-Aty, H., Wassmuth, R., Kühne, T., Dietz, R., and Schulz-Menger, J. "An open-source software tool for the generation of relaxation time maps in magnetic resonance imaging." *BMC medical imaging*, 10(1):16 (2010).

Mewton, N., Liu, C. Y., Croisille, P., Bluemke, D., and Lima, J. A. "Assessment of myocardial fibrosis with cardiovascular magnetic resonance." *Journal of the American College of Cardiology*, 57(8):891–903 (2011).

Miller, C. A., Naish, J. H., Bishop, P., Coutts, G., Clark, D., Zhao, S., Ray, S. G., Yonan, N., Williams, S. G., Flett, A. S., et al. "Comprehensive validation of cardiovascular magnetic resonance techniques for the assessment of myocardial extracellular volume." *Circulation: Cardiovascular Imaging*, 6(3):373–383 (2013).

Monroe, A. K., Haberlen, S. A., Post, W. S., Palella Jr, F. J., Kinsgley, L. A., D WITT, M., Budoff, M., Jacobson, L. P., and Brown, T. T. "Cardiovascular disease risk scores' relationship to subclinical cardiovascular disease among HIV-infected and–uninfected men." *AIDS (London, England)*, 30(13):2075 (2016).

Motoyama, S., Kondo, T., Sarai, M., Sugiura, A., Harigaya, H., Sato, T., Inoue, K., Okumura, M., Ishii, J., Anno, H., et al. "Multislice computed tomographic characteristics of coronary lesions in acute coronary syndromes." *Journal of the American College of Cardiology*, 50(4):319–326 (2007).

Nacif, M. S., Kawel, N., Lee, J. J., Chen, X., Yao, J., Zavodni, A., Sibley, C. T., Lima, J. A., Liu, S., and Bluemke, D. A. "Interstitial myocardial fibrosis assessed as extracellular volume fraction with low-radiation-dose cardiac CT." *Radiology*, 264(3):876–883 (2012).

Nadel, J. and Holloway, C. J. "Screening and risk assessment for coronary artery disease in HIV infection: an unmet need." *Hiv Medicine*, 18(4):292–299 (2017).

Pack, N. A., DiBella, E. V., Wilson, B. D., and McGann, C. J. "Quantitative myocardial distribution volume from dynamic contrast-enhanced MRI." *Magnetic resonance imaging*, 26(4):532–542 (2008).

Patel, P., Borkowf, C. B., Brooks, J. T., Lasry, A., Lansky, A., and Mermin, J. "Estimating per-act HIV transmission risk: a systematic review." *AIDS (London, England)*, 28(10):1509 (2014).

Pirš, M., Jug, B., Eržen, B., Šabović, M., Karner, P., Poljak, M., and Tomažič, J. "Cardiovascular risk assessment in HIV-infected male patients: a comparison of Framingham, SCORE, PROCAM and DAD risk equations." *Acta Dermatovenerol Alp Pannonica Adriat*, 23(3):43–7 (2014).

Prat-Gonzalez, S., Sanz, J., and Garcia, M. J. "Cardiac CT: indications and limitations." *Journal of nuclear medicine technology*, 36(1):18–24 (2008).

Programme, U. N. "Global report: UNAIDS report on the global AIDS epidemic 2019. Geneva: Joint United Nations Programme on HIV." *AIDS* (2019).

Puntmann, V. O., Peker, E., Chandrashekhar, Y., and Nagel, E. "T1 mapping in characterizing myocardial disease: a comprehensive review." *Circulation research*, 119(2):277–299 (2016).

Rienks, M., Papageorgiou, A.-P., Frangogiannis, N. G., and Heymans, S. "Myocardial extracellular matrix: an ever-changing and diverse entity." *Circulation research*, 114(5):872–888 (2014).

Salerno, M., Janardhanan, R., Jiji, R. S., Brooks, J., Adenaw, N., Mehta, B., Yang, Y., Antkowiak, P., Kramer, C. M., and Epstein, F. H. "Comparison of methods for determining the partition coefficient of gadolinium in the myocardium using T1 mapping." *Journal of Magnetic Resonance Imaging*, 38(1):217–224 (2013).

Schelbert, E. B., Fonarow, G. C., Bonow, R. O., Butler, J., and Gheorghiade, M. "Therapeutic targets in heart failure: refocusing on the myocardial interstitium." *Journal of the American College of Cardiology*, 63(21):2188–2198 (2014).

Schelbert, E. B., Testa, S. M., Meier, C. G., Ceyrolles, W. J., Levenson, J. E., Blair, A. J., Kellman, P., Jones, B. L., Ludwig, D. R., Schwartzman, D., et al. "Myocardial extravascular extracellular volume fraction measurement by gadolinium cardiovascular magnetic resonance in humans: slow infusion versus bolus." *Journal of cardiovascular magnetic resonance*, 13(1):1–14 (2011).

Scully, P. R., Bastarrika, G., Moon, J. C., and Treibel, T. A. "Myocardial extracellular volume quantification by cardiovascular magnetic resonance and computed tomography." *Current Cardiology Reports*, 20(3):15 (2018).

Selik, R. M., Mokotoff, E. D., Branson, B., Owen, S. M., Whitmore, S., and Hall, H. I. "Revised surveillance case definition for HIV infection—United States, 2014." *Morbidity and Mortality Weekly Report: Recommendations and Reports*, 63(3):1–10 (2014).

Sgouros, G. "Bone marrow dosimetry for radioimmunotherapy: theoretical considerations." *Journal of Nuclear Medicine*, 34(4):689–694 (1993).

Shah, A. S., Stelzle, D., Lee, K. K., Beck, E. J., Alam, S., Clifford, S., Longenecker, C. T., Strachan, F., Bagchi, S., Whiteley, W., et al. "Global burden of atherosclerotic cardiovascular disease in people living with HIV: systematic review and meta-analysis." *Circulation*, 138(11):1100–1112 (2018).

Southwick, F. "Infectious Diseases: A Clinical Short Course: A Clinical Short Course." (2007).

Stary, H. C., Chandler, A. B., Dinsmore, R. E., Fuster, V., Glagov, S., Insull Jr, W., Rosenfeld, M. E., Schwartz, C. J., Wagner, W. D., and Wissler, R. W. "A definition of advanced types of atherosclerotic lesions and a histological classification of atherosclerosis: a report from the Committee on Vascular Lesions of the Council on Arteriosclerosis, American Heart Association." *Circulation*, 92(5):1355–1374 (1995).

Tarr, P. E., Ledergerber, B., Calmy, A., Doco-Lecompte, T., Marzel, A., Weber, R., Kaufmann, P. A., Nkoulou, R., Buechel, R. R., Kovari, H., et al. "Subclinical coronary artery disease in Swiss HIV-positive and HIV-negative persons." *European heart journal*, 39(23):2147–2154 (2018).

Taylor, A. J., Salerno, M., Dharmakumar, R., and Jerosch-Herold, M. "T1 mapping: basic techniques and clinical applications." *JACC: Cardiovascular Imaging*, 9(1):67–81 (2016).

Treibel, T., White, S., and Moon, J. "Myocardial tissue characterization: histological and pathophysiological correlation." *Current cardiovascular imaging reports*, 7(3):9254 (2014).

Treibel, T. A., Fontana, M., Steeden, J. A., Nasis, A., Yeung, J., White, S. K., Sivarajan, S., Punwani, S., Pugliese, F., Taylor, S. A., et al. "Automatic quantification of the myocardial extracellular volume by cardiac computed tomography: synthetic ECV by CCT." *Journal of cardiovascular computed tomography*, 11(3):221–226 (2017).

Triant, V. A., Perez, J., Regan, S., Massaro, J. M., Meigs, J. B., Grinspoon, S. K., and D'Agostino Sr, R. B. "Cardiovascular risk prediction functions underestimate risk in HIV infection." *Circulation*, 137(21):2203–2214 (2018).

Tseng, Z. H. "Presumed sudden cardiac deaths among persons with HIV and heart failure." (2019).

Ugander, M., Bagi, P. S., Booker, O. J., Hsu, L.-Y., Oki, A. J., Greiser, A., Kellman, P., Aletras, A. H., and Arai, A. E. "Edema by T2-weighted imaging in salvaged myocardium is extracellular, not intracellular." *Journal of Cardiovascular Magnetic Resonance*, 13(S1):P70 (2011).

Ugander, M., Oki, A. J., Hsu, L.-Y., Kellman, P., Greiser, A., Aletras, A. H., Sibley, C. T., Chen, M. Y., Bandettini, W. P., and Arai, A. E. "Extracellular volume imaging by magnetic resonance imaging provides insights into overt and sub-clinical myocardial pathology." *European heart journal*, 33(10):1268–1278 (2012).

Vajapeyam, S., Stamoulis, C., Ricci, K., Kieran, M., and Poussaint, T. Y. "Automated processing of dynamic contrast-enhanced MRI: correlation of advanced pharmacokinetic metrics with tumor grade in pediatric brain tumors." *American Journal of Neuroradiology*, 38(1):170–175 (2017).

Vasile, C. and Pascu, M. *Practical guide to polyethylene*. iSmithers Rapra Publishing (2005).

Wang, H.-q., Jin, K.-p., Zeng, M.-s., Chen, C.-z., Rao, S.-x., Ji, Y., Fu, C.-x., and Sheng, R.-f. "Assessing liver fibrosis in chronic hepatitis B using MR extracellular volume measurements: comparison with serum fibrosis indices." *Magnetic Resonance Imaging*, 59:39–45 (2019).

Wessels, B. W., Bolch, W. E., Bouchet, L. G., Breitz, H. B., DeNardo, G. L., Meredith, R. F., Stabin, M. G., and Sgouros, G. "Bone marrow dosimetry using blood-based models for radiolabeled antibody therapy: a multiinstitutional comparison." *Journal of nuclear medicine*, 45(10):1725–1733 (2004).

Weustink, A. C. and de Feyter, P. J. "Radiation exposure in cardiac multislice spiral computed tomography (MSCT)." *F1000 Medicine Reports*, 1 (2009).

Wiesmann, F., Petersen, S. E., Leeson, P. M., Francis, J. M., Robson, M. D., Wang, Q., Choudhury, R., Channon, K. M., and Neubauer, S. "Global impairment of brachial, carotid, and aortic vascular function in young smokers: direct quantification by high-resolution magnetic resonance imaging." *Journal of the American College of Cardiology*, 44(10):2056–2064 (2004).

Wong, T. C., Piehler, K. M., Kang, I. A., Kadakkal, A., Kellman, P., Schwartzman, D. S., Mulukutla, S. R., Simon, M. A., Shroff, S. G., Kuller, L. H., et al. "Myocardial extracellular volume fraction quantified by cardiovascular magnetic resonance is increased in diabetes and associated with mortality and incident heart failure admission." *European heart journal*, 35(10):657–664 (2014).

Wypych, G. *Handbook of polymers*. Elsevier (2016).

Xue, H., Shah, S., Greiser, A., Guetter, C., Littmann, A., Jolly, M.-P., Arai, A. E., Zuehlsdorff, S., Guehring, J., and Kellman, P. "Motion correction for myocardial T1 mapping using image registration with synthetic image estimation." *Magnetic resonance in medicine*, 67(6):1644–1655 (2012).

Yeung, J., Sivarajan, S., Treibel, T., Rosmini, S., Fontana, M., Gillmore, J., Hawkins, P., Punwani, S., Moon, J., Taylor, S., et al. "Measurement of liver and spleen interstitial volume in patients with systemic amyloid light-chain amyloidosis using equilibrium contrast CT." *Abdominal Radiology*, 42(11):2646–2651 (2017).

Zamecnik, J. "The extracellular space and matrix of gliomas." *Acta neuropathologica*, 110(5):435–442 (2005).

Zhou, X., Shi, Q.-H., Bai, S., and Sun, Y. "Dense pellicular agarose–glass beads for expanded bed application:: Fabrication and characterization for effective protein adsorption." *Biochemical engineering journal*, 18(2):81–88 (2004).